TWO-DIMENSIONAL PHOTONIC BAND GAP CRYSTALS

Thesis by
Cheryl Marie Anderson

In Partial Fulfillment of the Requirements
for the Degree of
Doctor of Philosophy

California Institute of Technology
Pasadena, California

1999

(Submitted December 8, 1998)

To Mom and Dad

Acknowledgments

I have been fortunate to have had the support of many extraordinary people during my six years at Caltech, and I want to thank all of those who have helped to make my graduate studies a rewarding experience.

My advisor, Konstantinos Giapis, deserves a lot of recognition for his patience and teaching, and for providing the opportunity to learn about a field far outside the bounds of traditional chemical engineering. I'm not sure what he hoped for in a "first student" but I'll bet that I was more than he bargained for. We both started out pretty green—new grad student, new advisor—and it hasn't always been an easy road. Looking back, I can appreciate the necessity of the tough times so that I might become stronger both professionally and personally. I hope that I've been able to teach him something as well. Thank you, Kostas.

Thank you to all the members of the Giapis group: Gyeong Hwang, Mike Gordon, Jason Kenney, and Rhett Brewer, for being such great lab buddies. May the luck of the lab squid be with you always.

Many people behind-the-scenes have routinely gone above and beyond the call of duty to help keep disasters to a minimum. Suresh Gupta, computer guru, somehow always managed to fix my latest computer mishap. Kathy Bubash is an unequaled source of campus information, and genuinely cares about students. Guy Duremburg, Ray Garcia, and Mike Roy in the Chemistry Machine Shop are extremely talented machinists and could always be counted on to brighten my day.

I have been truly blessed with many wonderful friends here at Caltech. I owe special thanks to Nikki Takarabe for being the most amazing friend I could have hoped to find. She is the perfect swimming and running partner, a fellow chocolate addict, and a gifted matchmaker; my graduate experience would have been greatly diminished without

her friendship. My classmate Mike Vicic has been a great friend and "honorary chick" throughout our Caltech years together, and deserves recognition for his attempts to teach me how not to throw like a girl. I am very grateful to all the members of the Davis group for adopting me as one of their own when I was group-less, especially: Shervin Khodabandeh for numerous late-night discussions about what we want to do with our lives; Larry and Dara Beck for cooking real dinners for me and for taking care of my mice; and Paul Wagner for counterbalancing my zaniness with his calm demeanor and coffee breaks during thesis writing. I would also like to thank Clint Dodd and the whole Caltech waterpolo gang for teaching me some dirty underwater tricks and for providing a very effective form of stress relief.

I owe a very special thanks to my entire family, "old" and "new." Bruce and Sue Dartt have warmly accepted me into their hearts, and have been a wonderful source of comfort and support during the last few years of my graduate work. I am honored to be a member of the Dartt family. My brother, Chris, has always stuck by me and has made me feel very special by the pride he shows for his "Sis." Finally, thank you so much to my Mom and Dad for always being there for me with their unlimited supply of encouragement and support. As only parents can do, they could say, "Just get it done," and "Don't work too hard," in the same conversation, but their boundless love for me was always very clear.

By far the best thing my Ph.D. experience gave me is my husband, Chris Dartt. He started out as "the cute blonde guy in the lab down the hall" and has become my best friend. CBD, you have been with me through everything and I know it hasn't been easy on you. You have put up with more than anyone could reasonably expect, and have done it with more love, patience, and understanding than I thought possible. Without you I never would have made it through. (I love you!!)$^\infty$ and I look forward to spending the rest of my life showing you how much it's true.

Abstract

A photonic crystal is a periodic dielectric structure that possesses a band of frequencies in which propagating electromagnetic waves are forbidden. Two-dimensional photonic crystals exhibit a band gap for waves traveling in the crystal plane, a property that offers promise for improved operation of optoelectronic devices including semiconductor lasers, light-emitting diodes, and frequency filters.

A theoretical investigation of two-dimensional photonic band gap crystals has been performed. The plane-wave expansion method is used to solve Maxwell's equations for the electromagnetic frequency bands in several square (Laue group *4mm*) and triangular (Laue group *6mm*) crystal structures. The size of absolute band gaps is often limited by band degeneracies at lattice symmetry points. By reducing the lattice symmetry, these degeneracies can be lifted to increase the size of existing photonic band gaps, or to create new gaps where none existed for the more symmetric structure. Symmetry analysis also offers a rational approach for exploring and designing new photonic crystal structures. Gap maps for several important crystal structures are presented as a useful reference guide for experimentalists.

The utility of photonic crystals for many applications is enhanced through the introduction of a defect into the crystal structure, which creates localized frequency states within the photonic band gap. Defect modes in two-dimensional square photonic crystal structures were studied using a supercell approach. By changing the radius of a single rod, several defect modes with complex electromagnetic field patterns appear within the photonic band gap. The mode frequencies can be tuned by varying the size of the defect rod. The double-rod square structure has two rod types per unit cell, yielding different defect characteristics depending on which rod is altered.

In addition, anisotropic etching of patterned silicon has been investigated experimentally using a hyperthermal neutral fluorine atom beam generated by laser-induced detonation of SF_6. The detrimental effects of surface charging are eliminated by the use of charge-neutral etch species; however, inelastic scattering of energetic reactive species has a significant effect on the development of the etch profiles, especially at high aspect ratios. Etch profile anomalies including microtrenching and undercutting are observed.

Table of Contents

CHAPTER 1

Introduction

Light scattering is at the heart of many of nature's most spectacular displays, including the formation of rainbows, clear blue skies, and fiery sunsets. Even the brilliant colors of blue jay feathers and butterfly wings are the result of the interplay of light waves with thin films and fine microstructures on the wing surface. The rather simple interactions of electromagnetic waves with scattering elements help to create a world filled with beautiful colors.

The *Lycaena alciphron* butterfly shown in Fig. 1-1(a) is brightly colored with shades of blue, purple, and copper. Such colors are not caused by pigments, which are rarely found in animals, but instead are "structural" colors: the wing surfaces are covered with arrays of precise and repeated structures that scatter light to produce the color.[1,2] The scanning electron micrograph in Fig. 1-1(b) shows an example of these microfeatures, which have a periodicity on the order of visible light wavelengths. Similar multilayer thin-film structures are also responsible for the iridescent color of some butterflies and birds.

The marvelous effects of light scattering processes are not limited to nature. Many of the technological advances made in the field of optics have come about by the ability to utilize light scattering, reflection, and refraction in a useful manner. Light waves are confined within the high refractive index glass of fiber optic cables by total internal reflection. The structure of atoms in a crystalline solid are explored by scattering x-rays off of the crystal and studying the resulting diffraction pattern. The dielectric mirrors commonly used in laser cavities rely on coherent scattering of light waves off of

the layered interfaces of dissimilar materials. These are just a few examples of the ways in which light properties can be controlled and used in applications.

The near-perfect reflective property of dielectric mirrors is the result of stacking several layers of low-loss dielectric with alternately high and low refractive index, each of which is a quarter-wavelength thick. In this way, electromagnetic waves with the desired wavelength will satisfy the Bragg condition for coherent reflection,

$$2d\cos\theta = n\lambda, \tag{1.1}$$

where d is the thickness of the repeating unit, θ is the angle of incidence, $n = 1, 2, 3...$, and λ is the light wavelength. Since the Bragg condition for a quarter-wave stack is satisfied at $\theta = 0°$, these mirrors reflect light efficiently at normal (or near-normal) incidence yielding a "stop band" of frequencies about the wavelength λ. Waves with frequencies outside the stop band, or that are incident upon the mirror at an angle, are transmitted through the layered mirror.

The reflection and transmission properties of the dielectric mirror are a result of classical scattering of light from the interfaces of two different media, and are not restricted to this one-dimensional structure. In fact, we can extend the same concept of periodic dielectric materials to higher dimensions to create a photonic crystal—a structure that has the ability to reflect light frequencies through a range of incident angles, and for all polarizations of light. Examples of periodic crystal structures in one, two, and three dimensions are shown in Fig. 1-2. Like the quarter-wave stack, a photonic crystal has a frequency stop band called the photonic band gap (PBG), a region of the electromagnetic frequency spectrum where propagating modes are forbidden. In two dimensions, the PBG exists for waves traveling in the plane of the crystal; in three dimensions, light waves at all angles of incidence with frequencies within the PBG are reflected. In each case, it is the proper selection of materials and geometry that gives photonic crystals the ability to control the propagation of light waves.

1.1 Photonic Crystals

The new field of photonic crystal research began in 1987, when Yablonovitch first suggested that a three-dimensionally periodic dielectric structure could be made to possess a forbidden frequency gap irrespective of the propagation direction.[3] His idea was to use the photonic crystal to inhibit the spontaneous emission of atoms by overlapping the frequency band gap with the atomic emission frequency. Reducing the power losses to spontaneous emission would result in improved performance of optoelectronic devices that are limited by spontaneous processes, such as semiconductor lasers, heterojunction bipolar transistors, and solar cells. Also in the same year, John suggested that a three-dimensional dielectric superlattice array could induce strong localization of photons, an effect that may lead to a number of useful device applications.[4]

The tantalizing prospects for the improved operation of optoelectronic devices spurred researchers to prove (or disprove) that photonic crystals could exist. Within a few years, researchers had established the theoretical basis for calculating the properties of photonic crystals[5-7] and had identified specific geometries in two[8-10] and three[7,11] dimensions that should possess a photonic band gap. In 1991, the first experimental verification of theoretical predictions was achieved when a face-centered-cubic-like structure of air holes in dielectric was found to possess a full photonic band gap in the microwave regime.[12]

Photonic crystals are not limited to any fundamental length scale; in fact, the wavelength of the photonic band gap directly scales with the size of the dielectric elements that form the crystal. Specifically, the periodicity of the scattering elements should be of the order $\lambda/2$. Many of the proposed device applications of photonic crystals involve light in the visible and near-IR region of the electromagnetic spectrum (λ in the range of 300 to 1500 nm) requiring photonic crystal features on the order of tenths of

microns. This is the same size scale of the features on computer chips, microfabricated with state-of-the-art processing technology. However, photonic crystals have an additional requirement over computer chips in that the tiny features must possess near-perfect periodicity over several microns in width—a challenging feat even with current advanced techniques. Three-dimensional photonic crystals pose an even greater challenge as the perfect periodicity must be extended in the vertical direction. Though some clever three-dimensional photonic crystal designs have been proposed[13-16] to help ease the trouble of microfabrication, such structures may still lie beyond the reach of our current abilities.

Two-dimensional photonic crystals, however, are easier to microfabricate than their 3D counterparts precisely because the requirement of periodicity in the third dimension has been removed. Thus, the 2D structure readily lends itself to standard photolithographic and etching techniques. The desired crystal pattern is defined in photoresist on the surface of a dielectric material, and can then be transferred to the material below with an anisotropic etching process.

Although 3D photonic crystals may hold the greatest promise for applications due to their unique ability to control light waves irrespective of the direction of propagation, the importance of 2D structures should not be underestimated. Their strong reflectivity properties over a wide frequency band and all angles within the crystal plane provide an advantage over traditional (one-dimensional) Bragg mirrors. Applications where such dielectric mirrors are used (e.g., laser diodes[17]) could be improved through the use of 2D periodic structures. The relative ease of fabrication and their role in important device applications makes 2D photonic crystals worthy of more detailed study, and provides the motivation for the research work presented here.

1.2 Theoretical Considerations

Ideally, one would like to be able to specify the desired properties of the photonic crystal (e.g., a large band gap) and then perform calculations to determine the crystal structure that will possess these properties. Unfortunately, the solution is not straightforward—while it is known how to calculate the frequency band properties from a given photonic crystal structure, the inverse problem remains as yet intractable. One must propose a specific photonic crystal structure, perform the frequency calculations, and then evaluate the results. Thus, our success at achieving the desired properties relies on our ability (or luck) to guess *a priori* a correct crystal structure. A guiding principle that would help researchers sift through the countless geometrical arrangements and select the most promising crystal structures would be invaluable.

The initial studies of two-dimensional photonic crystals focused on simple rod geometries (square and circular cross-sections) arranged in patterns described by the basic 2D Bravais lattices. Band gap calculations of these crystals showed that some arrangements, like that of the triangular lattice of nearly close-packed "air rods" (holes) in a dielectric background, do possess large band gaps. Similarly, holes arranged on a square lattice also possessed a photonic band gap, albeit smaller than that for the triangular-based structure. It was also found that crystals composed of circular cross-section rods tended to have larger band gaps than those crystals with hexagonal or square cross-section rods.[10]

At first glance these results appear to suggest that a high degree of crystal symmetry is required for a photonic band gap to appear. On the other hand, symmetry tends to foster degeneracies in the frequency bands which inhibit the opening of band gaps. For example, a uniform material is perfectly symmetric but does not possess any band gaps because the lack of dielectric constant modulation leads to a continuous spectrum of allowed frequencies. Thus, a balance of symmetry and disorder is necessary

for the crystal to have a photonic band gap. By gaining a greater understanding of this delicate balance, the observed characteristics of the photonic crystals could be explained in terms of their symmetry properties. In addition, crystal symmetry can be used as a guiding principle in the design of large band gap photonic crystals.

1.3 Fabrication of Photonic Crystals

Once the theoretical studies have identified a photonic crystal geometry with the desired properties, the next step is to fabricate the crystal structure. For photonic band gaps in the microwave regime, the fundamental length scale of the crystal is on the order of centimeters allowing for straightforward construction with bulk dielectric materials and a patient machinist. Smaller photonic crystals are more difficult to microfabricate, though techniques for creating near-perfect photonic crystals with sizes on the order of microns have been successfully developed. In one interesting example, a 2D photonic crystal with a band gap centered at a wavelength of 5 μm was fabricated by electrochemical etching of silicon in hydrofluoric acid.[18] This structure, shown in Fig. 1-3, was etched to a depth of 75 μm, with a lattice constant of only 2.3 μm. Though this example was an important breakthrough for photonic crystal fabrication, the technique would be difficult to apply in cases where the photonic crystal is used in an optoelectronic device such as a light-emitting diode. In such instances it would be most convenient to directly integrate the photonic crystal and device, using the same processing steps for both components simultaneously. This can be achieved by using micro-fabrication techniques.

The ideal two-dimensional crystal has perfect periodicity within the plane, and a long extension of the structure in the third dimension (i.e., a high aspect ratio) so as to eliminate the end effects of the rods. Even if the crystal is "sandwiched" between cladding layers, the etched holes (rods) must penetrate well into the bottom cladding layer

to minimize power losses in the vertical direction.[19] The requirement of high aspect ratios with minimal variation in the rod diameter along their entire length poses great demands on the fabrication process. The crystal specifications become even more difficult to realize when the photonic band gap is chosen to occur in the visible to near-IR frequency regime.

Many of the profile anomalies that occur during plasma etching of small features are caused by electrical charge build-up on the photoresist layer used to define the etch pattern. The excess charge creates a static electric field that can deflect the path of incoming reactive ions, resulting in profile irregularities such as bowed sidewalls and microtrenches at the foot of etched features. Such phenomena can considerably alter the desired feature profiles and hinder attempts to achieve high aspect ratios.

The problem of charge-induced nonuniformities can be eliminated by using neutral species instead of ions. However, this entails the difficulty of creating a directional source of reactive neutrals necessary to achieve anisotropic etching. Ions are easily accelerated and directed by electromagnetic fields, but neutral species require a different approach. A novel method and apparatus for generating a nearly mono-energetic beam of neutral atoms with energies of 1–10 eV was developed for the study of gas-surface scattering experiments.[20] This source can be adapted to create a collimated beam of reactive neutral atoms with hyperthermal translational energies suitable for anisotropic etching.

1.4 Research Objectives

Before a photonic crystal is utilized to improve performance of an optoelectronic device, the properties of the crystal itself should be optimized. Since it is the photonic band gap that makes such crystals desirable for applications, it is essential to identify and design crystal structures which possess the largest possible photonic band gaps.

Theoretical calculations are an important first step in this design process. In this thesis work we sought to identify two-dimensional photonic crystal structures that possess large photonic band gaps, using analysis of the crystal symmetry properties as a guide towards the most promising geometries.

The work presented in Chapter 2 focuses on the class of 2D crystal structures formed with a square lattice basis (designated Laue symmetry group *4mm*). The size of the photonic band gaps in these structures is often limited by degenerate frequencies at points of high lattice symmetry. These band degeneracies can be lifted by altering the lattice symmetry properties, potentially increasing the size of existing photonic band gaps, or causing new gaps to open where none existed before. Specifically, we explore the effects of symmetry changes brought about by the addition of different diameter rods into the unit cell of these crystals.

In Chapter 3, an overview of the hexagonal 2D photonic crystal structures that form Laue symmetry group *6mm* is presented. This symmetry group contains two of the most widely utilized crystal structures in experiments, the triangular and honeycomb structures. We compare the band gap properties of several structures that fall within the *6mm* class based on their symmetry properties. Small changes to the crystal symmetry properties can have a great impact on the photonic band gap properties of the crystal. The symmetry-based approach is used to identify 2D structures that possess large band gaps and also have geometries that lend themselves to easy microfabrication. The compiled results can serve as a useful reference guide for experimentalists.

Perfect photonic crystals are useful because of their ability to reflect electromagnetic waves at all frequencies inside the photonic band gap. However, some very useful properties can be obtained through the introduction of a physical defect into the otherwise perfect crystal structure. A photonic crystal defect is analogous to the intentional addition of dopant atoms into a semiconductor material; in both cases, the defect introduces discrete allowed states into the band gap. Because the allowed photonic

defect modes are bordered by forbidden frequencies, they can be used as a well-defined "sink" for electromagnetic energy. This property can be exploited in light-emitting devices such as semiconductor lasers and diodes, where it is desirable to channel as much of the input energy as possible into a single mode. The introduction of physical defects into square photonic crystal structures is described in Chapter 4. Some implications of defect modes for improved device operation are also explored.

Finally, in Chapter 5 experimental studies of neutral fluorine etching of silicon are presented. A pulsed beam of hyperthermal neutral fluorine atoms with translational energies tunable from 4 to 30 eV is used for the anisotropic etching of patterned silicon. Though the use of neutral species prevents the appearance of etch profile anomalies by charge-induced processes, scattering of energetic reactive species was found to affect significantly the development of feature profiles.

1.5 References

[1] H. Ghiradella, "Light and Color on the Wing: Structural Colors in Butterflies and Moths," *Appl. Optics* **30**, 3492 (1991).

[2] H. Tada, S. E. Mann, I. N. Miaoulis, and P. Y. Wong, "Effects of a Butterfly Scale Microstructure on the Iridescent Color Observed at Different Angles," *Appl. Optics* **37**, 1579 (1998).

[3] E. Yablonovitch, "Inhibited Spontaneous Emission in Solid-State Physics and Electronics," *Phys. Rev. Lett.* **58**, 2059 (1987).

[4] S. John, "Strong Localization of Photons in Certain Disordered Dielectric Superlattices," *Phys. Rev. Lett.* **58**, 2486 (1987).

[5] K. M. Leung and Y. F. Liu, "Full Vector Wave Calculation of Photonic Band Structures in Face-Centered-Cubic Dielectric Media," *Phys. Rev. Lett.* **65**, 2646 (1990).

[6] Z. Zhang and S. Satpathy, "Electromagnetic Wave Propagation in Periodic Structures: Bloch Wave Solution of Maxwell's Equations," *Phys. Rev. Lett.* **65**, 2650 (1990).

[7] K. M. Ho, C. T. Chan, and C. M. Soukoulis, "Existence of a Photonic Gap in Periodic Dielectric Structures," *Phys. Rev. Lett.* **65**, 3152 (1990).

[8] R. D. Meade, K. D. Brommer, A. M. Rappe, and J. D. Joannopoulos, "Existence of a Photonic Band Gap in Two Dimensions," *Appl. Phys. Lett.* **61**, 495 (1992).

[9] P. R. Villeneuve and M. Piché, "Photonic Band Gaps in Two-Dimensional Square and Hexagonal Lattices," *Phys. Rev. B* **46**, 4969 (1992).

[10] P. R. Villeneuve and M. Piché, "Photonic Band Gaps in Two-Dimensional Square Lattices: Square and Circular Rods," *Phys. Rev. B* **46**, 4973 (1992).

[11] C. T. Chan, K. M. Ho, and C. M. Soukoulis, "Photonic Band Gaps in Experimentally Realizable Periodic Dielectric Structures," *Europhys. Lett.* **16**, 563 (1991).

[12] E. Yablonovitch, T. J. Gmitter, and K. M. Leung, "Photonic Band Structure: The Face-Centered-Cubic Case Employing Nonspherical Atoms," *Phys. Rev. Lett.* **67**, 2295 (1991).

[13] S. Fan, P. R. Villeneuve, R. D. Meade, and J. D. Joannopoulos. Design of Three-Dimensional Photonic Crystals at Submicron Lengthscales. *Appl. Phys. Lett.* **65**, 1466 (1994).

[14] K. M. Ho, C. T. Chan, C. M. Soukoulis, R. Biswas, and M. Sigalas. Photonic Band Gaps in Three Dimensions: New Layer-By-Layer Periodic Structures. *Solid State Comm.* **89**, 413 (1994).

[15] E. Özbay, E. Michel, G. Tuttle, R. Biswas, K. M. Ho, J. Bostak, and D. M. Bloom. Double-Etch Geometry for Millimeter-Wave Photonic Band-Gap Crystals. *Appl. Phys. Lett.* **65**, 1617 (1994).

[16] H. S. Sözüer and J. P. Dowling. Photonic Band Calculations for Woodpile Structures. *J. Mod. Opt.* **41**, 231 (1994).

[17] D. L. Bullock, C.-C. Shih, and R. S. Margulies, "Photonic Band Structure Investigation of Two-Dimensional Bragg Reflector Mirrors for Semiconductor Laser Mode Control," *J. Opt. Soc. Am. B* **10**, 399 (1993).

[18] U. Grüning, V. Lehmann, S. Ottow, and K. Busch, "Macroporous Silicon with a Complete Two-Dimensional Photonic Band Gap Centered at 5 μm," *Appl. Phys. Lett.* **68**, 747 (1996).

[19] B. D'Urso, O. Painter, J. O'Brien, T. Tombrello, A. Yariv, and A. Scherer, "Modal Reflectivity in Finite-Depth Two-Dimensional Photonic-Crystal Microcavities," *J. Opt. Soc. Am. B* **15**, 1155 (1998).

[20] G. E. Caledonia, R. H. Krech, and D. B. Green, "Source of High Flux Energetic Atoms," U.S. Patent No. 4894511 (January 16, 1990).

[21] P. L. Gourley, J. R. Wendt, G. A. Vawter, T. M. Brennan, and B. E. Hammons, "Optical Properties of Two-Dimensional Photonic Lattices Fabricated as Honeycomb Nanostructures in Compound Semiconductors," *Appl. Phys. Lett.* **64**, 687 (1994).

[22] M. Maier, World Wide Web URL: http://EuropeanButterflies.com.
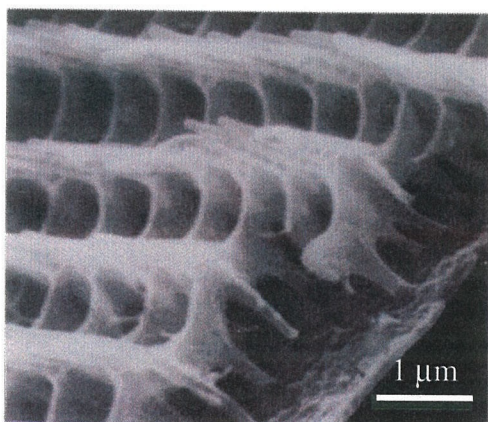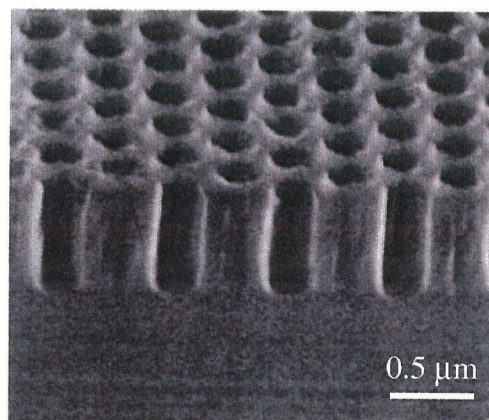
Fig. 1-1. The blue, purple, and copper colors of the butterfly *Lycaena alciphron* (a) have their origin in light scattering from fine microstructures on the wing surface, an example of which is shown in (b) for the *Zeuxidia amethystis* butterfly.[1] The wing microfeatures closely resemble a two-dimensional photonic crystal (c).[21] The photograph in (a) is reprinted with permission from M. Maier.[22]
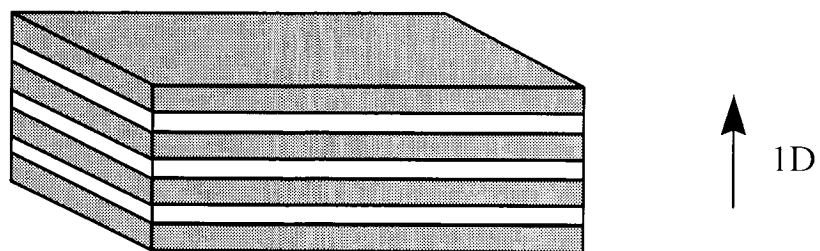
(a)
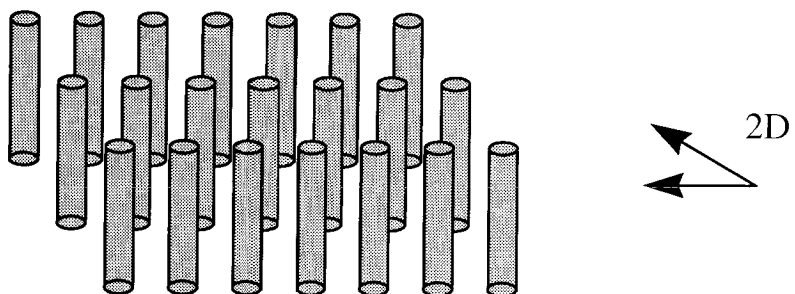
(b)
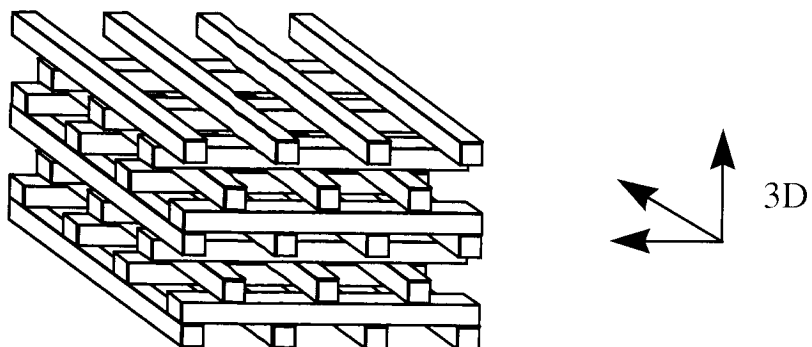
(c)

Fig. 1-2. Schematic drawings showing examples of (a) one-, (b) two-, and (c) three-dimensional photonic crystal structures. The "one-dimensional photonic crystal" shown in (a) is a traditional quarter-wave stack dielectric mirror.
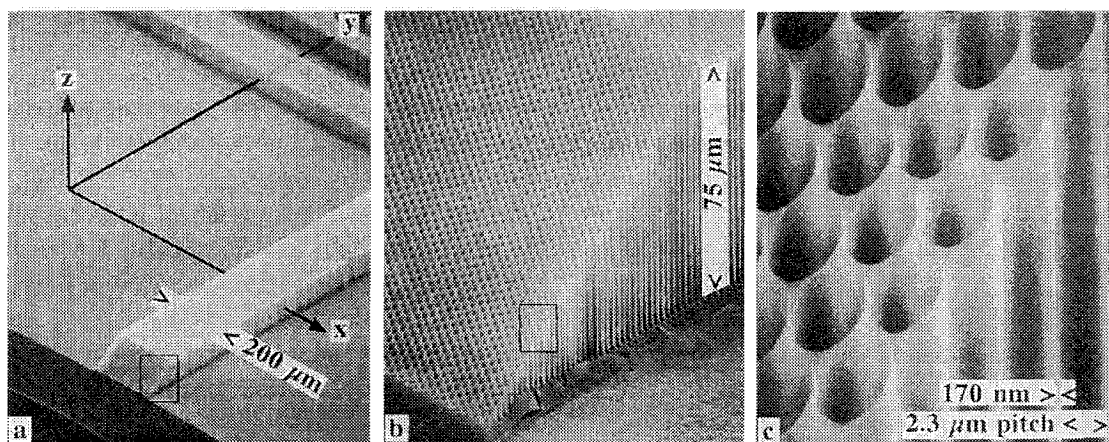
Fig. 1-3. Scanning electron micrographs of a two-dimensional photonic crystal fabricated by electrochemical etching of silicon.[18] (a) The photonic crystal structure is 200 μm wide and 75 μm high. The lattice constant of the triangular macropore array is 2.3 μm, and the diameter of the pores is 2.13 μm. (b) A tenfold magnification of the inset in (a) shows the micromachined edges of the photonic crystal and the polished 45° inclined edge. (c) A tenfold magnification of the inset in (b) shows the perfect periodicity of the crystal structure. The pore walls are just 170 nm thick.

CHAPTER 2

Symmetry Reduction in Group *4mm* Photonic Crystals

<u>Abstract</u>

The size of absolute band gaps in two-dimensional photonic crystals is often limited by band degeneracies at the lattice symmetry points. By reducing the lattice symmetry, these degeneracies can be lifted to increase the size of existing photonic band gaps, or to create new gaps where none existed for the more symmetric structure. Specifically, symmetry reduction by the addition of different diameter rods into the unit cell of two-dimensional square lattices (Laue group *4mm*) is explored. This approach is especially useful in opening absolute band gaps in structures of dielectric rods in air, which are more easily microfabricated than a crystal of air columns in a dielectric background. Symmetry reduction offers a rational approach for exploring and designing new photonic crystal structures.

2.1 Introduction

The past decade has witnessed the start of an exciting new field in optoelectronics. The first assertion in 1987 that periodic dielectric structures could be made to possess a photonic band gap[1,2]—a region of the frequency spectrum where propagating modes are forbidden—has captured the imaginations of researchers around the world. A photonic band gap is analogous to an electronic band gap in semiconductors; this analogy bears promise for photonic crystals to impact optical device applications as semiconductors have done for electronics.

Much of the interest surrounding photonic crystals stems from their ability to provide frequency-mode control of light propagating through them. This property gives photonic crystals the potential to greatly improve the efficiency of optoelectronic devices. For example, radiation losses in high-Q resonance cavities can be reduced by embedding the cavity in a photonic crystal.[3] Frequencies that fall within the photonic band gap are exponentially attenuated with no absorption. The use of an entirely dielectric medium also provides an improvement over traditional metallic shielding methods, where high losses reduce their usefulness at optical frequencies. Fine control of frequency propagation may be obtained through the introduction of "defect" modes (localized frequency modes) into the gap, which channel emission to one or a few select frequencies.[3-5] Photonic defect modes, most easily formed by blocks of dielectric material inserted into or removed from the photonic crystal, could lead to thresholdless solid-state lasers and more efficient solar cells.

Many three-dimensional[6-8] and two-dimensional[5,9-11] photonic crystals with band gaps in the microwave region have been fabricated. For the most promising applications, however, it is desirable to have photonic gaps at visible to near-infrared (IR) wavelengths. The frequency at which the band gap occurs is directly related to the size of the scattering elements comprising the lattice. Specifically, the size of the features must be of order

$\lambda/2$, where λ is the wavelength at which the gap occurs. A photonic crystal with a band gap in the microwave regime has lattice elements a few millimeters in size, but to achieve a band gap in the visible region of the electromagnetic spectrum requires precise fabrication of lattice elements on the order of 0.25 μm. Though a method for microfabricating three-dimensional (3D) crystals with full photonic band gaps using standard photolithographic and etching techniques has been proposed,[7] fabrication of such small features is exceedingly difficult. Perhaps for this reason attention has been drawn towards two-dimensional (2D) lattice structures, where fabrication requirements are not as stringent. Several groups have successfully fabricated 2D crystals with near-IR band gaps[12-14] and even visible frequency gaps.[15]

Although 3D photonic crystals suggest the most interesting ideas for novel applications, 2D structures could also find several important uses, as a result of their strong *angular* reflectivity properties over a wide frequency band. For example, 2D photonic crystals with absolute band gaps provide a large stop band for use as a feedback mirror in laser diodes,[16] an improvement over traditional (one-dimensional) Bragg reflectors.

The larger a photonic band gap is, the greater the forbidden region of the frequency spectrum. Thus, it is essential to identify and design crystal structures which possess the largest photonic band gaps for a given dielectric contrast ratio. For two different crystals possessing absolute band gaps of equal size, it may be advantageous from a fabrication standpoint to choose the one that has the band gap occurring at the higher non-dimensionalized frequency, $\omega a/2\pi c$, where ω is the frequency, a is the lattice constant, and c is the speed of light in vacuum. For a given filling fraction, the feature size scales with a; thus, the crystal with the higher $\omega a/2\pi c$ should be easier to fabricate. But how does one sift through the countless geometrical arrangements to select manufacturable structures with large band gaps in the desired frequency regime? Theoretical calculations are indispensable, albeit a formidable task in view of the

numerous structures to model with many variational parameters (e.g., lattice type, filling fraction, shape of filling element). A rational approach towards the design of photonic crystals is needed, rather than brute-force computation.

Photonic crystals are most valuable when they possess an *absolute* band gap, where propagating modes are forbidden regardless of wave polarization. Many crystals possess band gaps for some light polarizations, but these may not overlap to produce an absolute band gap. Often this is a result of band degeneracies at points of high symmetry in the crystal, which prevent gaps from opening. In some cases the degeneracy can be lifted by reducing the crystal symmetry. Consider for example the 3D face-centered-cubic lattice with spherical dielectric "atoms," which does not possess an absolute photonic band gap.[17] By decreasing the symmetry of the lattice through the introduction of a two-point basis set (which produces the diamond lattice), a degeneracy in the bands is lifted and a full photonic band gap is obtained.[17] In two-dimensional photonic crystals, a similar idea of lattice symmetry reduction has also been effective in producing larger band gaps.[18] Here, we present a more complete description of symmetry reduction in Laue group *4mm* lattices.

2.2 Two-Dimensional Square Structures

There are three plane groups (two-dimensional space groups) that comprise the square crystal family: *p4*, *p4mm*, and *p4gm*.[19] The first belongs to the Laue group *4*, a relatively low symmetry group that has four symmetry operations. Each of the last two plane groups possesses eight symmetry operations and together they form the Laue group *4mm*. Two-dimensional photonic crystals that have the symmetry of the latter group will be the focus of the present article. Such crystals are formed by circular cross-section rods having a dielectric constant ε_a, embedded in a different background material with dielectric constant ε_b. The infinitely long rods are assumed to be parallel to the z axis,

and the cross-section with the x-y plane forms one of the group *4mm* lattices. There are several ways to arrange rods within the unit cell of such a lattice without departing from the symmetry group. The simplest structure (shown by the rods labeled with index A in Fig. 2-1) contains one rod in each primitive unit cell, with the rod axes arranged on the lattice sites given by the vectors

$$\mathbf{a}(\ell) = \ell_1 \mathbf{a}_1 + \ell_2 \mathbf{a}_2 \qquad (2.1)$$

Here $\mathbf{a}_1$ and $\mathbf{a}_2$ are primitive lattice vectors and ℓ_1 and ℓ_2 are any two integers, collectively termed ℓ. For the coordinate system shown, the primitive lattice vectors are $\mathbf{a}_1 = a(1,0)$ and $\mathbf{a}_2 = a(0,1)$, where a is the lattice constant. The rods occupying these sites all have diameter d_1.

A different structure can be obtained by the overlay of another square lattice with rods of diameter d_2 on top of the single-rod square lattice, as shown by the index B rods in Fig. 2-1. The added structure has the same lattice constant a, but is displaced with respect to the first lattice by $\tau = \frac{1}{2}(\mathbf{a}_1 + \mathbf{a}_2)$. This arrangement forms a new lattice when $d_1 \neq d_2$, which is termed the "double-rod square lattice." Both the single-rod and double-rod square lattice structures have the symmetry of the plane group *p4mm*, and all of the rod sites have *4mm* symmetry (i.e., four-fold rotation and mirror planes along the two principal symmetry axes).[19] However, the symmetry is changed slightly in the latter crystal structure, as the smallest unit cell must now contain two rods. In either case, the rods are all assumed to be made of the same dielectric material and are embedded in a different dielectric background. The ratio of the two rod diameters, $\beta = d_2/d_1$, can be varied to control the position and size of band gaps. The rod diameter ratio can have values from 0 to ∞, but since β and β^{-1} yield equivalent crystal structures, we examine β values between 0 and 1 only. Note that at either $\beta = 0$ or 1, the single-rod square lattice structure is recovered.

There are several other ways in which one can reduce the symmetry of the single-rod square structure. Consider the "glide-symmetry square lattice" as shown in Fig. 2-2. While at first glance this structure might not appear to be more than a random collection of rods, it belongs in the plane group *p4gm*, thus possessing quite a large number of symmetry operations. Each rod site has ..*m* symmetry (a mirror plane off the principal axes). The primitive unit cell is shown by the square outline. Varying the angle that the lattice elements form with the primitive unit cell produces a whole class of new structures. We define this angle of tilt, θ, as the angle between the line diagonal of the lattice elements and the *x* axis, as illustrated in Fig. 2-2.

New structures can emerge from combining the two previous ideas, i.e., increasing the number of rods in the unit cell and introducing the glide symmetry operation. Consider, for example, the overlay of this new glide-symmetry lattice structure with the single-rod square lattice, such that the rods of the latter lie at the corners and center of the primitive unit cell. The single-rod square lattice elements have diameter d_1, and the rods associated with the glide lattice have diameter d_2. This complex structure combines two different rod symmetries, with a total of six rods in each primitive unit cell. We will show that even this type of symmetry reduction can yield large absolute band gaps. The glide lattice, superimposed with the single-rod square lattice, gives two parameters that may be varied to maximize the absolute photonic band gap: the ratio of the rod diameters for the two lattices ($\beta = d_2/d_1$) and the tilt angle θ. We examine β values ranging from 0 to ∞, since β and β^{-1} no longer yield equivalent crystal structures. In Fig. 2-3, three different periodic structures that may be obtained by varying θ are shown. At $\theta = 0°$ [Fig. 2-3(a)] the structure becomes the double-rod square lattice. We also consider two other lattice positions, as shown in Figs. 2-3(b) and 2-3(c) at angles of 18.4° and 45°, respectively.

2.3 Theory and Photonic Band Gap Calculations

The propagation of electromagnetic waves through dielectric media is described by Maxwell's equations. These equations can be solved using a plane-wave expansion technique to yield the electromagnetic frequency spectra of waves in a periodic dielectric crystal.[17] To begin, Maxwell's equations are combined to give the wave equation in terms of the magnetic field $\mathbf{H}$

$$\nabla \times \left[\frac{1}{\varepsilon(\mathbf{x})} \nabla \times \mathbf{H} \right] = \frac{\omega^2}{c^2} \mathbf{H} \tag{2.2}$$

where $\varepsilon(\mathbf{x})$ is the position-dependent dielectric constant, ω is the frequency, and c is the speed of light in vacuum. The magnetic field $\mathbf{H}(\mathbf{x})$ and the dielectric function $\varepsilon(\mathbf{x})$ can be expanded in a sum of plane waves

$$\mathbf{H}(\mathbf{x}) = \sum_{\mathbf{G}} \sum_{\lambda=1,2} h_{\lambda,\mathbf{G}} \hat{\mathbf{e}}_{\lambda} e^{i(\mathbf{k}+\mathbf{G})\cdot\mathbf{x}} \tag{2.3}$$

$$\varepsilon(\mathbf{x}) = \sum_{\mathbf{G}} \kappa(\mathbf{G}) e^{i\mathbf{G}\cdot\mathbf{x}} \tag{2.4}$$

where $\mathbf{k}$ is the wave vector in the Brillouin zone and $\mathbf{G}$ is a reciprocal-lattice vector. The unit vectors $\hat{\mathbf{e}}_{\lambda}$ are magnetic wave polarizations orthogonal to $\mathbf{k} + \mathbf{G}$ and the coefficients $h_{\lambda,\mathbf{G}}$ are the corresponding components of the magnetic field. The Fourier coefficients $\kappa(\mathbf{G})$ are defined in the usual manner by

$$\kappa(\mathbf{G}) = \frac{1}{A_{cell}} \int_{A_{cell}} \varepsilon(\mathbf{x}) e^{-i(\mathbf{G}\cdot\mathbf{x})} d\mathbf{x} \tag{2.5}$$

where the integration is carried out over the area A_{cell} of one lattice unit cell.

In two-dimensions, the vectors $\mathbf{k} + \mathbf{G}$ always lie in the plane of the rods. Therefore, the unit vectors $\hat{\mathbf{e}}_1$, $\hat{\mathbf{e}}_2$ must either lie in the plane or along the z axis. This property allows us to rewrite Eq. (2.2) as two simpler equations, each describing a

particular wave polarization. For the magnetic field vector parallel to the axes of the rods (H-polarization), $h_{2,\mathbf{k}+\mathbf{G}} = 0$ for all $\mathbf{k}+\mathbf{G}$. Substituting the plane wave expansions into the wave equation gives an eigenvalue problem

$$\sum_{\mathbf{G}'} (\mathbf{k}+\mathbf{G}) \cdot (\mathbf{k}+\mathbf{G}') \eta(\mathbf{G}-\mathbf{G}') h_{1,\mathbf{k}+\mathbf{G}'} = \frac{\omega^2}{c^2} h_{1,\mathbf{k}+\mathbf{G}} \tag{2.6}$$

where $\eta(\mathbf{G}-\mathbf{G}')$ is a matrix found by inverting the $\kappa(\mathbf{G}-\mathbf{G}')$ matrix of coefficients defined in Eq. (2.5). By first expanding the dielectric function $\varepsilon(\mathbf{x})$ in a plane wave basis and then inverting the resulting matrix to obtain $\eta(\mathbf{G}-\mathbf{G}')$, faster convergence to the eigenvalues of Eq. (2.6) is achieved than by direct plane wave expansion of $\varepsilon^{-1}(\mathbf{x})$.[20]

For E-polarization the electric field vector is parallel to the rod axes and $\mathbf{H}(\mathbf{x})$ is in the rod plane. Here $h_{1,\mathbf{k}+\mathbf{G}} = 0$ for all $\mathbf{k}+\mathbf{G}$, yielding another eigenvalue problem:

$$\sum_{\mathbf{G}'} |\mathbf{k}+\mathbf{G}| \, |\mathbf{k}+\mathbf{G}'| \eta(\mathbf{G}-\mathbf{G}') h_{2,\mathbf{k}+\mathbf{G}'} = \frac{\omega^2}{c^2} h_{2,\mathbf{k}+\mathbf{G}} \tag{2.7}$$

Standard eigenvalue techniques are now used to solve Eqs. (2.6) and (2.7) to obtain the propagating wave frequencies for the corresponding polarizations.

In this formulation, all information pertaining to the geometry of the lattice is contained in the coefficient matrix η, or analogously the κ matrix. This provides a very convenient solving routine, as the bulk of the solution "machinery" remains in place, while only the κ coefficient matrix changes with different crystal structures.

The integral in Eq. (2.5) can be expanded and simplified to give

$$\kappa(\mathbf{G}) = \begin{cases} f\varepsilon_a + (1-f)\varepsilon_b, & \mathbf{G} = 0, \\ (\varepsilon_a - \varepsilon_b)\dfrac{1}{A_{cell}} \displaystyle\int_{A_{rod}} e^{-i(\mathbf{G}\cdot\mathbf{x})} d\mathbf{x}, & \mathbf{G} \neq 0. \end{cases} \tag{2.8}$$

The integral in the second part is now over the rods only. Here, f is the rod filling fraction, defined as $f = A_{rod}/A_{cell}$.

For the case of circular cross-section rods of radius r that do not overlap, the coefficients become

$$
\kappa(\mathbf{G}) = \begin{cases} f\varepsilon_a + (1-f)\varepsilon_b, & \mathbf{G} = 0, \\ (\varepsilon_a - \varepsilon_b)\sum_{\mathbf{T}} \dfrac{2\pi r J_1(Gr)}{A_{cell} G} e^{-i(\mathbf{G}\cdot\mathbf{T})}, & \mathbf{G} \neq 0. \end{cases}
$$

(2.9)

where J_1 is the first order Bessel function of the first kind and $G = |\mathbf{G}|$. The summation is over all rods inside one unit cell with positions described by translation vectors $\mathbf{T}$, measured from the origin of the coordinate axes. For example, consider the glide-symmetry square lattice shown in Fig. 2-3(b). There are four rods in the unit cell, located at positions described by the translation vectors

$$
\mathbf{T}_1 = \frac{3}{8}\mathbf{a}_1 + \frac{1}{8}\mathbf{a}_2
$$

$$
\mathbf{T}_2 = -\frac{1}{8}\mathbf{a}_1 + \frac{3}{8}\mathbf{a}_2
$$

$$
\mathbf{T}_3 = -\frac{3}{8}\mathbf{a}_1 - \frac{1}{8}\mathbf{a}_2
$$

$$
\mathbf{T}_4 = \frac{1}{8}\mathbf{a}_1 - \frac{3}{8}\mathbf{a}_2
$$

(2.10)

Substituting these vectors into Eq. (2.9) and simplifying yields

$$
\kappa(\mathbf{G}) = \begin{cases} f\varepsilon_a + (1-f)\varepsilon_b, & \mathbf{G} = 0, \\ (\varepsilon_a - \varepsilon_b)\dfrac{4\pi r J_1(Gr)}{A_{cell} G}\left[\cos(\dfrac{a}{8}(3g_1 + g_2)) + \cos(\dfrac{a}{8}(g_1 - 3g_2))\right], & \mathbf{G} \neq 0. \end{cases}
$$

(2.11)

Here g_1 and g_2 (integers, denoted collectively by g) are components of the reciprocal lattice vector defined by

$$
\mathbf{G}(g) = \frac{2\pi}{a^2}g_1\mathbf{a}_1 + \frac{2\pi}{a^2}g_2\mathbf{a}_2.
$$

(2.12)

The results that follow were obtained using 729 plane waves for the single-rod square lattice, and 1225 plane waves for the double-rod square lattice and the glide-symmetry square lattice. A greater number of plane waves was required to maintain accuracy for the latter cases due to a more complex unit cell arrangement. The results were tested using 1757 plane waves, for which the band frequencies differed from those calculated with fewer plane waves by a maximum of 0.8%. Most bands differed by less than 0.5%. Thus, we believe that all of the results reported here are accurate to within at least 1% of their true values. The results of the accuracy test also seem to suggest that band calculations with significantly fewer plane waves will not meet the 1% accuracy condition.

2.4 Photonic Band Gap Results

We first examine the single-rod square lattice of air holes in a different dielectric background.[18,21,22] The dispersion relation for a background material with dielectric constant $\varepsilon_b = 11.4$ (ε_{GaAs} at $\lambda \approx 1.5$ μm) and a rod filling fraction of $f = 0.77$ is shown in Fig. 2-4. The figure inset shows the irreducible portion of the Brillouin zone and the corresponding lattice symmetry points. An absolute band gap does exist for this structure, which is produced by an overlap of the H_2 and E_3 band gaps.[†] It is bounded on the lower side by the H-polarization gap boundary, and on its upper side by the E-polarization gap. A summary of our calculations for the single-rod square lattice is shown in the "gap map" of Fig. 2-5, where non-dimensionalized frequencies are plotted as a function of the filling fraction. An absolute band gap appears at filling fractions between 0.68 and 0.79, and has a maximum value of $\Delta\omega = 0.0188(2\pi c/a)$ at $f = 0.77$.

[†] A gap for a particular polarization bounded by the nth and $(n+1)$th frequency bands is designated with subscript n.

As the rod filling fraction nears the closed-packed condition ($f = 0.785$ for a square lattice of circular rods), the rods in the structure begin to touch and the absolute band gap quickly disappears. The frequency band plot of Fig. 2-6 for $f = 0.8$ demonstrates that the size of the absolute band gap is limited because the second, third, and fourth H-polarization bands are degenerate at the **M** point of the Brillouin zone. If this band degeneracy can be lifted while maintaining (or increasing) the size of the E-polarization gap, a larger absolute band gap will ensue. By placing a smaller diameter rod at the center of each square unit cell (as shown in Fig. 2-1), the crystal symmetry is reduced. The effect of this symmetry reduction on the square lattice dispersion relation is shown in Fig. 2-7, where a rod with diameter ratio $\beta = 0.16$ has been added to the structure for the same total filling fraction $f = 0.8$. The H-polarization degeneracy has been lifted, resulting in a much larger H-polarization gap. Remarkably, the upper E-polarization gap is also greatly enlarged. Thus, the overlap between the two gaps increases, resulting in a much larger absolute band gap. The gap map for the double-rod square lattice when $\beta = 0.16$ is shown in Fig. 2-8. The maximum absolute band gap for the double-rod square structure occurs when $\beta = 0.16$ and $f = 0.793$. With a gap width of $\Delta\omega = 0.0548(2\pi c/a)$, this photonic band gap is nearly *three times* larger than the best value obtained for the single-rod square lattice case.

The effect of symmetry reduction on the size and position of the band gaps may be more dramatically demonstrated by generating a gap map as a function of β. Figure 2-9 illustrates such a gap map for the double-rod square lattice at a filling fraction of 0.793. The band gaps for the single-rod square lattice are obtained when $\beta = 0$ or, equivalently, unity.[†] There are no absolute band gaps present for $\beta = 0$ at this filling fraction. As β is increased, a complex gap map unfolds as a result of symmetry breaking. Both the H_2 and E_3 gaps substantially widen and overlap to produce an absolute band gap with maximum

---

[†] When $\beta = 1$, the gap positions are shifted by a factor of $\sqrt{2}$ as a result of the change in the unit cell size.

width at $\beta = 0.16$. A smaller absolute gap also forms at $\beta \approx 0.5$. Several other gaps in both E- and H-polarizations appear and disappear as β is varied.

Extensive calculations have shown that both the filling fraction and the size of the symmetry breaking element are important factors in dictating which crystal arrangements will possess absolute photonic band gaps. In Ref. 23, it was shown that the region of filling fractions where the rods begin to touch or overlap is a critical region of the band gap spectrum, where many band gaps begin to close or open up. Furthermore, it was shown that a connected lattice arrangement was important in the production of H-polarization gaps. The introduction of small rods into the unit cell may work to create larger absolute band gaps by increasing the total rod filling fraction to regimes where large gaps occur, without suffering the consequences of disrupting the lattice connectivity.

Though we have managed to greatly increase the size of the absolute band gap for the square lattice arrangement of holes in dielectric, the resulting structure may not be practical for device applications. The maximum absolute gap condition has a very large filling fraction, $f = 0.793$. For a midgap wavelength of 1500 nm (near-IR), the dielectric walls between adjacent holes will be as thin as 6 nm. The precise microfabrication of such small features is extremely difficult. In fact, the results of several studies have shown that to open an absolute photonic band gap in a crystal of air columns in a background dielectric requires the rod filling fraction to always be near the close-packed condition.[9,24-26] Therefore, if we are to identify photonic crystal structures which possess large absolute gaps and can also be easily fabricated, we must consider the opposite arrangement, namely that of dielectric rods in air. It has been shown[25] that for the single-rod square lattice, no absolute gaps occur for the case of dielectric rods in air due to the complete absence of an H-polarization gap. In addition, we have searched all filling fractions of the double-rod square lattice [see Fig. 2-3(a)] of dielectric rods in air. A gap map for a filling fraction of 0.33 is shown in Fig. 2-10(a), where non-dimensionalized

frequencies are plotted as a function of the rod diameter ratio β. Values of β greater than 1 yield the same structures as those at β^{-1}. The gap map is filled with many large E-polarization gaps that open and close as the rod diameter ratio is varied. The gaps tend to decrease in size at higher frequencies. An interesting feature of this gap map is the presence of "defect-like" modes occurring between adjacent E-polarization gaps at high frequencies and low values of β. Three such defect modes are indicated by the horizontal arrows in the figure. In each case, a narrow frequency band appears along the length of a seemingly single E-polarization gap, splitting it in two and creating the isolated mode. From a different perspective, this observation could also be interpreted as follows: the two dissimilar rod sizes in the double-rod square lattice may act as a very regular pattern of defects, creating singular frequency pass-bands contained within a band gap. In contrast to the abundance of large E-polarization gaps, only a few small H-polarization gaps exist. The largest H-polarization gaps occur at high frequencies for values of β near 1, but these do not overlap with any E-polarization gaps. The largest absolute gap for the double-rod case was found for a filling fraction of 0.33 and $\beta = 0.57$. However, the gap is fairly small, having a maximum width of $\Delta\omega = 0.0280(2\pi c/a)$ at a non-dimensionalized mid-gap frequency of 0.752. Thus, other ways must be sought to reduce the symmetry of the square lattice to find arrangements which yield larger absolute band gaps.

The glide-symmetry structure with $\theta = 18.4°$, shown in Fig. 2-3(b), accomplishes a more severe symmetry reduction than that for the double-rod lattice, as mirror planes along major symmetry axes have been eliminated. This symmetry reduction opens several large H-polarization gaps and yields three large absolute band gaps. Band frequency calculations for this structure were performed along the symmetry lines forming the edges of the irreducible 1/8 of the Brillouin zone. The existence of band gaps was confirmed by density of states calculations using uniformly spaced $\mathbf{k}$ points in the entire first Brillouin zone. The calculations are summarized in the gap map shown in Fig. 2-10(b) at a filling fraction of 0.33. In this figure, the single-rod lattice is recovered

when $\beta = 0$. The lowest frequency gap occurs at intermediate values of β, and is entirely limited by the size of the H-polarization gap that opens inside an existing E-polarization gap. This gap is formed by the overlap of H_6 and E_{10} gaps,[23] and has a maximum width of $0.0757(2\pi c/a)$ at $f = 0.3$ and $\beta = 0.55$. Two other absolute gaps form at and near the equal rod diameter condition. The H-polarization gaps (H_{10} and H_{14}) share one E-polarization gap (E_{18}). The lower frequency gap has a maximum width of $0.0741(2\pi c/a)$ at $f = 0.33$ and $\beta = 1$, while the upper gap maximum is $0.0762(2\pi c/a)$ at $f = 0.33$ and $\beta = 1.05$. It is interesting to note that similar gaps do not exist for the double-rod lattice [Fig. 2-10(a)]. An additional degree of symmetry reduction (accomplished through the introduction of the glide symmetry operation) was necessary to open the new absolute gaps. As all three absolute gaps for the glide-symmetry lattice have similar maximum widths, we can choose which gap to utilize for experimental purposes. From a fabrication standpoint it may be easier to utilize the highest frequency absolute gap. For equal size rods the filling fraction is given by $f = n\pi r^2/a^2$, where n is the number of rods in the unit cell. Therefore, for a given filling fraction the rod radius scales with a, and is inversely proportional to $\sqrt{n}$. With six rods in each glide-symmetry lattice unit cell, it is especially important to make the lattice parameter a as large as possible to increase the smallest feature dimension. However, it has also been shown that higher frequency gaps are more sensitive to random lattice disorder than those at lower frequencies.[27] Since the introduction of a certain amount of disorder during fabrication is probable, especially for small-size features, this may also affect the choice of absolute band gap.

Continuing the study of the symmetry reduction argument, we have also examined the structure shown in Fig. 2-3(c). The primitive unit cell for this structure contains six rods, as does the previous case, but now the rods line up in diagonal rows ($\theta = 45°$). After searching all filling fractions and rod diameter ratios of dielectric rods in air, no absolute photonic band gaps were found for this structure. A gap map is shown in Fig. 2-10(c) for a filling fraction of 0.33. Several large E-polarization gaps exist, but only one small H-

polarization gap opens up and does not overlap the E-polarization gaps. The lack of absolute gaps makes sense in light of the fact that this crystal structure belongs to the plane group *p4mm*, as do the single-rod and double-rod lattices. All of the *p4mm* symmetry crystals of dielectric rods in air have very small (or absent) H-polarization gaps.

Striking differences may be seen in comparing the three gap maps of Fig. 2-10. The most symmetric structure, that of Fig. 2-10(a), possesses the greatest number of large band gaps, albeit for only one polarization. This structure also exhibits defect-like modes in some of the upper E-polarization gaps, a characteristic not seen in the other lattices studied here. It is easy to create E-polarization gaps in ordered crystals comprising of dielectric rods in air. These gaps are usually quite large and robust with respect to changes in the crystal structure.[27] The challenge is to force H-polarization gaps to open at frequencies that overlap with the E-polarization gaps. Introduction of the glide-symmetry operation in Fig. 2-10(b) has succeeded in this more difficult task, opening three large H-polarization gaps. Some of the E-polarization gaps—present in the more symmetric case—have been eliminated by this reduction in lattice symmetry, but several large gaps survive to create absolute band gaps. In Fig. 2-10(c), ordered rows of rods are separated with pockets of empty space. The hardy E-polarization gaps remain, though only one small H-polarization gap exists. The remarkable evolution of gaps occurs simply by changing the tilt angle, θ.

Our analysis suggests that the best *4mm*-group-based structure for obtaining large absolute band gaps with dielectric columns in air is the structure with glide symmetry, shown in Fig. 2-3(b). Removing the mirror plane symmetries along the principal axes of the square lattice (present in the *p4mm* plane group but not in *p4gm*) contributes to the opening of H-polarization gaps, and ultimately produces large absolute band gaps. At first glance, it might seem unlikely that the glide structure would have any gaps at all. However, there are many symmetry operations present within this structure, which

apparently are enough to allow gaps to open. This example illustrates the power of the symmetry-reduction idea—it provides a rational way to identify new structures with absolute band gaps that might have otherwise been overlooked. Indeed, it is doubtful as to whether the structure of Fig. 2-3(b) would have been studied without this motivation.

2.5 Discussion

Though we have explored a method for systematically identifying new photonic crystal structures, we have not yet detailed a quantitative connection between the degree of symmetry reduction and the size of the absolute photonic gap. Such a relationship—if it exists—would be immensely beneficial for the design of photonic crystals. Other researchers have also searched for the link between crystal properties and band gap opening in an attempt to explain and predict the occurrence of photonic band gaps. Joannopoulos et al.[25] studied electromagnetic fields and lattice connectivity to understand photonic gap openings. Cassagne et al.[26] have investigated the opening of gaps for 2D hexagonal structures using a perturbative approach. Although these investigations shed light into how gap opening occurs, they also fall short of providing physical rules for selecting the optimal structure. Ideally, deciphering the connection between symmetry reduction and band overlap should enable one to determine the crystal arrangement that yields the maximum absolute band gap for a given dielectric contrast. For the single-rod square lattice, we have seen that band degeneracies at a high symmetry point in the crystal can be lifted by reducing the lattice symmetry. However, we lack an *a priori* understanding as to what "degree" the symmetry should be broken to maximize the photonic gaps. Photonic crystal modeling is analogous in many ways to electronic crystal modeling. Though several methods exist for calculating properties of crystals of atoms, these methods do not allow one to exactly determine the ideal structure to optimize a given property (e.g., hardness). Instead, one must first propose a structure and then

calculate its crystal properties to determine if the goal has been met. However, judicious guesses of promising structures greatly assist in the study of these materials. In photonic crystal modeling, symmetry reduction can, at the least, be considered as a guiding principle to the design of new photonic structures.

2.6 Summary and Conclusions

We have shown that the size of absolute photonic band gaps in two-dimensional square lattices can be significantly increased by reducing the lattice symmetry. Specifically, two interpenetrating square lattices with different diameter rods can yield photonic crystals with gaps significantly larger as compared to the single-rod lattice with the same dielectric contrast. For air holes in a background medium of GaAs ($\varepsilon = 11.4$), the maximum gap size of the double-rod square lattice was nearly three times the size of the best single-rod lattice band gap at the same dielectric contrast. However, absolute band gaps for crystals of air rods in background dielectric occur at high filling fractions, resulting in thin-walled structures that are difficult to fabricate. This problem may be avoided by fabricating photonic crystals of dielectric rods in air. However, no photonic band gaps exist for either the single-rod or double-rod lattices of dielectric rods in air. By removing the mirror planes of the single-rod lattice geometry through the introduction of the glide symmetry operation, crystals with large absolute band gaps have been obtained. These band gaps occur at moderate filling fractions (≈ 0.35) and thus should be easier to fabricate than those of holes in dielectric. Lattice symmetry reduction provides a guiding principle towards a more rational design of 2D photonic crystals, and might also be successfully applied for band gap engineering in 3D photonic crystals.

Acknowledgments

2.7 References

[1]   E. Yablonovitch, "Inhibited Spontaneous Emission in Solid-State Physics and Electronics," *Phys. Rev. Lett.* **58**, 2059 (1987).

[2]   S. John, "Strong Localization of Photons in Certain Disordered Dielectric Superlattices," *Phys. Rev. Lett.* **58**, 2486 (1987).

[3]   R. D. Meade, K. D. Brommer, A. M. Rappe, and J. D. Joannopoulos, "Photonic Bound States in Periodic Dielectric Materials," *Phys. Rev. B* **44**, 13772 (1991).

[4]   E. Yablonovitch, T. J. Gmitter, R. D. Meade, A. M. Rappe, K. D. Brommer, and J. D. Joannopoulos, "Donor and Acceptor Modes in Photonic Band Structure," *Phys. Rev. Lett.* **67**, 3380 (1991).

[5]   S. L. McCall, P. M. Platzman, R. Dalichaouch, D. Smith, and S. Schultz, "Microwave Propagation in Two-Dimensional Dielectric Lattices," *Phys. Rev. Lett.* **67**, 2017 (1991).

[6]   E. Yablonovitch and T. Gmitter, "Photonic Band Structure: The Face-Centered-Cubic Case," *Phys. Rev. Lett.* **63**, 1950 (1989).

[7]   E. Yablonovitch, T. Gmitter, and K. M. Leung, "Photonic Band Structure: The Face-Centered-Cubic Case Employing Nonspherical Atoms," *Phys. Rev. Lett.* **67**, 2295 (1991).

[8]   E. Özbay, A. Abeyta, G. Tuttla, M. Tringides, R. Biswas, C. T. Chan, C. M. Soukoulis, and K. M. Ho, "Measurement of a Three-Dimensional Photonic Band Gap in a Crystal Structure Made of Dielectric Rods," *Phys. Rev. B* **50**, 1945 (1994).

[9]   R. D. Meade, K. D. Brommer, A. M. Rappe, and J. D. Joannopoulos, "Existence of a Photonic Band Gap in Two Dimensions," *Appl. Phys. Lett.* **61**, 495 (1992).

[10]   W. M. Robertson, G. Arjavalingam, R. D. Meade, K. D. Brommer, A. M. Rappe, and J. D. Joannopoulos, "Measurement of Photonic Band Structure in a Two-Dimensional Periodic Dielectric Array," *Phys. Rev. Lett.* **68**, 2023 (1992).

[11]   S. Y. Lin, G. Arjavalingam, and W. M. Robertson, "Investigation of Absolute Photonic Band Gaps in Two-Dimensional Dielectric Structures," *J. Mod. Opt.* **41**, 385 (1994).

34

[12] T. F. Krauss, R. M. De La Rue, and S. Brand, "Two-Dimensional Photonic-Bandgap Structures Operating at Near-Infrared Wavelengths," *Nature* **383**, 699 (1996).

[13] U. Grüning, V. Lehmann, S. Ottow, and K. Busch, "Macroporous Silicon with a Complete Two-Dimensional Photonic Band Gap Centered at 5 μm," *Appl. Phys. Lett.* **68**, 747 (1996).

[14] K. Inoue, M. Wada, K. Sakoda, M. Hayashi, T. Fukushima, and A. Yamanaka, "Near-Infrared Photonic Band Gap of Two-Dimensional Triangular Air-Rod Lattices as Revealed by Transmittance Measurement," *Phys. Rev. B* **53**, 1010 (1996).

[15] H.-B. Lin, R. J. Tonucci, and A. J. Campillo, "Observation of Two-Dimensional Photonic Band Behavior in the Visible," *Appl. Phys. Lett.* **68**, 2927 (1996).

[16] D. L. Bullock, C. Shih, and R. S. Margulies, "Photonic Band Structure Investigation of Two-Dimensional Bragg Reflector Mirrors for Semiconductor Laser Mode Control," *J. Opt. Soc. Am. B* **10**, 399 (1993).

[17] K. M. Ho, C. T. Chan, and C. M. Soukoulis, "Existence of a Photonic Gap in Periodic Dielectric Structures," *Phys. Rev. Lett.* **65**, 3152 (1990).

[18] C. M. Anderson and K. P. Giapis, "Larger Two-Dimensional Photonic Band Gaps," *Phys. Rev. Lett.* **77**, 2949 (1996).

[19] *International Tables for Crystallography*, edited by T. Hahn, D. Reidel Publishing Company, Boston (1987).

[20] P. R. Villeneuve and M. Piché, "Photonic Bandgaps: What is the Best Numerical Representation of Periodic Structures?" *J. Mod. Opt.* **41**, 241 (1994).

[21] M. Plihal, A. Shambrook, A. A. Maradudin, and P. Sheng, "Two-Dimensional Photonic Band Structures," *Optics Comm.* **80**, 199 (1991).

[22] P. R. Villeneuve and M. Piché, "Photonic Band Gaps in Two-Dimensional Square Lattices: Square and Circular Rods," *Phys. Rev. B* **46**, 4973 (1992).

[23] J. N. Winn, R. D. Meade, and J. D. Joannopoulos, "Two-Dimensional Photonic Band-Gap Materials," *J. Mod. Opt.* **41**, 257 (1994).

[24] P. R. Villeneuve and M. Piché, "Photonic Band Gaps in Two-Dimensional Square and Hexagonal Lattices," *Phys. Rev. B* **46**, 4969 (1992).

[25] J. D. Joannopoulos, R. D. Meade, and J. N. Winn, *Photonic Crystals* (Princeton University Press, Princeton, 1995).

[26] D. Cassagne, C. Jouanin, and D. Bertho, "Hexagonal Photonic-Band-Gap Structures," *Phys. Rev. B* **53**, 7134 (1996).

[27] M. M. Sigalas, C. M. Soukoulis, C.-T. Chan, and D. Turner, "Localization of Electromagnetic Waves in Two-Dimensional Disordered Systems," *Phys. Rev. B* **53**, 8340 (1996).
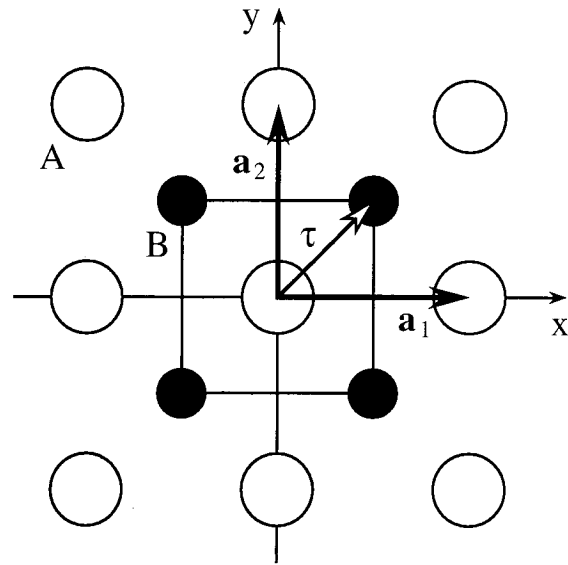
Fig. 2-1. The two-dimensional single-rod (sites labeled A) and double-rod (sites A and B) square structures, showing the unit cell and the primitive lattice translation vectors.
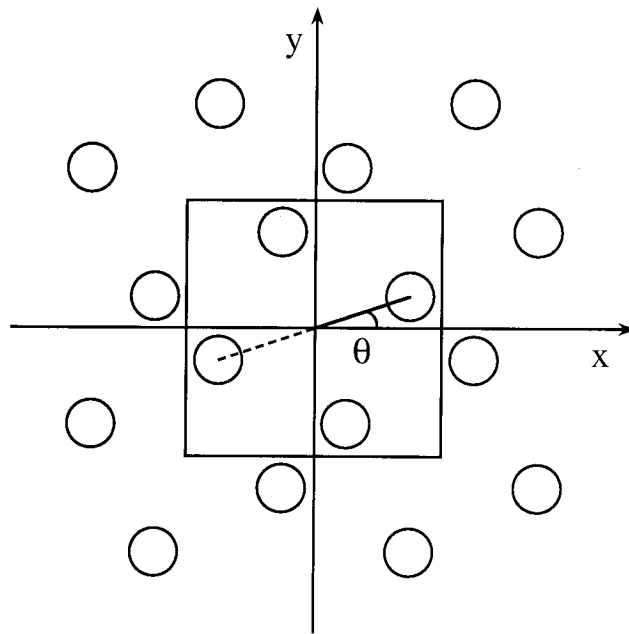
Fig. 2-2. The two-dimensional glide-symmetry square lattice, with the unit cell indicated. The rod arrangements may be rotated by varying the angle θ to obtain various structures.
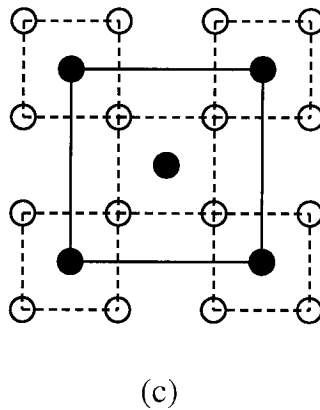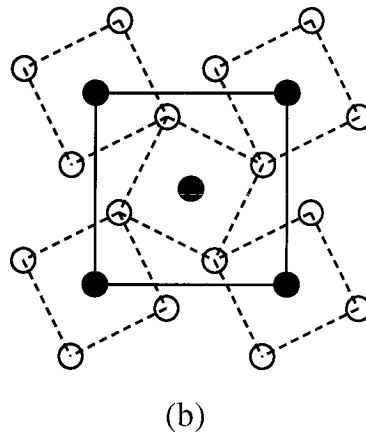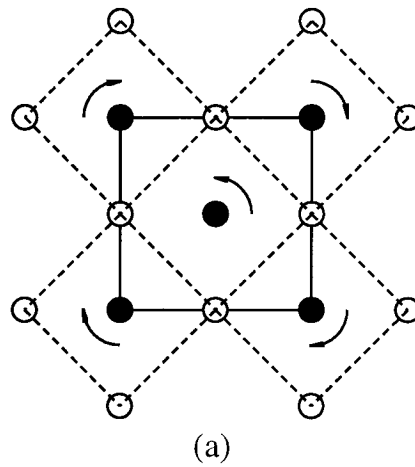
(a)

(b)

(c)

Fig. 2-3. Two-dimensional square structures produced at tilt angles (a) $\theta = 0°$, (b) $\theta = 18.4°$, and (c) $\theta = 45°$. The arrangement in (a) is the double-rod structure ($p4mm$), shown with a larger unit cell. The arrows in (a) illustrate the direction of rotation—accompanied by lattice compression—that is performed to obtain the glide-symmetry square lattice (group $p4gm$) in (b). Further rotation and compression produces the group $p4mm$ structure in (c).
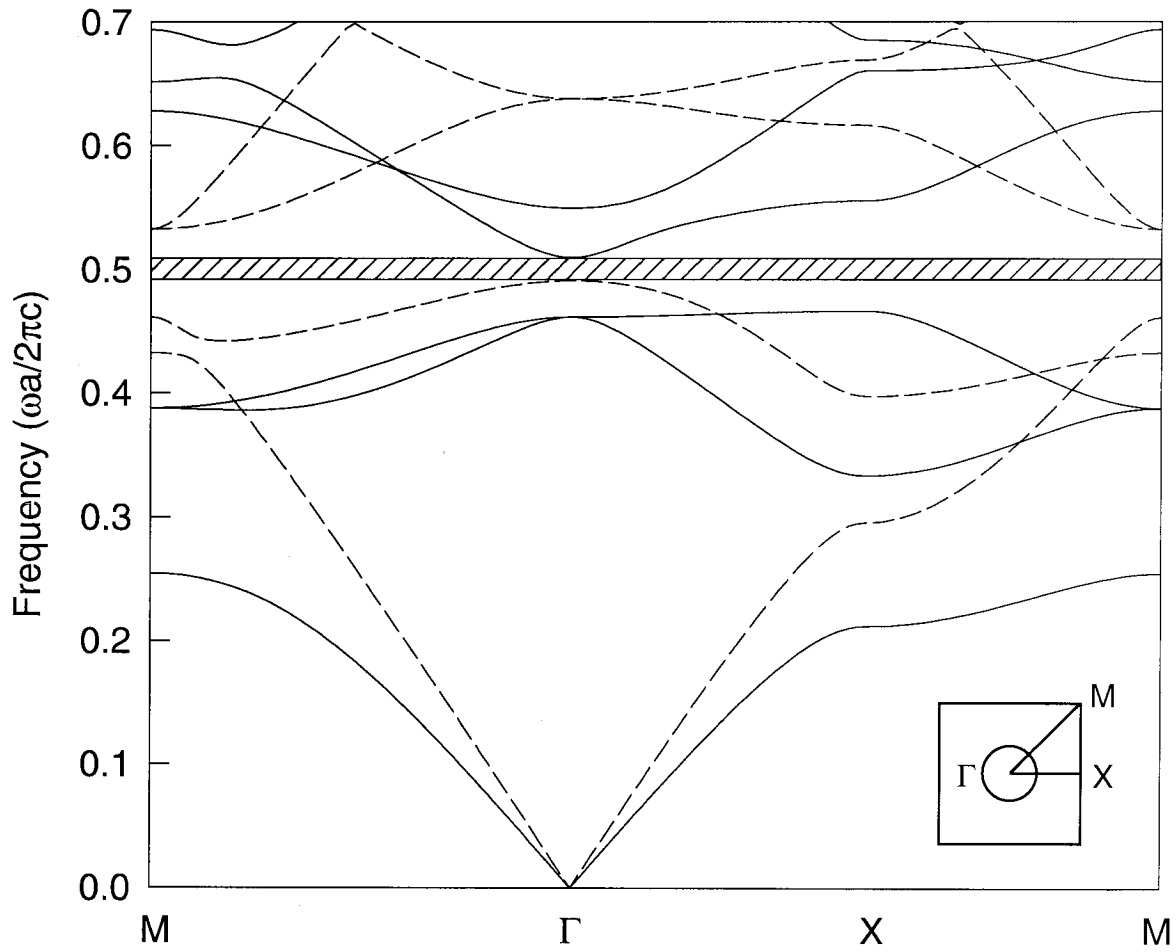
Fig. 2-4. Frequency band plot for the single-rod square lattice of holes ($f = 0.77$) in a background dielectric ($\varepsilon_b = 11.4$). E-polarization modes are shown by the solid lines, and H-polarization modes by the dashed lines. The H_2 and E_3 gaps overlap to produce an absolute band gap (crosshatched region) of width $0.0188(2\pi c/a)$.
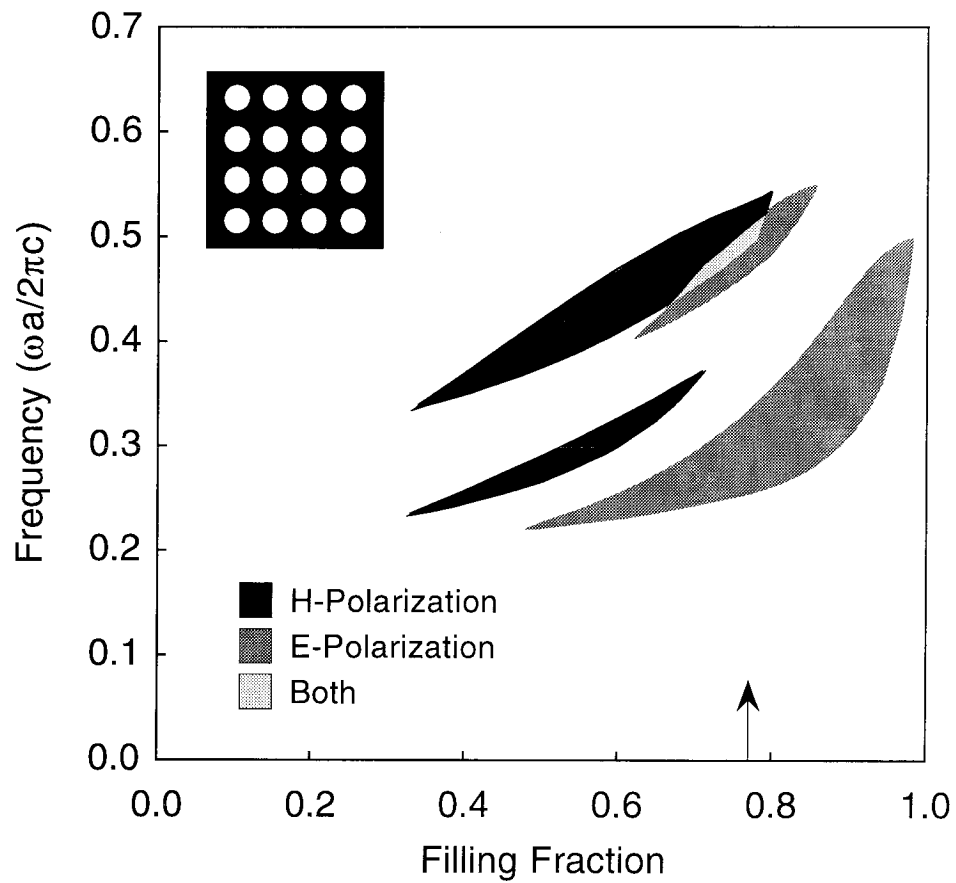
Fig. 2-5. Gap map for the single-rod square lattice of air holes in a background dielectric ($\varepsilon_b = 11.4$). An absolute band gap occurs where the upper two polarization gaps overlap. The maximum gap occurs at $f = 0.77$ (indicated by the arrow).
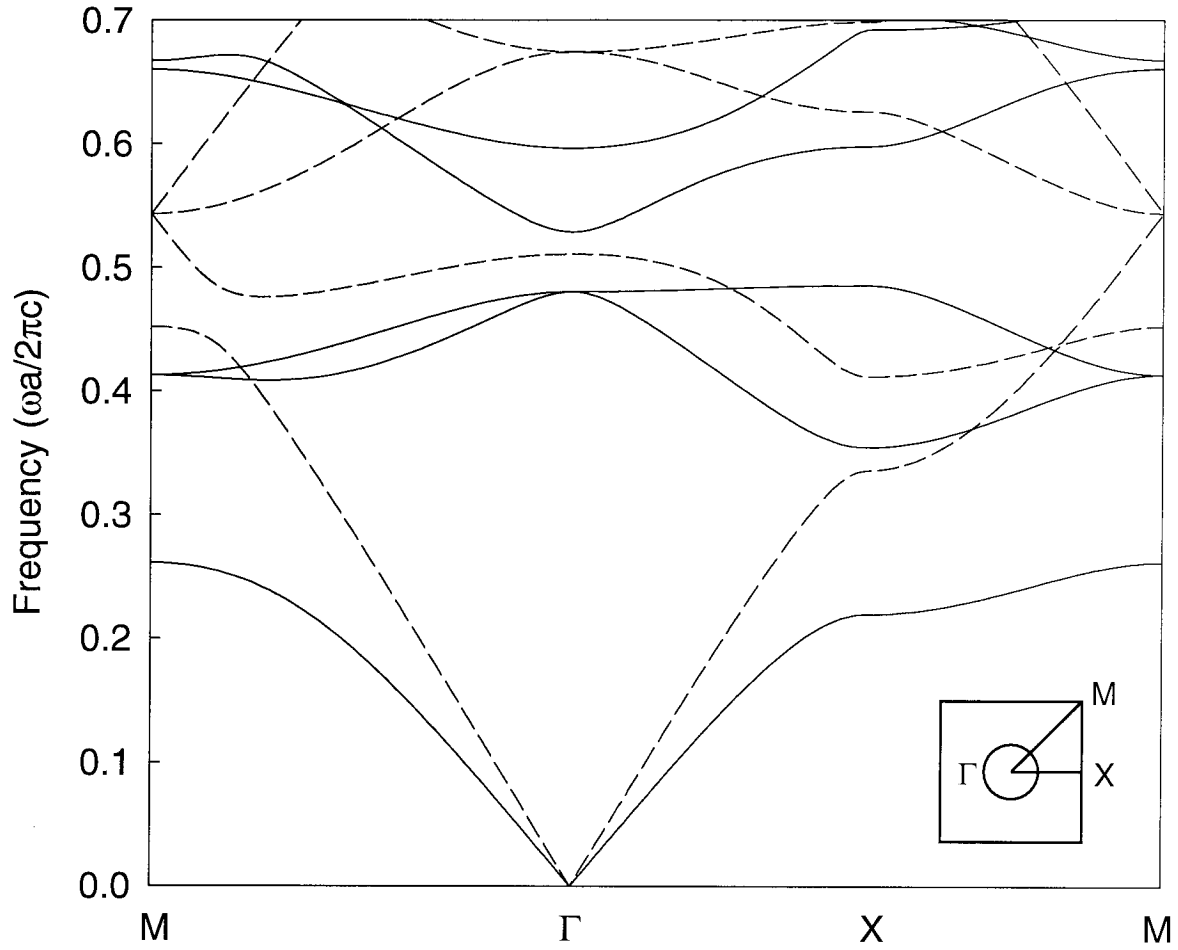
Fig. 2-6. Frequency band plot for the single-rod square lattice of holes ($f = 0.8$) in a background dielectric ($\varepsilon_b = 11.4$). E-polarization modes are shown by the solid lines, and H-polarization modes by the dashed lines. The absolute band gap disappears at large filling fractions due to an H-polarization band degeneracy at lattice symmetry point **M**.
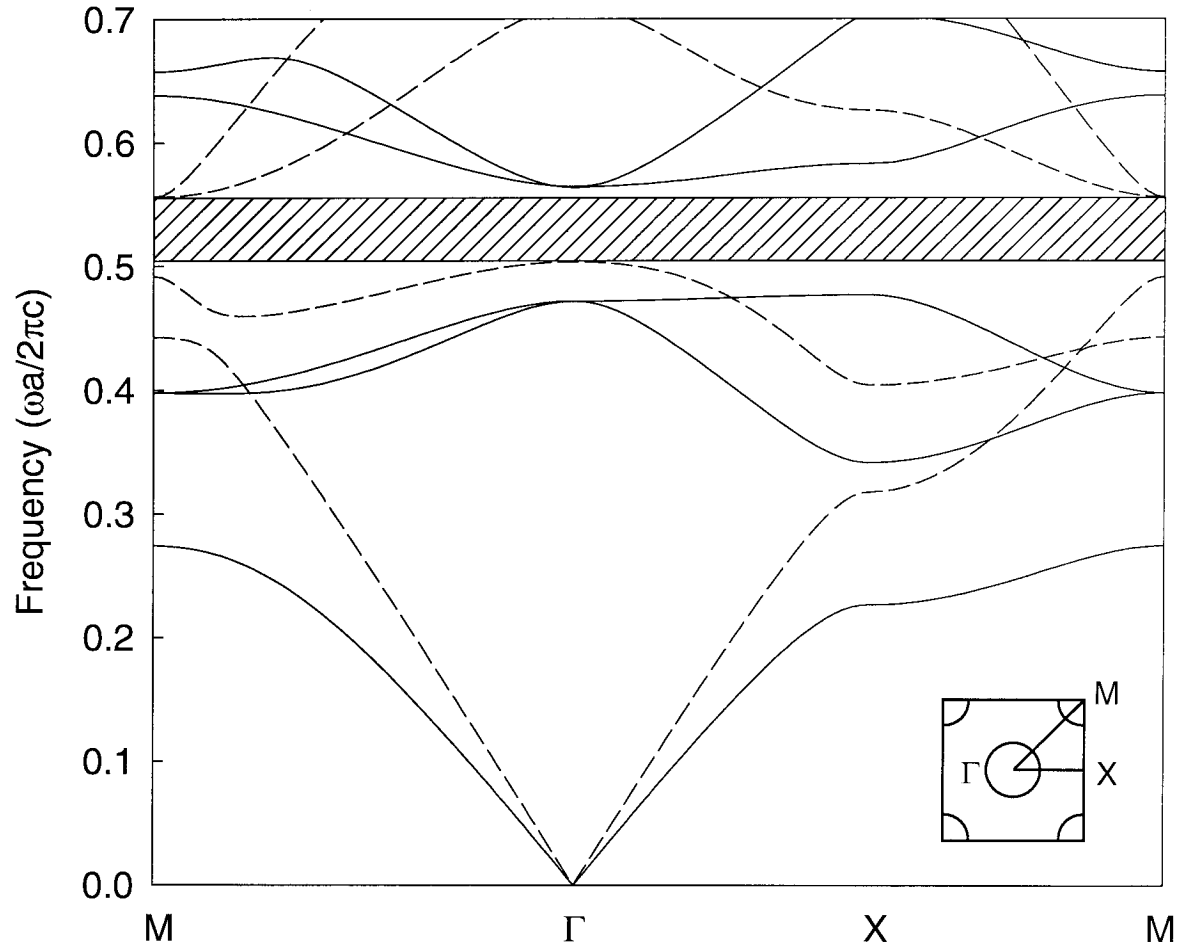
Fig. 2-7. Frequency band plot for the double-rod square lattice of holes in background dielectric (ε_b=11.4), with f=0.8 and β=0.16. Reducing the lattice symmetry by introducing an additional rod into the unit cell lifts the H-polarization (dashed lines) degeneracy while maintaining a large E-polarization (solid lines) gap, resulting in a large absolute band gap (crosshatched region).
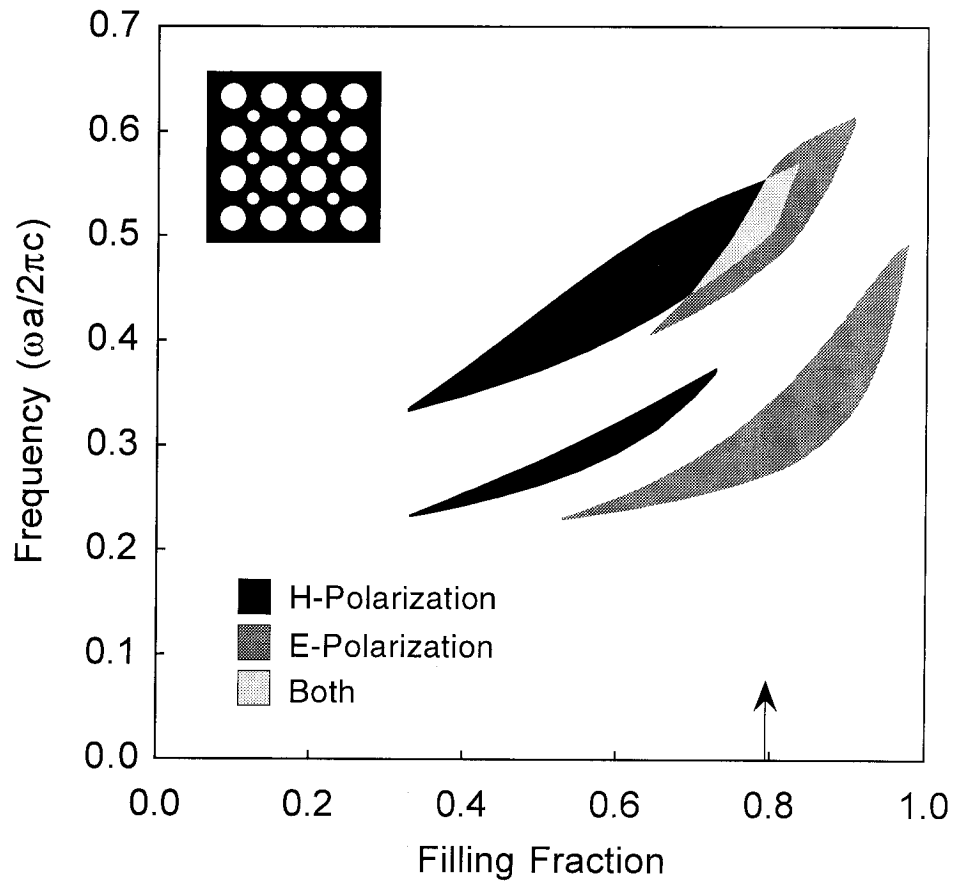
Fig. 2-8. Gap map for the double-rod square lattice ($\beta = 0.16$) of air holes in a background dielectric ($\varepsilon_b = 11.4$), showing a significantly larger absolute band gap than that for the single-rod lattice. The maximum gap of $0.0548(2\pi c/a)$ occurs at a filling fraction of 0.793 (indicated by the arrow).
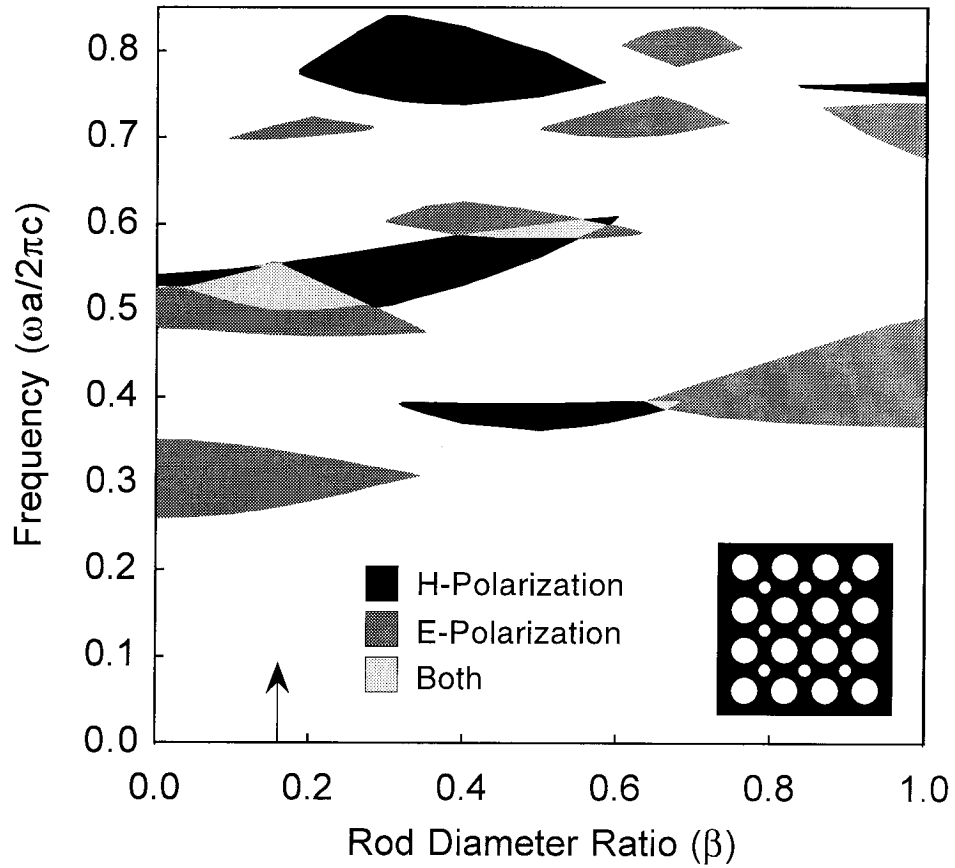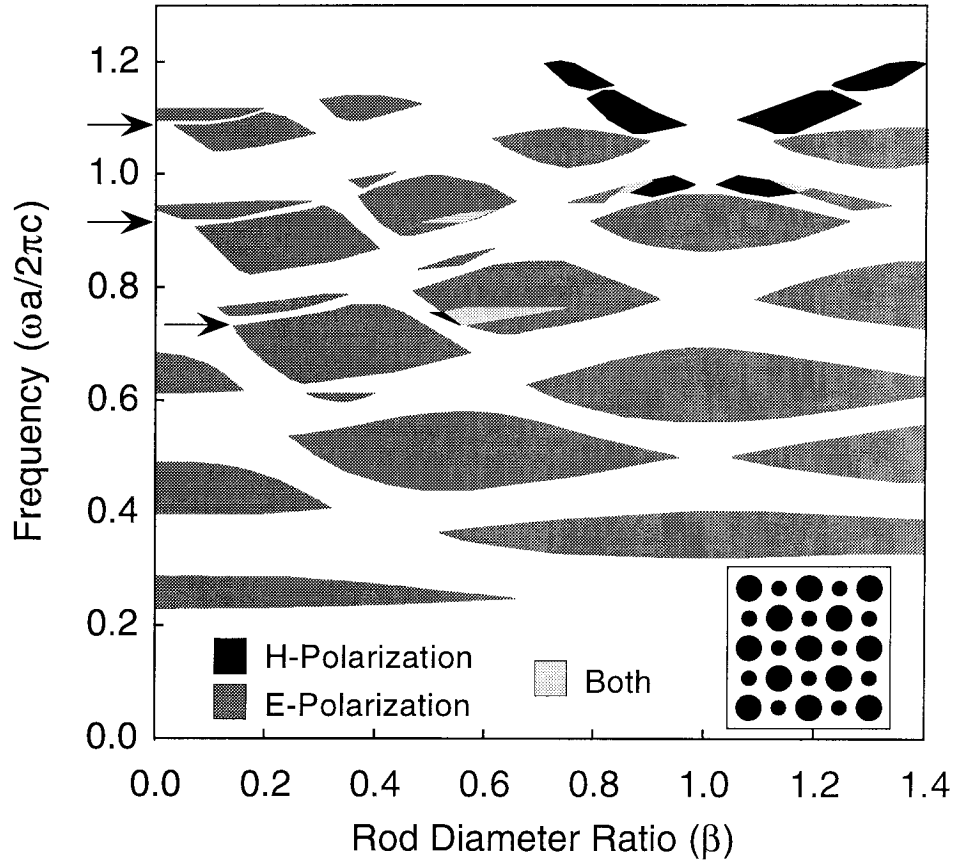
Fig. 2-9. Gap map for the double-rod square lattice ($f = 0.793$) of air holes in a background dielectric ($\varepsilon_b = 11.4$) as a function of β. Lattice symmetry reduction increases gap sizes for both polarizations to yield absolute band gaps. The largest absolute gap occurs at $\beta = 0.16$ (arrow).

Fig. 2-10. Gap maps for two-dimensional square structures of dielectric rods ($\varepsilon_a = 11.4$) in air produced at tilt angles (a) $\theta = 0°$, (b) $\theta = 18.4°$, and (c) $\theta = 45°$. The lattice filling fraction in each case is $f = 0.33$. The structures in (a) and (c) belong to plane group *p4mm*, and have limited H-polarization gaps. Only the arrangement in (b) possesses the glide symmetry operation (group *p4gm*), which opens several large H-polarization gaps to produce three absolute band gaps. The largest gap (indicated by the vertical arrow) has a maximum width of $0.0762(2\pi c/a)$ at $\beta = 1.05$. Horizontal arrows in (a) point to defect-like modes present within the E-polarization gaps.
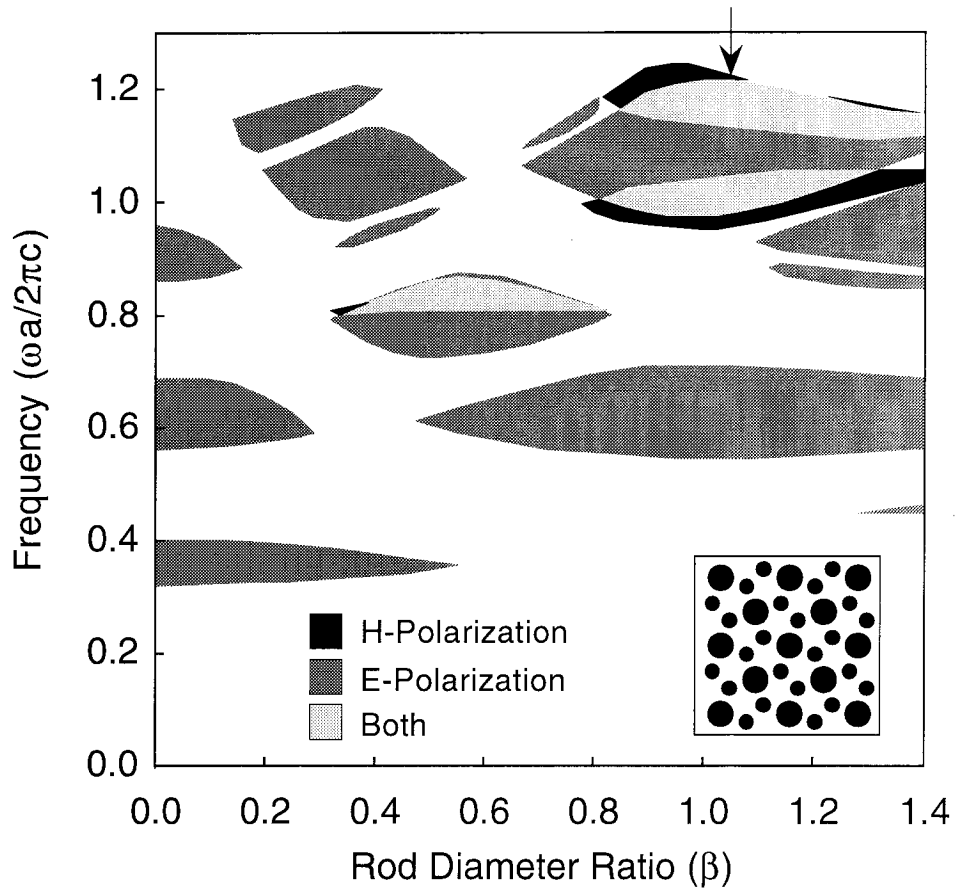
(b)

Fig. 2-10. (Continued.)
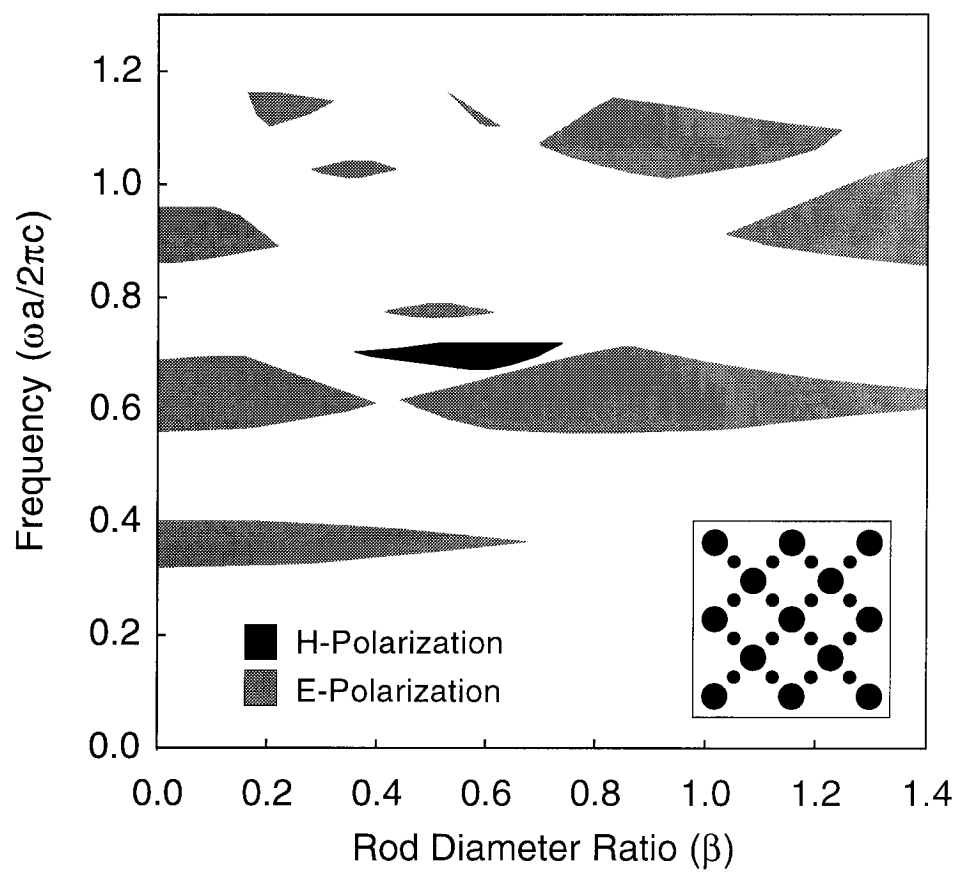
Fig. 2-10. (Continued.)

CHAPTER 3

A Comprehensive Guide to Two-Dimensional Hexagonal Photonic Crystals

Abstract

We present an overview of the hexagonal two-dimensional photonic crystal structures that form the Laue symmetry group *6mm*. This symmetry group contains two of the most widely utilized crystal structures in experiments, the triangular and honeycomb structures. Using a symmetry-based approach, we compare the band gap properties of several structures that fall within the *6mm* class. For crystals formed of air columns in a high dielectric background, the triangular lattice is the optimal arrangement for the largest absolute band gap. The converse arrangement of dielectric rods in air achieves its maximum band gap in the reduced symmetry triangular arrangement, composed of a hexagonal lattice interpenetrated by a triangular one with smaller diameter rods. Gap maps for several important crystal structures are presented as a reference guide for experimentalists.

3.1 Introduction

A decade old now, the idea of photonic band gap (PBG) crystals[1,2] has matured into a research field of its own. Demonstrations of the feasibility of microfabricating such crystals in two[3-6] and three[7-9] dimensions continue to stimulate investigations into their applications as well as their fundamental properties. An understanding of PBG crystal properties is essential not only for developing new optical devices but also for judiciously choosing the best crystal for a particular application. The design of photonic crystals, with specific properties defined *a priori*, remains elusive and presents a considerable theoretical challenge.

One of the goals of modeling the electromagnetic wave propagation through periodic dielectric media has been the identification of crystalline structures that possess large absolute photonic band gaps, most suitable for applications. Many 2D structures based on the simple Bravais lattices have been studied and some have been shown to possess absolute band gaps.[10-16] Often such investigations were not performed with ease of microfabrication in mind; indeed, some structures with sizable gaps pose considerable obstacles to microfabrication. For example, the triangular structure of circular cross-section rods has the largest band gap known of any 2D structure; however, this crystal has very thin walls between adjacent holes (e.g., ~ 15 nm for visible wavelengths) that are difficult to realize at small length scales. Thus, an additional aim of modeling is to identify crystal geometries that best combine large absolute band gaps with manufacturability.

However, a systematic approach towards targeting new structures for study has thus far been lacking. What new structures should be studied? How will we know when the structure with the largest possible band gap has been found? Symmetry, a fundamental property that both links and differentiates crystal structures, provides a framework to help address these questions.

We use a benchmarking technique based on photonic crystal symmetry as a guide to those arrangements that possess large absolute photonic band gaps. Within a class of photonic crystal structures, we seek the optimal "amount" of total structure symmetry that will give rise to the largest absolute band gaps. Different structures may be compared based on their symmetry properties, and those arrangements that lack sufficient symmetry properties can be discarded without further investigation. New structures that fall within the regime of the ideal amount of total structure symmetry can be investigated more closely. The advantage of such an optimal symmetry principle is that it allows researchers to focus on the most promising crystal structures, and may also indicate when the structure with the maximum possible absolute band gap has been found.

Both experimentalists and modeling groups have migrated toward a single class of structures that have been shown to possess large absolute band gaps. These structures belong to the hexagonal lattice family, or Laue symmetry group *6mm*. Here, we present a comparison of the structures within this class from the viewpoint of their symmetry properties. We show how both lattice and point symmetries combine to determine the band properties of the crystal. The differences in band structure are clearly demonstrated by a comparison of the crystal gap maps. These gap maps also form a concise, yet comprehensive, guide to the most utilized 2D PBG structures.

3.2 Symmetry Properties of Laue Group *6mm*

There are five plane groups (i.e., two-dimensional space groups) that compose the hexagonal crystal family: *p3*, *p6*, *p31m*, *p3m1*, and *p6mm*.[17] The first two belong to a class of structures with relatively low symmetry, the Laue group *6*. The last three plane groups form the Laue group *6mm*, and possess a much higher degree of symmetry. The plane groups *p31m* and *p3m1* each have 6 unique symmetry operations, while *p6mm* has 12 symmetry operations, the most of any of the 2D lattices. As high crystal symmetry

plays an important role in opening PBGs, we will investigate 2D photonic crystals that have Laue group symmetry *6mm*. Figure 3-1 illustrates schematically the symmetries present in each of these plane groups. The unit cell is shown as a rhombus, the typical crystallographic unit cell representation for the hexagonal crystal family. The solid symbols mark points of rotational symmetry, with the number of sides *n* representing an *n*-fold rotational point. Solid lines mark mirror lines, and dashed lines indicate glide lines (i.e., reflection, followed by translation). The high degree of symmetry present in the *p6mm* plane group is clearly demonstrated in the figure. The *p6mm* group yields many interesting crystal structures, and will be the focus of much of the discussion in this paper.

The plane group alone is not enough to define the entire crystal symmetry; the point group is also needed to describe the symmetry of the dielectric rods or holes within the two-dimensional crystal structure. For example, consider a single rod placed at the corners of the plane group unit cells shown in Fig. 3-1. If the rod has a circular cross section, then the crystal belongs to plane group *p6mm*. If the rod has a triangular cross section, the crystal might have the symmetry of either plane group *p31m* or *p3m1*, depending on the orientation of the rod with respect to the unit cell axes. Usually, choosing circular rods will tend to move the crystal into a higher symmetry group than for other rod cross-section shapes such as hexagons or triangles. Other properties such as rod diameter or material can also be used to modify the overall crystal symmetry.

Previous studies of rod geometry (shape) on the photonic band gap properties of hexagonal lattice structures have shown that circular cross-section rods tend to produce the largest absolute band gaps and are the preferred shape.[10,18,19] Thus, we will study arrangements of circular cross-section rods with the additional requirement that the rods do not overlap; this will likely not exclude important crystal arrangements, as it is has been shown that existing band gaps rapidly disappear when the connectivity of the structure changes.[20]

3.3 Photonic Band Gaps

The two-dimensional photonic crystals are formed by infinitely long rods whose intersection with a plane forms one of the *6mm* lattices. The rods are composed of a material with dielectric constant ε_a, embedded in a different background dielectric material ε_b. In this study, the crystals are formed using two materials, gallium arsenide ($\varepsilon_{GaAs} = 11.4$ at $\lambda = 1500$ nm) and air ($\varepsilon_{air} = 1.0$). The GaAs can either fill the crystal rods or the background (leaving air occupying the rods, producing holes) yielding two complementary structures for each lattice arrangement.

To obtain the photonic crystal frequency bands, Maxwell's equations for electro-magnetic wave propagation are solved using the plane wave expansion technique described by Ho *et al.*[21] The frequency modes in a two-dimensional crystal separate into two orthogonal polarizations: H-polarized, with the magnetic field vector aligned with the rod axes, and E-polarized, with the electric field vector parallel to the rods. This mode decoupling greatly simplifies the solution of Maxwell's equations. Band calculations for the simple triangular lattice were performed using 469 plane waves, while all other structures were studied using 1261 plane waves. Crystal arrangements other than the triangular structure are more complex and require a larger number of expansion terms to ensure sufficient accuracy (within 1% error).

3.3.1 Triangular Structures

One of the first two-dimensional photonic crystals studied was the simple structure formed by rods arranged on a triangular lattice.[10,11,20,22] A triangular lattice with circular cross-section rods is a natural place to begin the investigations as this structure possesses a high degree of symmetry—an important factor in opening large band gaps. The simple triangular structure is composed of one rod with point symmetry *6mm* in each unit cell, yielding a structure with *p6mm* symmetry. A gap map for air columns in a

background dielectric of $\varepsilon_b = 11.4$ is shown in Fig. 3-2, where nondimensionalized band frequencies are plotted against rod filling fraction. At high filling fractions an H-polarization (H_1) and E-polarization (E_2) gap overlap, producing a large absolute band gap for all possible wave polarizations and direction of propagation. The maximum size of the absolute band gap occurs at a filling fraction $f = 0.823$, and is an impressive $\Delta\omega = 0.0759(2\pi c/a)$ wide. This frequency domain band gap corresponds to a wavelength gap of 235 nm, centered at 1500 nm. This absolute band gap remains the largest of all of the two-dimensional structures studied to date.

The complementary structure of circular cross-section dielectric rods in air does not fare as well. The gap map for the triangular lattice of $\varepsilon_a = 11.4$ rods in air is shown in Fig. 3-3. This arrangement is dominated by large E-polarization gaps that exist across a wide range of filling fractions. One low frequency H-polarization gap (H_1) opens at filling fractions from 0.22 to 0.72, but lies between the two adjacent E-polarization gaps and does not produce an absolute band gap. A higher frequency H-polarization gap exists for a limited range of filling fractions ($f = 0.04$–0.17), but also does not overlap with any of the E-polarization gaps. Only a few H-polarization streaks open within existing E-polarization gaps, producing small absolute gaps at nondimensionalized frequencies of approximately $0.8(2\pi c/a)$. These tiny gaps appear to be of limited experimental utility.

The dramatic differences between the two complementary triangular structures has been qualitatively explained by examining the character of the individual polarizations.[20] H-polarization gaps are largest when the high dielectric constant material is arranged in a well connected lattice network, while E-polarization gaps prefer isolated regions of high dielectric material. Both polarization gaps appear in the triangular lattice of air columns when the rods are nearly close-packed; under these conditions, a network of thin high-ε "veins" connect "spots" of dielectric material, simultaneously satisfying the requirements of both wave polarizations.

In addition to the material and filling fraction requirements, it is equally important for the structure to possess the correct amount of symmetry to open absolute band gaps. Indeed, if large absolute band gaps were dependent only on the lattice geometry, then the triangular lattice of holes in dielectric should possess a large absolute band gap for other rod cross-sectional shapes, such as squares or rectangles. As this is not the case,[18,19] we must conclude that rod (scattering element) symmetry is an important factor. Conversely, since a square lattice of circular cross-section holes in dielectric has a much smaller absolute band gap than the corresponding triangular case,[12] the lattice symmetry must play a significant role in dictating the frequency band properties. Therefore, it appears that the combination of high lattice and element symmetry is critical in the formation of band gaps.

The large absolute band gap of the triangular lattice does not necessarily provide the optimal structure choice for use in all experiments or devices, due to very thin dielectric walls present between adjacent air holes at the maximum gap condition. For a midgap wavelength of 1500 nm and the maximum gap filling fraction of 0.823, the dielectric walls are as thin as 35 nm. To improve manufacturability at small length scales, the filling fraction must be reduced below that for the maximum gap condition.

3.3.2 Honeycomb Structures

In an effort to overcome the fabrication difficulties associated with the triangular lattice structure, attention has turned towards other arrangements. Many different crystal structures within the *p6mm* class can be obtained by changing the symmetry of the rods that compose the crystal. If the single *6mm* rod of the triangular lattice is replaced with two rods, each with *3m.* symmetry, the honeycomb (or graphite) structure is obtained.[15,20] Like the triangular photonic crystal, the honeycomb lattice also possesses a high degree of symmetry. The primitive unit cell, however, must now contain two rods instead of one. Though the overall symmetry class of the structure has not changed, the element

symmetry of the rods has been reduced and thus the overall symmetry of the honeycomb structure is slightly lower than that of the triangular structure. In 2D photonic crystals it has been shown that reducing the symmetry of a structure can cause larger band gaps to open.[12,14] This principle has been shown to improve the band gaps in some 3D photonic crystals as well.[21]

First, we examine the honeycomb lattice of air columns in a background dielectric. The gap map for this structure is shown in Fig. 3-4. One absolute band gap appears for this structure, having a maximum magnitude of $\Delta\omega = 0.0285(2\pi c/a)$ at a rod filling fraction of 0.57. This gap does not surpass the size of the absolute gap present in the triangular structure; it appears that reduction of rod symmetry has not helped in this situation. Analyses of many crystal arrangements with the low dielectric constant material in the rods have shown that large gaps occur at high rod filling fractions. For the honeycomb structure, the maximum filling fraction before the rods begin to touch $(f \approx 0.605)$ is not large enough to form substantial gaps. Symmetry reduction is not enough to overcome the fundamental material dependence of the photonic gaps.

For the complementary arrangement of high dielectric constant rods in air, the situation is reversed and large gaps tend to open at smaller filling fractions. Thus, we would expect that symmetry reduction could play a favorable role in opening large band gaps for this honeycomb structure. Indeed, we see in the gap map of Fig. 3-5 that several large H-polarization gaps have opened up, producing four substantial absolute band gaps. The largest absolute gap for the honeycomb lattice occurs at a filling fraction $f = 0.14$, and is $0.0881(2\pi c/a)$ wide. Though this band gap is not quite as large as the maximum for the air-in-dielectric triangular lattice, this structure may be much easier to microfabricate as no thin walls or tiny features are present; for a midgap wavelength of 1500 nm, the rod diameters will be 202 nm at the maximum gap condition. The existence of multiple band gaps in this structure may also provide opportunities for novel applications.

3.3.3 Reduced Symmetry Triangular Structures

A new crystal structure may be obtained by combining the two different rod symmetry types of the triangular and honeycomb structures. That is, we include both *6mm* and *3m.* rods in the same unit cell. If all of the rods are identical, then the crystal reverts back to the simple triangular structure. However, if the rods of each symmetry type differ from each other (e.g., different diameters), a new "reduced symmetry triangular" structure is obtained.[12] This structure has also been termed the face-centered graphite lattice.[23]

Following the nomenclature in Ref. 12, the ratio of the rod diameters is defined as $\beta = d_2/d_1$, where the index 1 refers to the *3m.* symmetry rods, and index 2 refers to the *6mm* rod. The honeycomb lattice is recovered when $\beta = 0$, and the triangular lattice when $\beta = 1$ or ∞. The parameter β and the filling fraction f can be varied in an effort to maximize the absolute PBG. In Fig. 3-6, the effect of changing the rod diameter ratio β is shown for a structure of dielectric rods in air for constant filling fraction $f = 0.14$ (the maximum gap condition for the honeycomb structure). The absolute gap of the honeycomb structure is increased through the addition of a small *6mm* symmetry rod into the unit cell, reaching a maximum width when $\beta = 0.11$. Here, the size of the absolute gap is $0.0967(2\pi c/a)$, an increase of 9.9% over the honeycomb structure gap. However, the increased gap size has been obtained at the cost of manufacturability; for a midgap wavelength of 1500 nm, the minimum feature size has dropped from approximately 200 nm in the honeycomb lattice to a mere 24 nm. Though the reduced symmetry triangular structure has not passed the test of fabricational ease, it sheds light on the effectiveness of symmetry breaking. For crystals composed of dielectric rods in air, we have seen that no absolute gap occurs for the triangular structure (all *6mm* symmetry rods). A large absolute band gap opens up for the honeycomb lattice (*3m.* symmetry rods) that can be increased even further by combining the two rod types in one crystal structure. Thus, it appears that the ideal "amount" of symmetry lies somewhere between that of the

triangular and honeycomb structures. Based on this brief analysis, we might predict that structures composed of lower symmetry elements than that for the honeycomb lattice will have correspondingly smaller absolute band gaps.

Now we consider the complementary structure, that of air holes in a dielectric background. We have already seen that a large gap exists for the triangular lattice, and that the gap is decreased for the honeycomb structure. Combining the two rod symmetry types will produce one of two possible outcomes: (1) The gap will be larger than for the triangular lattice, suggesting that this is the optimal condition to yield the maximum absolute gap, or (2) the absolute gaps formed by the two rod types will all be smaller than that for the *6mm* rods alone, implying that the triangular lattice forms the optimal structure. Fig. 3-7 illustrates that the latter prediction is correct. In this gap map, the non-dimensionalized frequencies are plotted versus rod diameter ratio for a constant filling fraction of 0.57. The absolute gap for the honeycomb structure is present at $\beta = 0$ and becomes steadily smaller as β decreases. Two new absolute gaps open at intermediate values of β, at nondimensionalized frequencies of $0.88(2\pi c/a)$ and $0.55(2\pi c/a)$. However, none of these absolute gaps are larger than the maximum gap found for the triangular structure of holes. The introduction of *3m.* rods into the triangular structure only serves to decrease the size of the absolute band gap.

The results obtained thus far are summarized in terms of the crystal symmetry. For structures with the high dielectric constant material contained in the rods, the maximum absolute gap occurs when symmetry elements *6mm* and *3m.* are both present. For a photonic crystal of air columns in a high dielectric background, the maximum absolute gap is found using only *6mm* symmetry elements. This suggests that the optimal element symmetry present within the *p6mm* plane group has been determined; introduction of elements with lower symmetry into the unit cell should only decrease the size of the absolute gaps.

3.3.4 Other p6mm Structures

Further reduction of the element symmetry can produce other *p6mm* lattices. Consider, for example, the structure produced by placing three identical circular cross-section rods in the unit cell such that they have *2mm* element symmetry. This new arrangement is called the "rotated honeycomb" structure, as the resulting crystal appears as though the hexagonal cells of the honeycomb lattice have been twisted with respect to one another. Following the guideline for the correspondence of absolute gaps and lattice symmetry, the element symmetry in the rotated honeycomb structure is expected to be too low to produce large absolute PBGs. Figure 3-8 shows that this is indeed the case. The gap map for a structure of dielectric rods in air is shown for a range of filling fractions. The structure mostly possesses E-polarization gaps at small filling fractions, though two thin H-polarization gaps also exist. One gap (H_1) overlaps very slightly with the lowest E-polarization gap (E_3) at a filling fraction $f \approx 0.4$.

To try to improve this tiny absolute gap, we can combine the *2mm* symmetry elements with a higher symmetry element, as was done for the reduced symmetry triangular lattice case. If a *6mm* symmetry rod is added to the unit cell we obtain a new structure, termed the rotated double-rod structure. Here, an additional parameter (β, the *6mm* to *2mm* rod diameter ratio) is available to help improve the maximum gap obtained for the honeycomb lattice of rods in air. The triangular structure is recovered when $\beta = 1$. No improvements in absolute gap size are found as β is varied, as is illustrated in the gap map of Fig. 3-9. The maximum absolute gap was that found for the rotated honeycomb case ($\beta = 0$) at a filling fraction of 0.42. This small absolute gap does not offer any advantages over those structures previously investigated. However, these results do agree with the analysis of the optimal amount of structural symmetry. Though at first glance it may appear that the rotated honeycomb structure is very similar to the honeycomb structure (compare insets of Figs. 3-5 and 3-8), they display a marked difference in frequency band properties.

3.3.5 Boron Nitride Structures

We have exhausted all of the promising crystal structures within the *p6mm* plane group, and have developed a hierarchy of element symmetries to produce the optimal absolute photonic band gaps. However, we still do not know how the photonic gaps of a crystal outside the *p6mm* plane group will compare. It is possible that the unique combination of element symmetry and the symmetry of the plane group will combine to produce a structure with a larger absolute band gap than was found for the *p6mm* structures.

If the two identical *3m.* symmetry elements in the hexagonal structure are replaced with two different *3m.* symmetry elements (for example, with two rods of different diameters), then a new structure is obtained that has the symmetry of the plane group *p3m1*. This structure has been termed the boron nitride structure because of the analogy to the atomic crystal structure of that compound.[13] The *p3m1* plane group has lower symmetry than the *p6mm* group, as there are only 6 unique symmetry operations as compared with the 12 symmetry operations present in the latter case. Still, this structure is quite similar to the honeycomb structure, and might offer an improvement upon the largest gap structure found there.

Figure 3-10 shows the gap map for the boron nitride structure of air cylinders in a dielectric background material at a rod filling fraction of 0.57. The triangular lattice is obtained when one of the rods is removed ($\beta = 0$); the honeycomb structure is produced when the rods are of equal diameter ($\beta = 1$). A few small absolute band gaps form for this structure, but none surpasses the large band gap present in the triangular structure of air columns in dielectric. This result is also true at higher rod filling fractions. These observations are in agreement with the optimal symmetry guidelines, as we have already surmised that the triangular structure will give the largest band gap for a crystal of air columns in dielectric.

The opposite configuration of dielectric cylinders in air is shown in the gap map of Fig. 3-11 for a filling fraction of 0.14. The maximum band gap occurs at $\beta = 1$, the honeycomb lattice condition. Another respectable absolute band gap also forms at intermediate values of β, reaching a maximum width of $0.0743(2\pi c/a)$ at $\beta = 0.34$, slightly smaller than the size of the honeycomb structure gap. After searching a range of filling fractions for the boron nitride structure, we found that the case when the rods are of equal diameter (the honeycomb structure) produces the largest absolute band gap.

3.4 Discussion

The band gap results for many specific crystal structures within the *6mm* Laue group have been presented. Most of the crystals belong to the *p6mm* symmetry group, the two-dimensional plane group with the highest symmetry. We have also studied one structure within the *p3m1* symmetry group, the boron nitride structure. Notably absent from the discussion so far have been crystal structures with the symmetry of group *p31m*. However, using circular cross-section rods tends to increase the overall crystal symmetry of *p31m* structures to that of either *p3m1* or *p6mm*. A true *p31m* symmetry crystal would require the use of lower symmetry rods (e.g., triangular or rectangular cross-section) which are expected to yield smaller band gaps, based on previous studies.[18,19]

A summary of important properties of the crystal structures formed by air rods in a high dielectric background is shown in Table 3-1. The large absolute band gap width of the triangular structure is clear from a comparison of the gap size in wavelength units. If the band gap is chosen to be centered at 1500 nm, the triangular structure gap would be 234 nm, over three times the size of the honeycomb lattice absolute band gap. Clearly, the high symmetry of the triangular lattice is the optimal arrangement for crystals of holes in dielectric.

Table 3-2 summarizes the results for two-dimensional crystals of dielectric rods in air. Here, a much different picture is obtained as the structure symmetry is decreased. The triangular lattice here does not possess any sizable band gaps. However, significant benefits are obtained by decreasing the rod symmetry: Large absolute band gaps are present in both the honeycomb and reduced symmetry triangular structures, both of which contain rods with *3m.* symmetry. The largest band gap found for crystals of dielectric rods in air is for the reduced symmetry triangular structure, with a bandgap width of 151 nm centered at 1500 nm. However, this structure may not be optimal for device microfabrication because of the presence of small diameter rods within the crystal. The smallest rods are 24 nm in diameter at 1500 nm midgap. To overcome the problems associated with creating these small features, the honeycomb structure may be a better suited design choice. The band gap (137 nm) is smaller than that for the reduced symmetry triangular structure, but the minimum feature size is nearly an order of magnitude larger, at 202 nm. Sacrificing a small amount of band width may be worth the great gain in fabricational ease. As the symmetry of the rods is decreased even further, the absolute gap sizes drop off quickly. Thus, for crystals composed of dielectric rods in air, it appears that the optimal amount of crystal symmetry is that of the maximally symmetric plane group (*p6mm*) containing elements that are slightly less symmetric (the *3m.* rods).

Why is it that swapping the placement of dielectric material within the crystal structure changes the symmetry required to produce the maximum absolute band gaps? The answer is not straightforward, but lies in the complex interplay of the fields and the dielectric materials. The electromagnetic frequency modes prefer to concentrate their energy in regions of high dielectric constant in order to lower the mode frequency.[20] The energy distribution can be quantitatively stated in terms of the energy density, u, by the relation

$$u = \frac{1}{2}(\mathbf{E} \cdot \mathbf{D} + \mathbf{B} \cdot \mathbf{H}) = \varepsilon E^2. \qquad (3.1)$$

Waves with orthogonal polarizations will behave differently in structures that have isolated high-ε regions versus those with connected high-ε material due to the dissimilar electromagnetic field concentrations. It may also be expected that the mode degeneracies in the two complementary crystal structures will also be different. In the case of air holes in dielectric, the band gaps in the triangular structure are not limited by band degeneracies. Lowering the symmetry in this case cannot improve the band properties, and only serves to decrease the gap size due to a lowering of the total rod filling fraction. However, for dielectric rods in air, the H-polarization gaps are restricted because of band degeneracies at high lattice symmetry points. Crystal symmetry reduction lifts these band degeneracies, greatly increasing the magnitude of the H-polarization gaps and creating large absolute band gaps where none existed for the triangular structure. Both material filling fraction and crystal symmetry must be optimized to produce these large absolute PBGs.

It is already known that high rod filling fractions are favored in crystals comprised of air holes, while dielectric rod arrangements prefer smaller filling fractions. In addition, we have determined the optimal amount of symmetry through a comparison of structures that fall within the hexagonal group of two-dimensional crystals. This approach offers a guide towards new crystal arrangements, and may suggest when the crystal structure with the largest absolute band gaps has been found. Analysis of crystal symmetry provides a general set of rules for exploring new geometries that should be applicable to 3D photonic crystals as well.

3.5 Conclusions

Using a symmetry analysis approach, we have investigated a variety of hexagonal two-dimensional photonic crystal structures. This methodical approach allows one to delineate the relationship between rod and crystal symmetries and the resulting photonic band structure. Symmetry analysis has been used to identify the crystal geometries that yield large band gaps for the two complementary dielectric configurations (air columns in dielectric, and dielectric rods in air).

For crystals that are comprised of air columns within a dielectric background material $\varepsilon_b = 11.4$, the maximum photonic band gap is found for the triangular lattice structure of circular cross-section rods with filling fraction $f = 0.823$. The magnitude of the absolute photonic band gap for this structure is $\Delta\omega = 0.0759(2\pi c/a)$, and is the largest band gap (in wavelength) found in any of the two-dimensional photonic structures. However, the thin walls present within the crystal render microfabrication difficult, and thus the complementary crystal arrangement (dielectric rods in air) may be preferred. For dielectric constant $\varepsilon_a = 11.4$ rods in air, the optimal structure was found to have a blend of *6mm* and *3m.* symmetry elements. This reduced symmetry triangular structure has a maximum absolute photonic band gap of $\Delta\omega = 0.0967(2\pi c/a)$ at a rod filling fraction $f = 0.14$ and a rod diameter ratio $\beta = 0.11$. As was the case for the triangular lattice, the small features within this crystal structure (in this case, small diameter rods) may again lead to problems in fabrication. It may be advantageous to sacrifice some of the photonic gap width in exchange for manufacturing robustness by reverting to the honeycomb structure. Though the gap size is 9% smaller than that for the reduced-symmetry triangular lattice, the smallest feature size is 8.5 times larger, making this structure easier to fabricate.

3.6 References

[1] E. Yablonovitch, "Inhibited Spontaneous Emission in Solid-State Physics and Electronics," *Phys. Rev. Lett.* **58**, 2059 (1987).

[2] S. John, "Strong Localization of Photons in Certain Disordered Dielectric Superlattices," *Phys. Rev. Lett.* **58**, 2486 (1987).

[3] J. R. Wendt, G. A. Vawter, P. L. Gourley, T. M. Brennan, and B. E. Hammons, "Nanofabrication of Photonic Lattice Structures in GaAs/AlGaAs," *J. Vac. Sci. Technol. B* **11**, 2637 (1993).

[4] K. Inoue, M. Wada, K. Sakoda, A. Yamanaka, M. Hayashi, and J. W. Haus, "Fabrication of Two-Dimensional Photonic Band Structure with Near-Infrared Band Gap," *Jpn. J. Appl. Phys.* **33**, L1463 (1994).

[5] U. Grüning, V. Lehmann, S. Ottow, and K. Busch, "Macroporous Silicon with a Complete Two-Dimensional Photonic Band Gap Centered at 5 μm," *Appl. Phys. Lett.* **68**, 747 (1996).

[6] T. F. Krauss, R. M. De La Rue, and S. Brand, "Two-Dimensional Photonic-Bandgap Structures Operating at Near-Infrared Wavelengths," *Nature* **383**, 699 (1996).

[7] C. C. Cheng and A. Scherer, "Fabrication of Photonic Band-Gap Crystals," *J. Vac. Sci. Tech. B* **13**, 2696 (1995).

[8] V. N. Bogomolov, S. V. Gaponenko, A. M. Kapitonov, A. V. Prokofiev, A. N. Ponyavina, N. I. Silvanovich, and S. M. Samoilovich, "Photonic Band Gap in the Visible Range in a Three-Dimensional Solid State Lattice," *Appl. Phys. A* **63**, 613 (1996).

[9] C. C. Cheng, A. Scherer, V. Arbet-Engels, and E. Yablonovitch, "Lithographic Band Gap Tuning in Photonic Band Gap Crystals," *J. Vac. Sci. Tech. B* **14**, 4110 (1996).

[10] P. R. Villeneuve and M. Piché, "Photonic Band Gaps in Two-Dimensional Square and Hexagonal Lattices," *Phys. Rev. B* **46**, 4969 (1992).

[11] R. D. Meade, K. D. Brommer, A. M. Rappe, and J. D. Joannopoulos, "Existence of a Photonic Band Gap in Two Dimensions," *Appl. Phys. Lett.* **61**, 495 (1992).

[12] C. M. Anderson and K. P. Giapis, "Larger Two-Dimensional Photonic Band Gaps," *Phys. Rev. Lett.* **77**, 2949 (1996).

[13] D. Cassagne, C. Jouanin, and D. Bertho, "Photonic Band Gaps in a Two-Dimensional Graphite Structure," *Phys. Rev. B* **52**, R2217 (1995).

[14] C. M. Anderson and K. P. Giapis, "Symmetry Reduction in Group *4mm* Photonic Crystals," *Phys. Rev. B* **56**, 7313 (1997).

[15] D. Cassagne, C. Jouanin, and D. Bertho, "Hexagonal Photonic-Band-Gap Structures," *Phys. Rev. B* **53**, 7134 (1996).

[16] C.-S. Kee, J.-E. Kim, and H. Y. Park, "Absolute Photonic Band Gap in a Two-Dimensional Square Lattice of Square Dielectric Rods in Air," *Phys. Rev. E* **56**, R6291 (1997).

[17] *International Tables for Crystallography*, edited by T. Hahn, D. Reidel Publishing Company, Boston (1987).

[18] T. Baba and T. Matsuzaki, "Theoretical Calculation of Photonic Gap in Semiconductor 2-Dimensional Photonic Crystals with Various Shapes of Optical Atoms," *Jpn. J. Appl. Phys.* **34**, 4496 (1995).

[19] R. Padjen, J. M. Gerard, and J. Y. Marzin, "Analysis of the Filling Pattern Dependence of the Photonic Bandgap for Two-Dimensional Systems," *J. Mod. Opt.* **41**, 295 (1994).

[20] J. D. Joannopoulos, R. D. Meade, and J. N. Winn, *Photonic Crystals* (Princeton University Press, Princeton, 1995).

[21] K. M. Ho, C. T. Chan, and C. M. Soukoulis, "Existence of a Photonic Gap in Periodic Dielectric Structures," *Phys. Rev. Lett.* **65**, 3152 (1990).

[22] M. Plihal and A. A. Maradudin, "Photonic Band Structure of Two-Dimensional Systems: The Triangular Lattice," *Phys. Rev. B* **44**, 8565 (1991).

[23] Y. Chen, "Photonic Band Gaps of Two-Dimensional Photonic Lattices: The Face-Centered Graphite Structures," *Superlattices and Microstructures* **22**, 115 (1997).
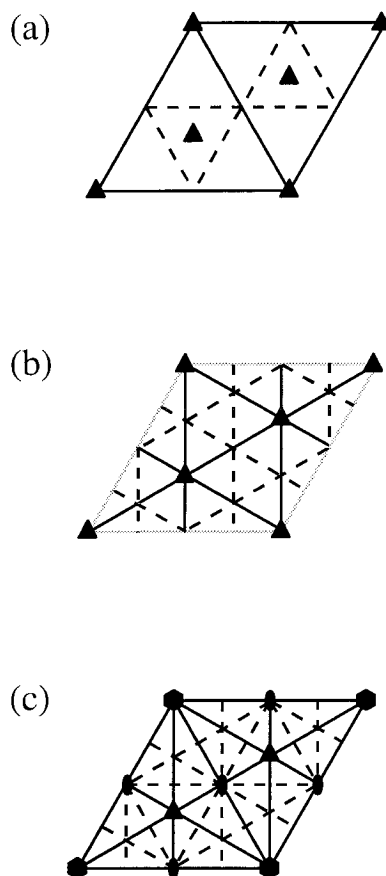
Fig. 3-1. Symmetry properties of the Laue group *6mm* plane groups (a) *p31m*, (b) *p3m1*, and (c) *p6mm*. All mirror lines (solid) and glide lines (dashed) are shown inside the lattice unit cell. Points of rotational symmetry (twofold, threefold, sixfold) are indicated by the filled symbols (ovals, triangles, hexagons, respectively).
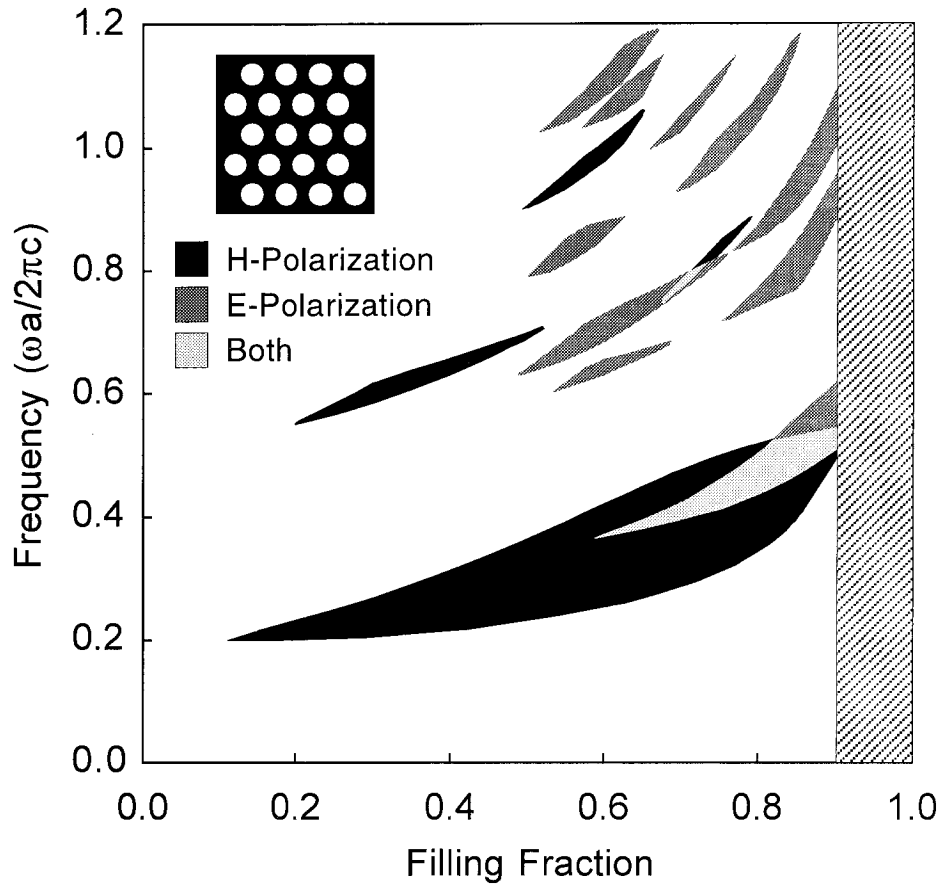
Fig. 3-2. Gap map for the triangular structure of air holes in a background dielectric ($\varepsilon_b = 11.4$). A large absolute band gap occurs where the lowest H-polarization and E-polarization gaps overlap. The maximum gap occurs at $f = 0.823$ and has a magnitude $\Delta\omega = 0.0759(2\pi c/a)$, the largest absolute band gap of any two-dimensional photonic crystal. The hatched region represents filling fractions where the rods overlap.
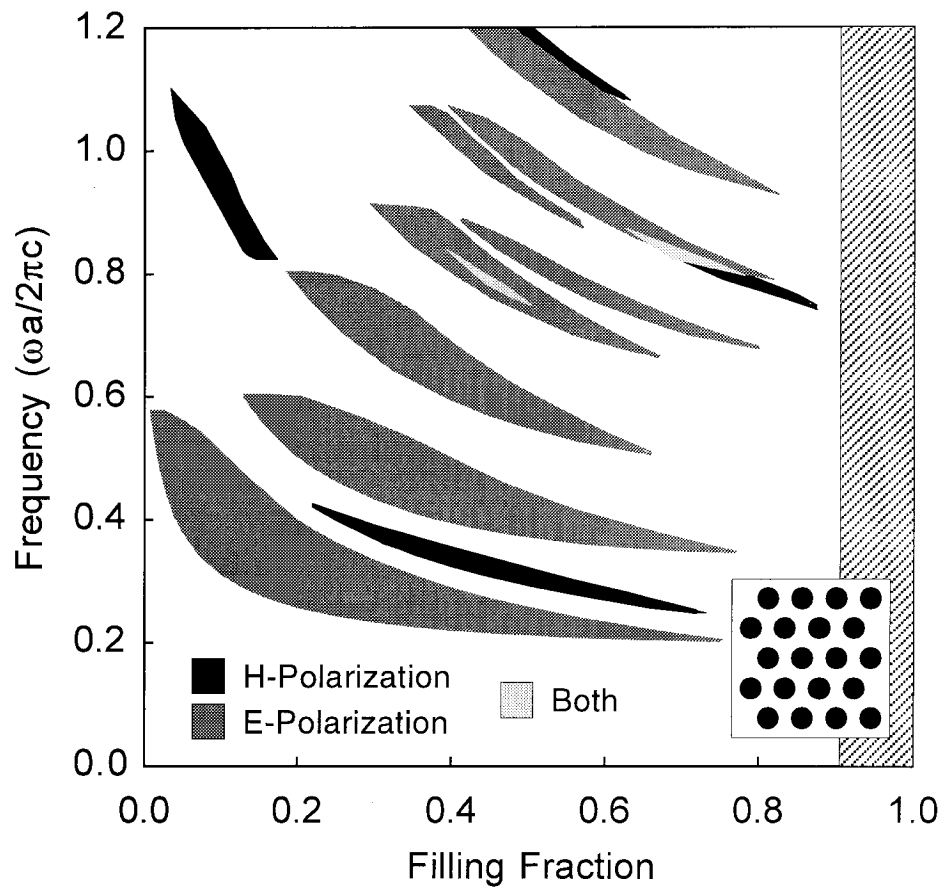
Fig. 3-3. Gap map for the triangular structure of dielectric rods ($\varepsilon_a = 11.4$) in air. Though several wide E-polarization gaps exist, the H-polarization gaps are limited in size and do not overlap with the E-polarization gaps to produce an absolute gap.
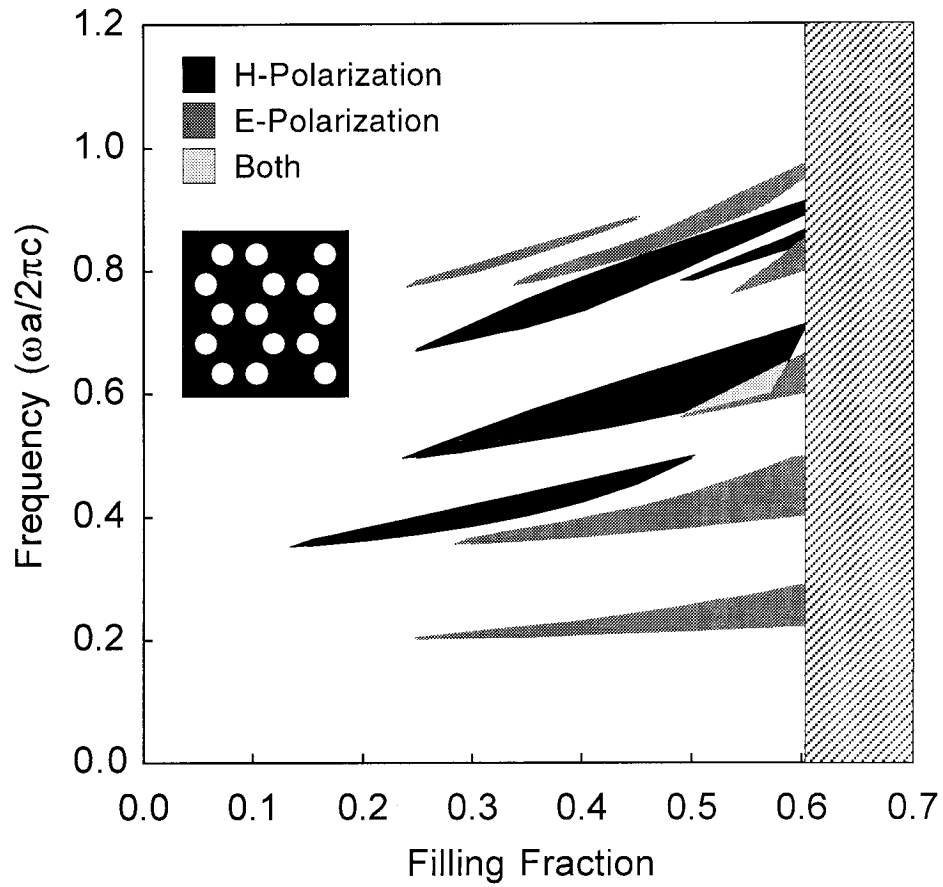
Fig. 3-4. Gap map for the honeycomb structure of air holes in a background dielectric, showing a small absolute band gap formed by the overlap of the H_5 and E_6 bands. The maximum gap width is $\Delta\omega = 0.0285(2\pi c/a)$ at $f = 0.57$, much smaller than for the triangular structure. The reduced rod symmetry has resulted in a smaller band gap.
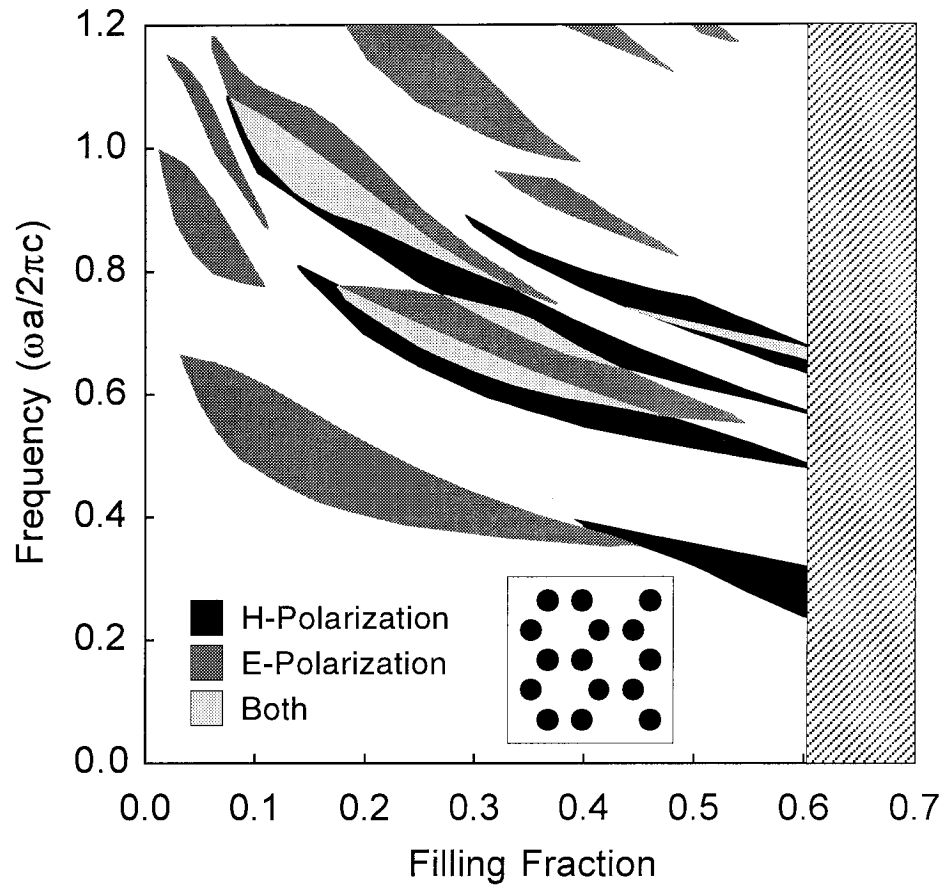
Fig. 3-5. Gap map for the honeycomb structure of dielectric rods in air. The reduced rod symmetry has opened several large H-polarization gaps to produce four absolute band gaps. The largest occurs at $f = 0.14$ and has a magnitude of $\Delta\omega = 0.0881(2\pi c/a)$.
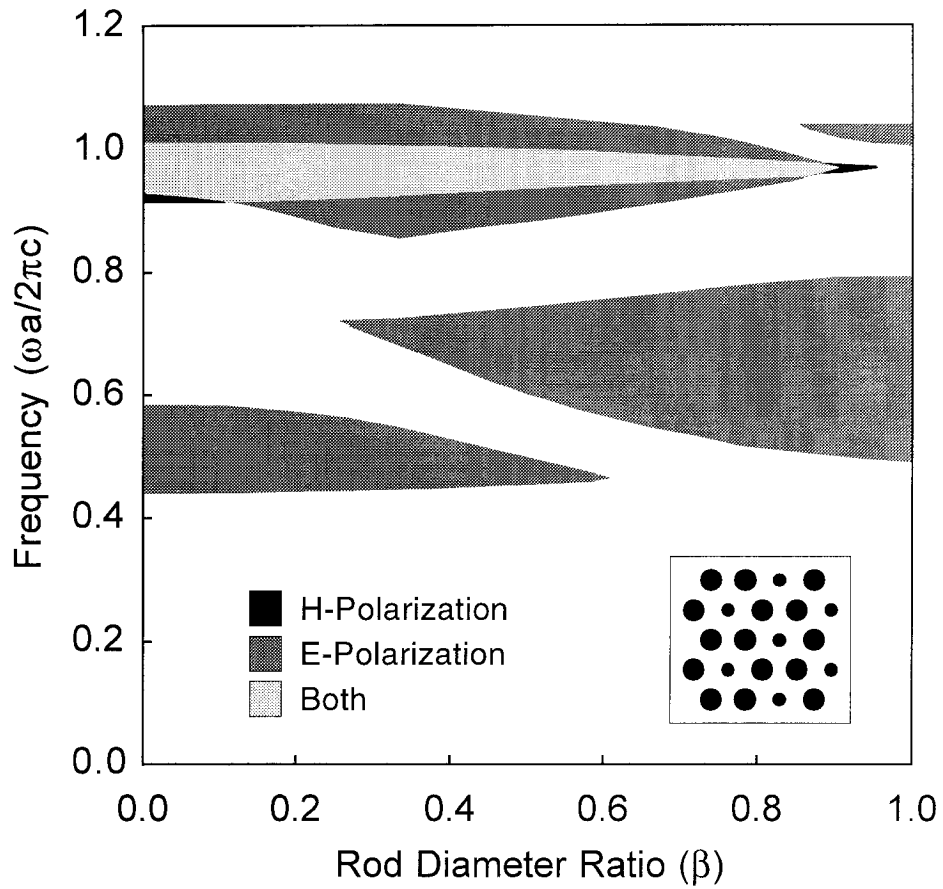
Fig. 3-6. Gap map for the reduced-symmetry triangular structure ($f = 0.14$) of dielectric rods in air, as a function of β. The large absolute gap of the honeycomb structure (shown at $\beta = 0$) is increased further by including higher symmetry (*6mm*) rods in the unit cell. The maximum absolute gap occurs at $\beta = 0.11$.
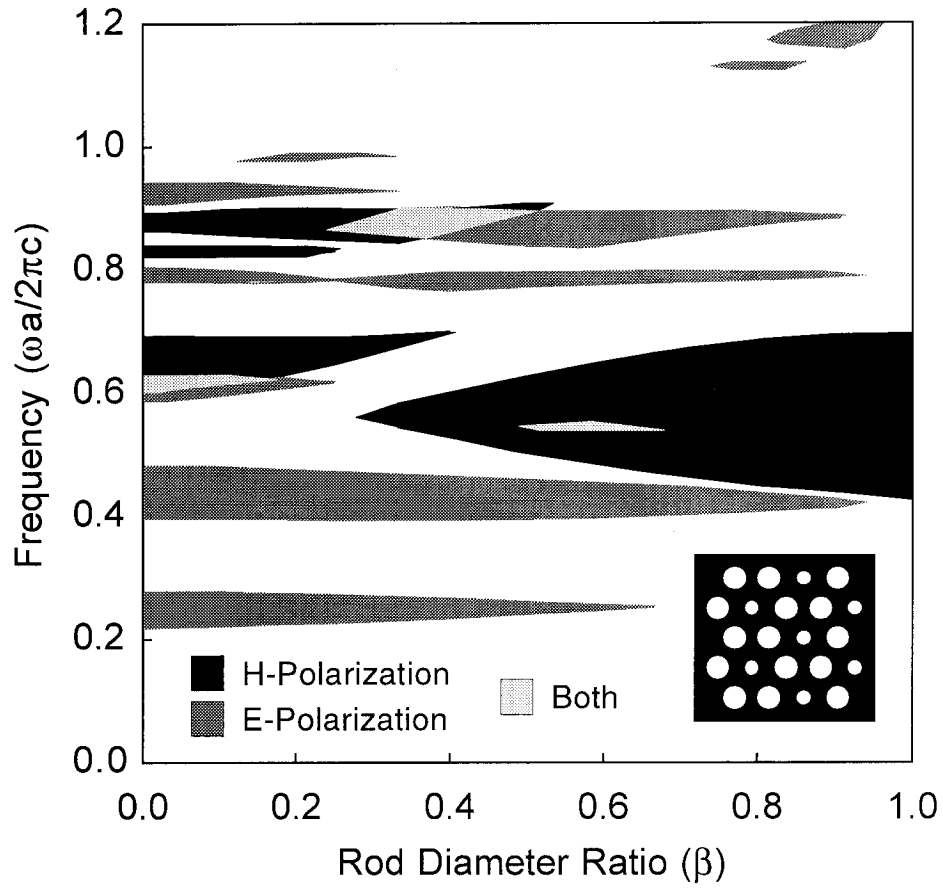
Fig. 3-7. The gap map for the reduced-symmetry triangular structure of air holes at $f = 0.57$ possesses three absolute band gaps through a range of β values. However, none of these gaps are larger than that of the triangular structure.
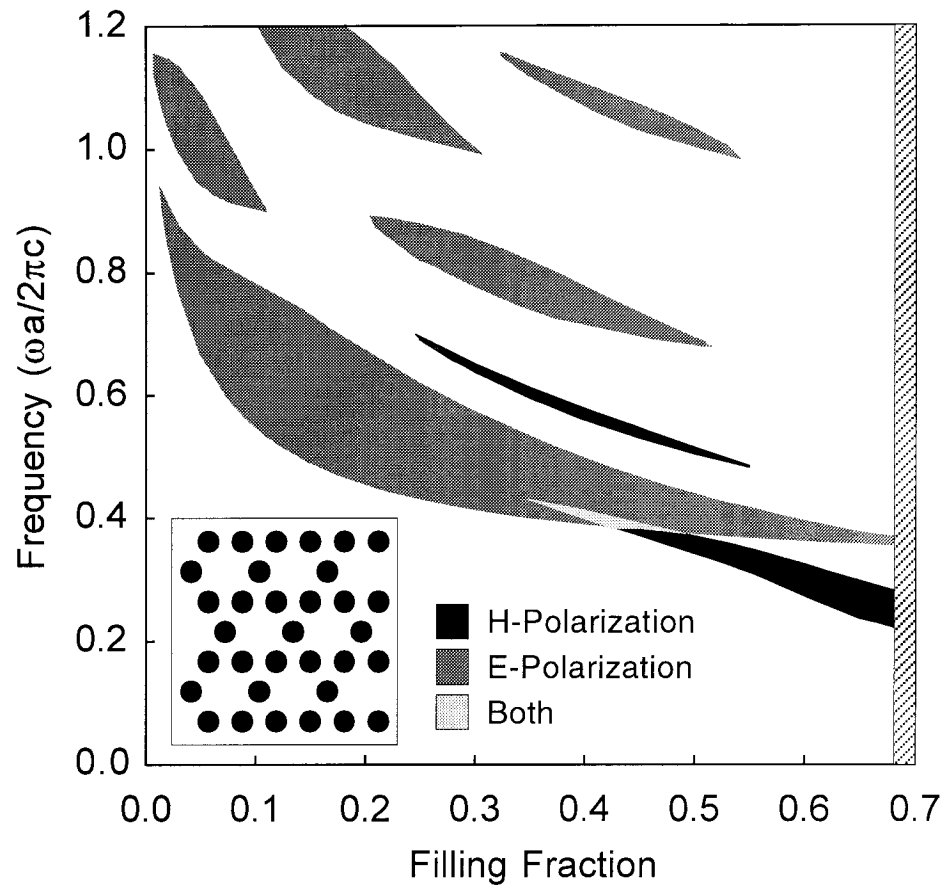
Fig. 3-8. Gap map for the rotated-honeycomb structure of dielectric rods in air. Two H-polarization gaps exist, but minimal overlap occurs between the H_1 and E_3 gaps. The rods composing this structure have low symmetry ($2mm$), greatly reducing the size of the band gaps. Compare this gap map with that in Fig. 3-5.
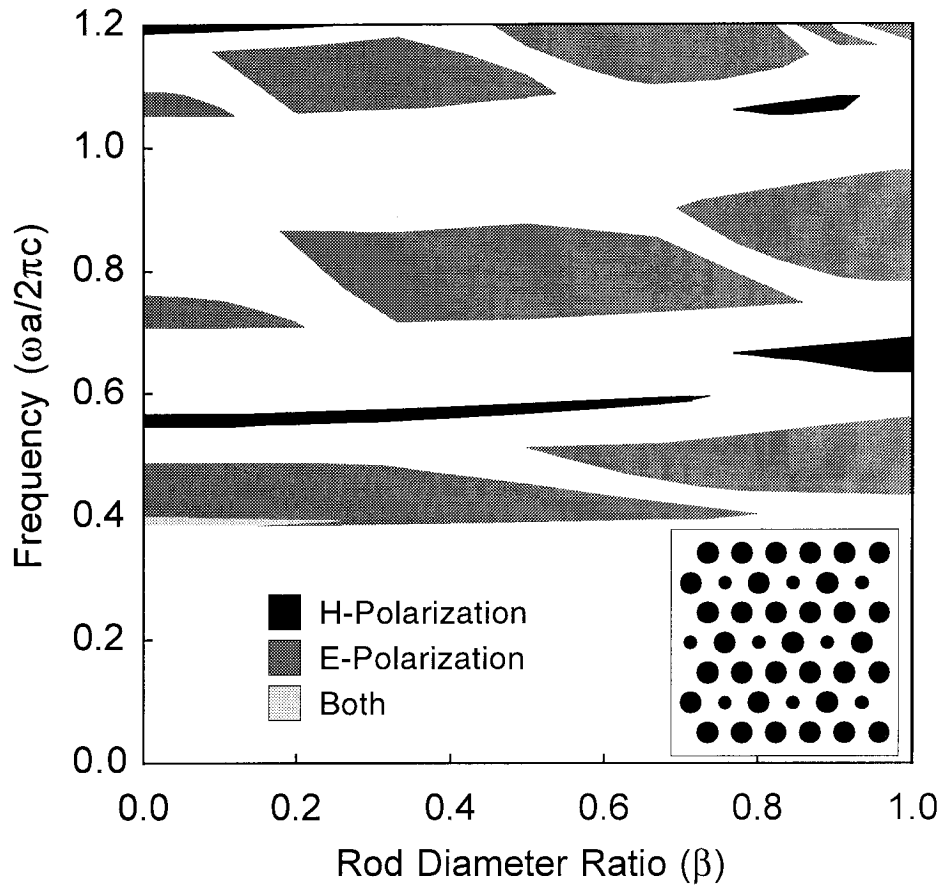
Fig. 3-9. Gap map for the rotated double-rod structure ($f = 0.42$) versus β, the ratio of the *2mm* to *6mm* rod diameters. The introduction of a higher symmetry (*6mm*) rod into the unit cell is not effective in yielding larger gaps. The triangular structure is recovered at $\beta = 1$.
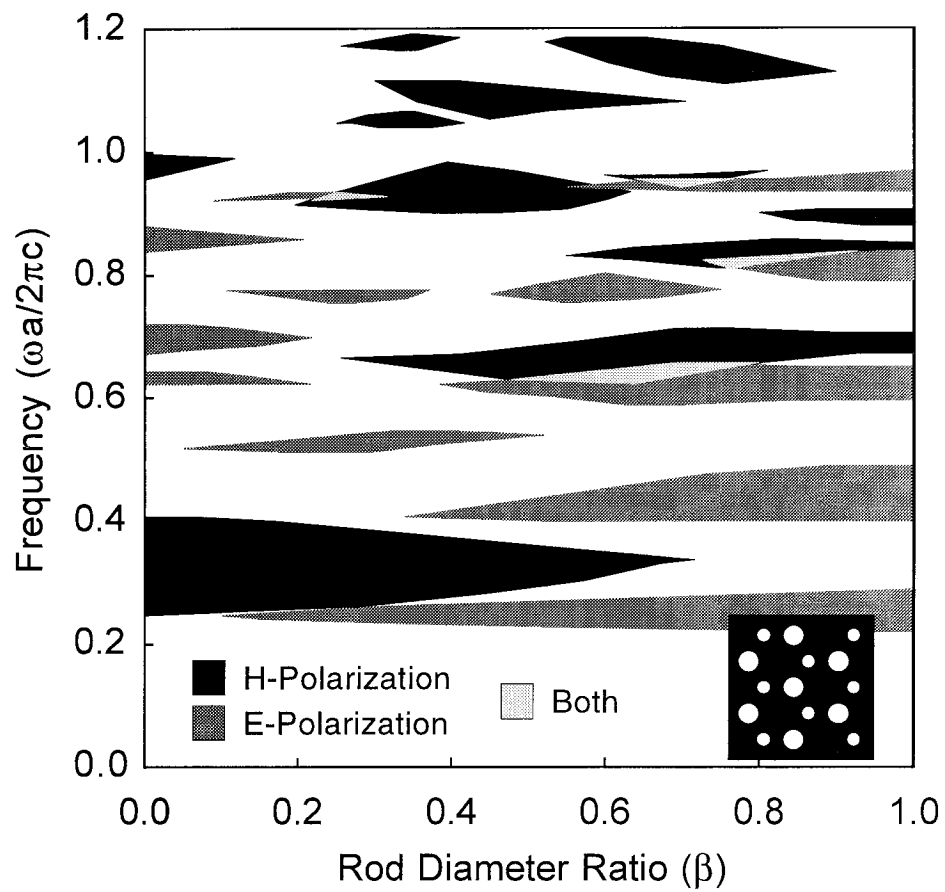
Fig. 3-10. Gap map for the boron nitride structure of air holes in dielectric for $f = 0.57$. Though H-polarization and E-polarization gaps exist and overlap to produce absolute band gaps, they do not exceed the maximum absolute gap of the triangular structure.
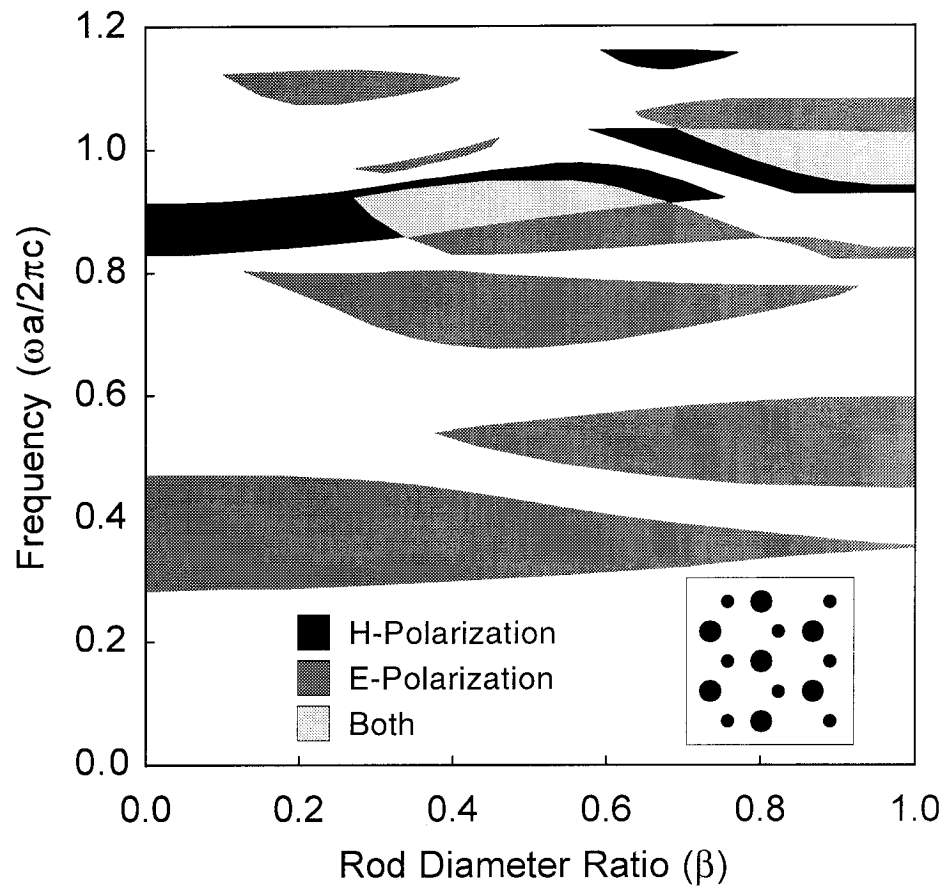
Fig. 3-11. Gap map for the boron nitride structure of dielectric rods in air for the maximum gap case of $f = 0.14$. An absolute gap occurs from the overlap of H_4 and E_5 at intermediate values of the rod diameter ratio β. The absolute gap at $\beta = 1$ corresponds to that of the honeycomb structure, and is the largest gap found for the boron nitride structure as well.
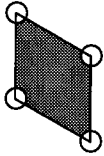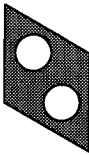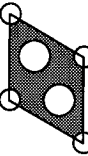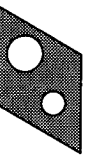
76

Unit Cell	Structure Name	Plane Group	Element Symmetry	Maximum Absolute Gap Conditions	Absolute Gap Size $(2\pi c/a)$	Midgap Frequency $(2\pi c/a)$	Absolute Gap Size (nm) at 1500 nm	Minimum Feature Size (nm)
	Triangular	p6mm	1 rod – 6mm	$f = 0.823$	0.0759	0.487	234	34.6
	Honeycomb (Graphite)	p6mm	2 rods – 3m.	$f = 0.57$	0.0285	0.617	69.3	15.5
	Reduced Symmetry Triangular (Face Centered Graphite)	p6mm	1 rod – 6mm 2 rods – 3m.	Triangular $(\beta = 1)$	—	—	—	—
	Boron Nitride	p3m1	1 rod – 3m. 1 rod – 3m.	Triangular $(\beta = 0)$	—	—	—	—
	Rotated Honeycomb	p6mm	3 rods – 2mm	$f = 0.68$	0.0429	0.972	66.2	≈ 0.1 (cylinders just touching)
	Rotated Double-Rod	p6mm	1 rod – 6mm 3 rods – 2mm	Triangular $(\beta = 1)$	—	—	—	—

Table 3-1. Comparison of band gap data for several group 6mm crystal structures formed of air holes in dielectric ($\varepsilon_b = 11.4$).
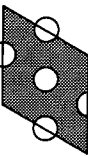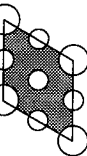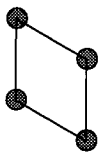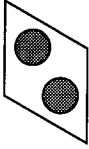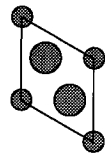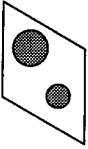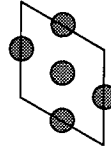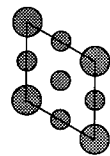
Unit Cell	Structure Name	Plane Group	Element Symmetry	Maximum Absolute Gap Conditions	Absolute Gap Size $(2\pi c/a)$	Midgap Frequency $(2\pi c/a)$	Absolute Gap Size (nm) at 1500 nm	Minimum Feature Size (nm)
	Triangular	*p6mm*	1 rod – *6mm*	*f*=0.45	0.0132	0.789	25.1	834
	Honeycomb (Graphite)	*p6mm*	2 rods – *3m.*	*f*=0.14	0.0881	0.970	136	202
	Reduced Symmetry Triangular (Face Centered Graphite)	*p6mm*	1 rod – *6mm* 2 rods – *3m.*	*f*=0.14, *β*=0.11	0.0967	0.964	151	23.7
	Boron Nitride	*p3m1*	1 rod – *3m.* 1 rod – *3m.*	Honeycomb (*β*=1)	—	—	—	—
	Rotated Honeycomb	*p6mm*	3 rods – *2mm*	*f*=0.42	0.0114	0.394	43.4	232
	Rotated Double-Rod	*p6mm*	1 rod – *6mm* 3 rods – *2mm*	Rotated Honeycomb (*f*=0.42)	—	—	—	—

Table 3-2. Comparison of band gap data for several group *6mm* crystal structures of dielectric rods ($\varepsilon_a = 11.4$) in air.

CHAPTER 4

Defect Modes in Two-Dimensional Photonic Crystals

Abstract

Physical defects in two-dimensional square photonic crystal structures are studied using the supercell plane-wave solution technique. Changing the radius of one of the rods in the crystal introduces allowed frequency states into the photonic band gap. These modes are strongly localized about the defect site and exhibit complex electromagnetic field patterns. Defect modes for the crystal of holes in a dielectric background are present in the absolute band gap for both E- and H-polarization waves, but these do not overlap to create an absolute defect band. The double-rod square structure has two rod types per unit cell, yielding different defect characteristics depending on which rod is altered. Selection of the smaller radius rod as the defect site decreases the effective size of the resonance cavity and reduces the number of allowed defect modes. The additional parameter afforded by the double-rod lattice may be useful in designing photonic crystal defect modes for applications.

4.1 Introduction

Perfect photonic crystals can inhibit electromagnetic waves from propagating through the crystal over a continuous range of frequencies, called the photonic band gap.[1] Band gaps have their origin in the scattering processes that occur when electromagnetic waves interact with the interfaces of dissimilar materials comprising the photonic crystal. By appropriately choosing the properties of the scattering elements (e.g., size, dielectric constant, lattice arrangement), one can design a crystal with a specific band gap. Multiple band gaps are possible for certain polarizations of the incident electromagnetic radiation. However, "absolute" band gaps that exist for all possible wave polarizations are usually limited in extent and harder to realize. Still, several different structures have been shown both theoretically and experimentally to possess photonic band gaps for all wave vectors and polarizations.[2-6]

The ability to control the reflection and transmission properties of light could lead to new physical phenomena when excited atoms are contained within a photonic crystal. Suppression or enhancement of spontaneous emission,[1,7] photon bound states,[8] and changing of the photon orbital angular momentum[9] are just a sampling of the events which can come about because of the interplay of atoms and photons with photonic crystals. Utilizing these properties could greatly improve the operation of various optoelectronic devices.[10-13] In addition, novel optical devices such as perfect channel-drop filters[14] are possible by utilizing the symmetry properties of defects in photonic crystals.

For applications such as semiconductor lasers and light-emitting diodes, it is desirable to channel as much of the energy as possible into a single mode. A perfect photonic crystal is not directly helpful for this application, as all frequencies within the gap are forbidden. With minor alterations, however, the crystal can provide narrow frequency modes within the band gap where light propagation is allowed.

A photonic band gap bears similarities to an electronic band gap: the electronic states in semiconductor crystals are arranged in energy bands separated by regions where no wavelike electron orbitals exist—the electronic band gap. Though this property makes semiconductors unique and important among the world of solids, these materials are most useful in applications when doped with small amounts of impurities. Very small amounts of dopant species can substantially alter the electronic properties of the bulk semiconductor. Through careful control of the amount and type of dopants used, discrete energy states are introduced into the electronic band gap. Electrons from the valence or conduction bands can hop into the band gap and occupy these new states at energies that were disallowed in the undoped semiconductor.

The introduction of defects into a photonic crystal can similarly affect the properties of light propagation. The photonic crystal can be "doped" by adding or removing material from certain sites within the lattice, or by replacing a small section of the crystal with a different dielectric constant material. These defect sites create new allowed frequency states within the band gap, providing a place for electromagnetic modes to couple to atoms, dipoles, or the substrate material.

4.2 Analogies Between Photonic Crystals and Semiconductors

Photonic crystal properties can perhaps be more easily understood by comparing them to the electronic properties of solid-state materials, where the concepts are more likely familiar. Many of the descriptive terms applied to the phenomena surrounding photonic crystals have their origin in the techniques and nomenclature of quantum mechanics and solid-state physics.

In the quantum mechanical description of atoms or molecules, the Schrödinger equation is used to obtain the allowed values of the energy for the system of particles. An isolated atom has a distinct set of energy levels that arise from the potential energy of the

electrons in the presence of the atomic nucleus and other electrons. In the case of molecules, additional energy states are formed by the molecular vibrations and rotations. When these atoms or molecules are in close proximity to each other, as in a semi-conductor material, they can no longer be treated as single entities, but rather behave as a single system with its own properties. Outer shell electrons are no longer bound to a single atom but belong to the bulk material. The close arrangement of atoms in a crystal lattice creates a periodic electronic potential. The solutions of the Schrödinger equation for the electron energy levels of this crystalline system split into many levels, spaced so tightly that they form energy bands. The highest partially filled energy band is called the conduction band, which is separated from the valence band below by the energy band gap.

A photonic crystal resembles a semiconductor material, where the atoms are replaced by macroscopic quantities of dielectric material and the electrons are instead electromagnetic waves. A classical formulation is used to describe wave propagation through the periodic potential created by the crystalline arrangement of two (or more) materials with different dielectric constants. The allowed frequencies of the electro-magnetic waves are solutions of the Maxwell equations and yield propagating modes inside the photonic crystal. For most bulk dielectric materials, the frequency solutions criss-cross through **k**-space, forming a continuous spectrum of allowed frequency bands. However, particular arrangements of dielectric materials can give rise to regions of the frequency spectrum in which no allowed frequency bands exist for all values of the wavevector. A "photonic band gap" opens between the allowed frequencies which is analogous to the energy band gap for semiconductors. Borrowing terminology from solid-state physics, we refer to the frequency band that forms the lower boundary of the photonic band gap as the valence band while the upper boundary defines the edge of the conduction band. As solutions to the Maxwell equations do not exist for frequencies

within the photonic band gap, electromagnetic waves with frequencies that fall within this gap are evanescent in the crystal.

The electrical and optical properties of semiconductor materials are significantly altered through doping, the intentional addition of small amounts of impurities. A dopant atom that has extra valence electrons as compared to the semiconductor atom it has replaced in the crystalline lattice is called a donor, as it contributes mobile electrons to the material. Similarly, an acceptor has fewer valence electrons than the normal lattice atoms, and helps create an excess of holes. In addition to influencing the conductivity of the material, the dopants also introduce discrete impurity energy levels into the band gap. Donor states are measured relative to the conduction band edge; acceptor states are likewise measured from the valence band edge.

It is similarly possible to dope a photonic crystal through the intentional disruption of the dielectric "atoms" in the crystal structure. A defect can be easily introduced by changing the size, shape, or dielectric constant of a feature in the crystal. The introduction of a single defect site changes the local potential function for an electromagnetic wave, creating the possibility of allowed frequency solutions that are forbidden in the bulk photonic crystal. These frequency defect modes lie within the photonic band gap, and are localized in space about the defect site. Extended modes of long range defect states can be created by disrupting the periodicity of the crystal through a line of defects or a physical space in between a plane of unit cells. In this way, defect modes can be guided through the photonic crystal structure by propagating along the path of defects.

As the dopant concentration in a semiconductor material increases, the discrete energy levels inside the band gap start to split into bands. Under conditions of very heavy doping, the donor (acceptor) impurity band can join with the conduction (valence) band, effectively decreasing the width of the band gap. As will be shown later, a similar effect

is also observed in photonic crystals when several defects are closely spaced in the structure.

4.3 Method of Defect Calculations

The plane wave expansion method, described in detail in Chapter 2, was used to calculate the photonic crystal frequency band structure. This method utilizes periodic boundary conditions at the edge of the unit cell, and implicitly assumes that the crystal is infinite in extent. The frequency solutions to Maxwell's equations are governed by the geometry of the materials within the unit cell as well as these periodic boundaries. The plane wave expansion method can be extended to crystals containing a defect by using a "supercell" approach.[15] Several small unit cells are combined together and the defect is introduced into this structure. The periodic boundary conditions are then applied to this large supercell, effectively creating an infinite crystal with regularly spaced defects. To determine the properties of a single defect, the supercell must be large enough in size so that the interaction between two adjacent defects is negligible. That is, we desire each defect to act like it is the only defect in an otherwise perfect crystal. As the defect modes inside the photonic crystal are localized about the defect site, it is possible to satisfy this requirement with a reasonably sized supercell (36 to 100 individual unit cells). This supercell plane wave method provides a convenient way to calculate the band structure of crystals with defect modes.

The greatest drawback of the supercell approach is that a large number of plane waves must be used to accurately describe the complex arrangement of dielectric material within the supercell. To retain the same level of accuracy as for a single unit cell calculation, a supercell comprising N unit cells requires the use of N times the number of plane waves.[16] Retaining a large number of plane wave requires much computer memory and also slows down calculations. Therefore, the supercell size must be judiciously

chosen so that it is large enough to reduce the artificial interactions of adjacent defects, yet sufficiently small to produce accurate calculations with a reasonable number of plane waves.

The calculations of the band structure and defect mode frequencies were performed using 1849 plane waves, the maximum possible within existing computer memory limitations. The profile of the dielectric function is well-described throughout most of the unit cell and the error introduced by the overshoot in the dielectric function (Gibbs' phenomenon at a jump discontinuity) is tolerable.

4.4 Results

4.4.1 Square Lattice of Holes in Dielectric

We first consider the single-rod square lattice of air holes in a background dielectric material ($\varepsilon_b = 11.4$). The band structure for the perfect crystal was previously discussed in Chapter 2, with the gap map shown in Fig. 2-5. A full photonic band gap is produced by an overlap of the H-polarization gap (H_2) with the upper E-polarization gap (E_3); the largest gap corresponds to a filling fraction of $f = 0.77$. Now we investigate the effects of introducing a physical defect into the crystal.

For the single-rod square lattice, $f = 0.77$ corresponds to a hole radius of $r = 0.495a$. As the lattice is nearly close-packed, the defect is most easily created by decreasing the size of one of the holes in the crystal (i.e., more high dielectric constant material is added). The hole is entirely filled in when $r = 0$.

We begin by examining the influence of the defect on the lower E-polarization gap, which occurs between the first and second bands. Figure 4-1 shows the results of the band gap calculations for supercells with an increasing number of unit cells. As the defect hole is slowly filled in, three defect states enter the photonic gap from out of the conduction band. Since these modes originate in the conduction band they are termed

"donor" levels, utilizing the analogy with semiconductors. The first donor mode appears when the defect radius is $r = 0.46a$. This is a non-degenerate mode that traverses across the width of the band gap as the radius of the defect hole gets smaller. This mode merges with the valence band at $r = 0.11a$. Two other defect modes also appear as the hole radius changes: another non-degenerate defect state, and a state composed of a pair of degenerate modes. Like the first defect mode, these also descend into the photonic gap from out of the conduction band. However, they remain well within the gap even when the defect hole is entirely closed. A unique feature of these latter two defect bands is that they cross when the hole radius is $0.3a$. At this point, there are three distinct electromagnetic field modes (one non-degenerate mode plus a degenerate pair) that share a common frequency. Comparison of the three plots in the figure shows that the defect bands become narrower in frequency as the size of the supercell increases. When the supercell size is small [Fig. 4-1(a)], the electromagnetic fields localized about the defect sites do not dissipate sufficiently before an adjacent defect is encountered. The communication between these defect sites results in a broadening of the defect bands.[17] This phenomenon is analogous to the broadened energy levels present within the energy gap of a heavily doped semiconductor. The defect modes of the photonic crystal also show slightly more broadening near the edges of the gap. This broadening comes about as the localized nature of the defect mode meets with the extended modes of the continuum of states. The transition is not abrupt; rather, the localized mode tries to blend smoothly into the continuum, gradually becoming less and less confined to the site of the physical defect as the defect mode approaches and enters the band of states.

The electric field is polarized along the axis of the rods and therefore it is easy to plot the magnitude of the electric field inside the supercell. The distribution of the electric field inside the 100 unit supercell is shown in Fig. 4-2 for the three defect modes, for various sizes of the defect rod. The character of each mode remains the same even as the defect size changes. The first defect state (mode 1) has a maximum field intensity

located at the very center of the defect. Following the descriptive terms used in Ref. 18, we label this mode a monopole since it possesses a single maximum without a node in the azimuthal direction. The second defect state (mode 2) is deemed a quadrupole, also with the electric field localized about the defect site. The bottom row of the plot shows one of the pair of degenerate dipole states of the third defect mode. As one moves from left to right in the figure, the defects descend further into the photonic gap away from the conduction band edge. The modes become more localized about the defect site, as evidenced by the smaller field intensities near the edges of the unit cell. The electromagnetic fields are strongly localized in space around the location of the defect.

The introduction of a defect also influences the bands that form the absolute band gap, H_2 and E_3, which appear at higher frequencies than the E_1 gap previously discussed. Though we can still apply the same supercell solution technique to find the defect characteristics as was done before, we encounter some difficulties. The bands at higher frequencies are much more sensitive to changes in the crystal structure than are the lower bands.[18] Similarly, these higher bands will also be sensitive to artificial changes in the lattice structure, as those introduced through the error in the Fourier series expansion of the dielectric constant. Thus, to achieve the same degree of accuracy in the solutions for these higher bands requires many more plane waves than for the lower bands. Unfortunately, the computer memory resources available limit the maximum number of plane waves to 1849, as used for the lower E gap calculations. A preliminary study showed that significant error (up to 15 percent variation in the band gap width) is present in the frequency solutions for the higher gaps. It should be noted that this error is not inherent to the solution method, but rather a reflection of our failure to retain a sufficient number of terms in the plane wave expansion.

Due to the large errors in the calculated frequencies, a definitive description of the defect frequencies present in the absolute gap is difficult. However, if the solutions for these higher frequency gaps are accepted with caution, it is possible to gain some

understanding of the defect mode characteristics. With this warning in mind, we proceed with a qualitative description of the defect states.

Figure 4-3 shows the band frequencies as a function of the defect size for the H-polarization gap. The supercell used in this calculation contains 64 unit cells. As before, we begin with a perfect crystal with all of the holes having a radius of $0.495a$, then slowly decrease the size of one of the holes. A total of five defect states are seen to drop down out of the conduction band and into the photonic gap. All of these states appear as bands, artificially broadened due to the small size of the supercell. This impurity band effect is especially apparent near the conduction band edge. Sudden jumps in the width of the photonic band gap occur as the broad defect bands merge with the continuum. Note that this effect is much more severe for this structure than for the E_1 gap—another indicator of the sensitivity of these higher lying bands. The degree of degeneracy of a particular defect mode is shown in the figure with solid and dashed lines representing non-degenerate and doubly-degenerate modes, respectively. The first four defect states traverse the gap as the defect rod radius decreases, and eventually reach the valence band. The last defect mode, a degenerate pair, remains contained within the band gap even when the hole has been completely filled ($r = 0$).

The band plot for the upper E-polarization gap displays similar characteristics, as shown in Fig. 4-4. Again, five defect states are present for this structure, three non-degenerate modes, and two doubly-degenerate ones. In contrast to the H-polarization case, these modes enter the photonic gap in close proximity to each other. The first two modes appear to cross in frequency twice as they make their way through the gap. The second and third defect appear to merge with each other before entering the valance band. Likewise, the fourth and fifth bands leave the conduction band intertwined before splitting into two separate defect modes. It is difficult to state with certainty if these band mergers are the result of interaction between the localized electromagnetic fields of adjacent defect sites, or if they are a symptom of the poor calculation accuracy. The

results of the lower E-polarization gap suggest the former to be true, and that using a larger supercell will produce discrete frequencies that do not merge together.

Now that we have considered the effects of the crystal defect on each wave polarization separately, we can combine the results to model the modes present inside the absolute band gap. Though a fairly dense array of defect states appear over most values of the defect rod radius, none of the defect modes from the two orthogonal polarizations overlap. An "absolute defect" within the absolute gap does not exist for this structure.

4.4.2 Square Lattice of Dielectric Rods in Air

The band structure of a photonic crystal composed of dielectric rods in air was examined in Chapter 2. Recall that for the single-rod structure, several E-polarization gaps exist over a large range of filling fractions, while no H-polarization gaps appear for any rod configuration. The addition of a different diameter rod into the unit cell was shown to greatly increase the size of the absolute gap for the crystal structure of holes in dielectric. However, applying the same technique in the case of dielectric rods does not result in the appearance of any significant H-polarization gaps. A gap map for the double-rod crystal structure at a filling fraction of 0.126 is shown in Fig. 4-5, where non-dimensionalized frequencies are plotted as a function of the rod-diameter ratio. Though gaps for H-polarized waves are clearly absent, the E-polarization gaps remain large at several values of the rod diameter ratio. Consider the crystal formation at the point where $\beta = 0.3$. The lowest frequency gap for this structure appears between bands E_1 and E_2, and is only slightly reduced in size from the single-rod structure (at $\beta = 0$). An important difference between these structures is that in the former case two different kinds of elements exist inside the unit cell. There is now a choice as to which element may be perturbed to create a defect in the crystal, and the properties of the defect mode should be different depending on which type of rod is manipulated.

First, we examine the lowest E-polarization gap when a defect is introduced into the single-rod structure. We begin with a perfect crystal where every rod has a radius of $0.2a$ (filling fraction $f = 0.126$), and slowly decrease the radius of one of the rods inside a 100 unit supercell. This crystal structure has previously been investigated by another group[19] and shown to have many interesting defect properties. We will present our results here for completeness and comparison with other crystal structures. Figure 4-6 shows the frequencies of the defect modes inside the photonic band gap as the radius of the defect rod changes. The perfect photonic crystal is represented by the vertical dashed line. Almost immediately after the radius of the rod is less than $0.2a$, a defect state enters the gap from the valence band. This non-degenerate mode increases in frequency as the defect rod gets smaller, ending with a frequency of $0.38(2\pi c/a)$ when the rod is completely removed. This mode is the only one that appears when material is removed from the crystal. In contrast, many defect states appear when material is added to the lattice by increasing the size of the defect rod. The first mode is a doubly-degenerate state that appears out of the conduction band at a defect radius of $0.24a$. This mode sweeps across the gap, rejoining the continuum of states in the valence band at $r = 0.44a$. At about the same point, three non-degenerate states drop out of the conduction band and begin to sweep their way across the gap. Five other defect modes also appear as the size of the defect rod is increased to $0.8a$, when it begins to touch the nearest neighbor rods.

Now, consider a double-rod crystal structure that has the same filling fraction ($f = 0.126$) as the above case but with a rod diameter ratio of $\beta = 0.3$. The radii of the rods in this structure are therefore either $0.271a$ or $0.0813a$, and there is a choice as to which element to select as the site of the crystal defect. Varying the size of one of the larger rods results in the defect band plot shown in Fig. 4-7. This plot is very similar to that for the single-rod structure. Again, one non-degenerate acceptor mode emerges from the valence band when the size of the rod is decreased. For an increase in the rod radius, a doubly degenerate donor appears, followed by three non-degenerate modes. The relative

position and slope of all of these modes is quite similar to what was found in Fig. 4-6. However, the bands plots for these two structures differ in the modes that appear at large values of the defect radius; the last three non-degenerate modes that were present in the single-rod structure are absent for the double-rod case.

A very different defect band structure is obtained when the smaller radius rod is chosen as the defect site (Fig. 4-8). In this case, there are no acceptor modes present even when the small rod is entirely removed from the structure. When the rod diameter is increased above $0.12a$ a non-degenerate mode drops out of the conduction band and sweeps across the gap, merging with the valence band at $0.32a$. A range with no defect modes follows until a doubly-degenerate donor mode appears at $0.4a$. It is joined by three non-degenerate defect modes as the rod radius increases further. These modes remain within the band gap even when the defect rod radius is increased to the maximum, where it touches the nearest neighbor rods. The defect structure for the smaller radius rod supports fewer modes than was the case for the larger rod defect, even though the bulk crystal structure is identical for both. We interpret this difference as the result of a change in the effective size of the resonance cavity created by the dielectric material surrounding the defect. The larger radius rods primarily contribute to confinement of the defect mode, as the greater extent of high dielectric constant presents a larger barrier to the light than do the smaller rods. The smaller rod defect is enclosed by four large rods as nearest neighbors, creating a smaller resonance cavity than for the case of the large rod defect which is enclosed by other large rods as second-nearest neighbors. Since fewer modes can exist inside a smaller cavity volume, we see fewer defect modes present for the small rod defect that for the large rod case.

Additional information is gained through comparison of the electric field distributions for the defect modes in each of the above structures. The modes for the single-rod lattice with rods of radius $0.2a$ are shown in Fig. 4-9. The field distribution for the acceptor mode at $r = 0.075a$ [Fig. 4-9(a)] shows that the defect is a classic monopole:

the field is concentrated at the center of the defect and decays rapidly away from this site. The other electric field patterns in Fig. 4-9(b)–(j) are the donor modes shown in the order in which they appear in the photonic gap as the defect rod radius is increased. In order to be proper eigenfunctions (i.e., solutions of the Maxwell equations subject to the boundary conditions of the photonic crystal) each mode must be orthogonal to the others.[†] This requirement gives birth to a variety of fascinating field patterns that surround the defect. The dipole in (b) is one of the pair of doubly-degenerate states that appear at a defect rod radius of $0.3a$. The other mode of the degenerate pair (not shown) is rotated 90° with respect to this one, keeping in line with the *4mm* symmetry of the structure. This mode pair is followed by three non-degenerate modes: (c) a quadrupole, (d) another quadrupole with different orientation, and (e) a second-order monopole. These field patterns are shown at rod radii where the modes occur at frequencies near the middle of the photonic gap, such that localization of the fields about the defect should be the greatest. One of a degenerate pair of hexapole modes is shown in (f), perhaps a surprising field pattern considering the *4mm* lattice symmetry. Another mode of a degenerate pair, a second-order dipole, occurs in (g). The modes of these degenerate pairs transform into each other under a 90° rotation, satisfying the point symmetry of the defect site within the supercell. Increasing the radius of the defect rod further yields octopoles in (h) and (i), and finally a second-order monopole in (j). These last three modes are shown for the case when the defect rod just begins to touch its nearest neighbors ($r = 0.8a$).

Next, we compare the electric field distributions for the double-rod structures. Figure 4-10 shows the defect modes present for the case discussed previously, when one of the large rods is selected as the defect. A monopole acceptor mode appears in (a) when the rod radius is decreased to $r = 0.07a$. This mode pattern is very similar in shape to that in Fig. 4-10(a), but the maximum magnitude appears to extend over a larger area of the

---

[†] The exception to this requirement is in the case of degenerate modes, which have equal frequencies and whose eigenfunctions are not necessarily orthogonal.

unit cell. This observation also supports the conjecture that the effective cavity volume of the defect site in this structure is larger than for the small rod defect. The field plots in (b)–(g) are the donor modes for this structure. Modes (b), (f), and (g) are one of doubly-degenerate pairs, while (c), (d), and (e) are non-degenerate. The electric field patterns evolve in the same manner as the modes for the single-rod structure, with the exception that the orientations of the quadrupole modes appear to be reversed. Actually, it is because the position of the large rods nearest the defect site that are rotated 45° with respect to the nearest neighbor rods for the single-rod structure that causes the apparent switch in the order of the modes.

The electric field patterns for the double-rod lattice with the rod of smaller radius used as the defect site are shown in Fig. 4-11. As was shown in the band plot for this structure, no acceptor modes exist even for complete removal of one of the rods. Thus, the field pattern of the first donor mode can take the form of a monopole, as shown in Fig. 4-11(a). Note how much more localized this mode appears compared with that of Fig. 4-10(a). Further increase in the radius of the defect rod leads to a degenerate dipole pair shown in (b), two non-degenerate quadrupoles in (c) and (d), and a second-order monopole in (e). The field plots for the last two modes are shown for the case when the defect rod is nearly touching the nearest neighbor rods. The defect frequencies are still fairly close to the conduction band edge at this point, as recognized from the less-localized appearance of the electric fields in the plots.

4.5 Discussion

In the design of photonic crystals with physical defects for optoelectronic applications (e.g., light-emitting diodes) two factors must be considered. First, the electromagnetic energy of the system should be confined to one or a few discrete modes,

with minimized losses to other undesired modes. Second, the electromagnetic radiation must have a way to exit the photonic crystal into the device.

We have shown that it is relatively easy to satisfy the first condition. The introduction of a single physical defect can produce discrete allowed frequency modes within the otherwise forbidden frequency regime of the photonic band gap. Since these frequencies lie within the gap, the fields are evanescent away from the site of the defect. The energy is confined within a kind of resonance cavity. The quality factor Q for the cavity can become very large when the physical defect is isolated inside the photonic crystal (i.e., for large supercells).[19] For many applications, what is desired most is a single pure allowed state. Consider the band plot for the E_1 gap in Fig. 4-1(c), where the second and third defect states cross at a common frequency value. Though they share the same frequency at this point, this particular crystal structure may not be desirable for some applications, as energy can be dissipated into three distinct mode patterns. For these applications it may be preferable to instead utilize the first defect state, a non-degenerate mode that is well-confined within the photonic band gap and does not intersect any other defect states. However, the unique characteristic of two different symmetry modes sharing a common frequency might be useful should energy from dissimilar sources need to be coupled into a common frequency.

To be useful for applications, the energy trapped within the defect mode must be able to interact with the world outside of the crystal. The most efficient means of extracting (imparting) energy from (to) the defect mode is by coupling the resonance to another mode or field pattern with a large overlap. That is to say, the symmetry of the resonance mode is an important consideration in how one chooses to couple to the energy. In the example above, the first defect state of the E_1 has a monopole-like field pattern, and therefore a monopole source placed at the defect site would provide a means of very efficiently pumping energy into this mode. Conversely, this resonant mode would best excite an atom or wave which has the same monopole symmetry.

These factors, as well as the ease of fabrication, must be considered in the design of photonic crystal structures. The double-rod crystal structure of dielectric rods in air has an advantage over the holes-in-dielectric case, as the thin walls present in the latter have been eliminated. This makes the rod structure much easier to fabricate especially at sub-micron length scales. In addition, the double-rod structure has an extra degree of freedom in selecting the defect properties of the crystal. By varying either the small or large radius rod, very different frequency characteristics can be obtained. For the case when the small radius rod is used as the defect, the monopole mode can be tuned to any frequency within the photonic band gap by appropriately adjusting the rod radius. This is an advantage over both the single-rod lattice and the double-rod lattice with the large rod defect, as in these structures the monopole mode ranges over the lower half of the photonic band gap only.

4.6 Conclusions

We have shown that the introduction of a different size scattering element into a photonic crystal can produce allowed frequency modes within the photonic band gap that are strongly localized about the site of the defect. The frequencies and symmetry properties of these modes can be controlled by varying the size of the defect. As more defect sites are introduced into the crystal, the discrete frequency modes broaden into bands analogous to the effect in heavily doped semiconductors. For the single-rod square lattice of holes in a dielectric background, two modes with distinct field patterns can be made to coexist at the same frequency. This frequency crossing may not be of interest for light-emitting applications, but might be useful for coupling fields with differing symmetry patterns. For the double-rod structure of dielectric rods in air, the choice of two lattice elements as defect sites leads to different defect mode properties for each case.

The supercell approach is a convenient method for calculating the defect mode properties of photonic crystals but has one drawback: a very large amount of computer memory is required to retain a sufficient number of plane wave expansion terms for accurate results. The errors introduced by considering too few plane waves are small for the lower lying bands, but rapidly become significant as the band frequencies increase. Thus, a different solution technique that overcomes this problems is required for accurate numerical solutions of the defect modes in the upper bands.

4.7 References

[1] E. Yablonovitch, "Inhibited Spontaneous Emission in Solid-State Physics and Electronics," *Phys. Rev. Lett.* **58**, 2059 (1987).

[2] R. D. Meade, K. D. Brommer, A. M. Rappe, and J. D. Joannopoulos, "Existence of a Photonic Band Gap in Two Dimensions," *Appl. Phys. Lett.* **61**, 495 (1992).

[3] C. M. Anderson and K. P. Giapis, "Larger Two-Dimensional Photonic Band Gaps," *Phys. Rev. Lett.* **77**, 2949 (1996).

[4] D. Cassagne, C. Jouanin, and D. Bertho, "Photonic Band Gaps in a Two-Dimensional Graphite Structure," *Phys. Rev. B* **52**, R2217 (1995).

[5] C. M. Anderson and K. P. Giapis, "Symmetry Reduction in Group *4mm* Photonic Crystals," *Phys. Rev. B* **56**, 7313 (1997).

[6] C.-S. Kee, J.-E. Kim, and H. Y. Park, "Absolute Photonic Band Gap in a Two-Dimensional Square Lattice of Square Dielectric Rods in Air," *Phys. Rev. E* **56**, R6291 (1997).

[7] K. A. Shore, "Control of Spontaneous Emission in Microcavity Laser Diodes," *Physica B* **175**, 123 (1991).

[8] S. John and J. Wang, "Quantum Optics of Localized Light in a Photonic Band Gap," *Phys. Rev. B* **43**, 12772 (1991).

[9] J. D. Joannopoulos, P. R. Villeneuve, and S. Fan, "Photonic Crystals," *Solid State Comm.* **102**, 165 (1997).

[10] H. Yokoyama, "Physics and Device Applications of Optical Microcavities," *Science* **256**, 66 (1992).

[11] E. Yablonovitch, "Photonic Band-Gap Structures," *J. Opt. Soc. Am. B* **10**, 283 (1993).

[12] A. Mekis, J. C. Chen, I. Kurland, S. Fan, P. R. Villeneuve, and J. D. Joannopoulos, "High Transmission Through Sharp Bends in Photonic Crystal Waveguides," *Phys. Rev. Lett.* **77**, 3787 (1996).

[13] J. C. Knight, T. A. Birks, P. St. J. Russell, and D. M. Atkin, "All-Silica Single-Mode Optical Fiber with Photonic Crystal Cladding," *Opt. Lett.* **21**, 1547 (1996).

[14] S. Fan, P. R. Villeneuve, J. D. Joannopoulos, and H. A. Haus, "Channel Drop Tunneling through Localized States," *Phys. Rev. Lett.* **80**, 960 (1998).

[15] R. D. Meade, K. D. Brommer, A. M. Rappe, and J. D. Joannopoulos, "Photonic Bound States in Periodic Dielectric Materials," *Phys. Rev. B* **44**, 13772 (1991).

[16] K. Sakoda, "Numerical Study on Localized Defect Modes in Two-Dimensional Triangular Photonic Crystals," *J. Appl. Phys.* **84**, 1210 (1998).

[17] X.-P. Feng and Y. Arakawa, "Defect Modes in Two-Dimensional Triangular Photonic Crystals," *Jpn. J. Appl. Phys.* **36**, L120 (1997).

[18] M. M. Sigalas, C. M. Soukoulis, C.-T. Chan, and D. Turner, "Localization of Electromagnetic Waves in Two-Dimensional Disordered Systems," *Phys. Rev. B* **53**, 8340 (1996).

[19] P. R. Villeneuve, S. Fan, and J. D. Joannopoulos, "Microcavities in Photonic Crystals: Mode Symmetry, Tunability, and Coupling Efficiency," *Phys. Rev. B* **54**, 7837 (1996).
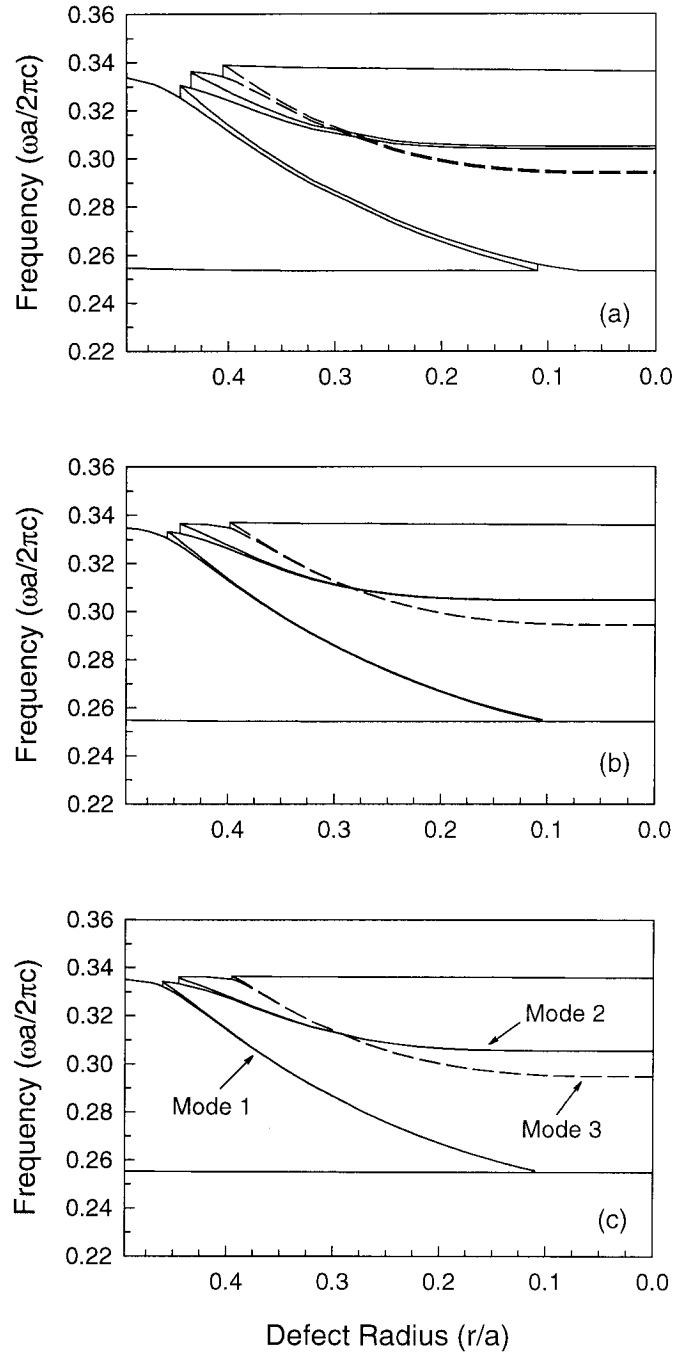
Fig. 4-1. Frequency of defect states for the E_1 gap in the single-rod square structure of air holes in a dielectric background ($\varepsilon_b = 11.4$) with supercells of (a) 36, (b) 64, and (c) 100 unit cells. The holes in the perfect structure have radius $0.495a$, with the defect introduced by decreasing the radius of one of the holes. The modes within the photonic band gap may be non-degenerate (solid lines) or doubly-degenerate (dashed lines). The defect modes exist as bands for the smaller supercell, becoming more discrete as the supercell size increases. Note the frequency crossing of the second and third modes.
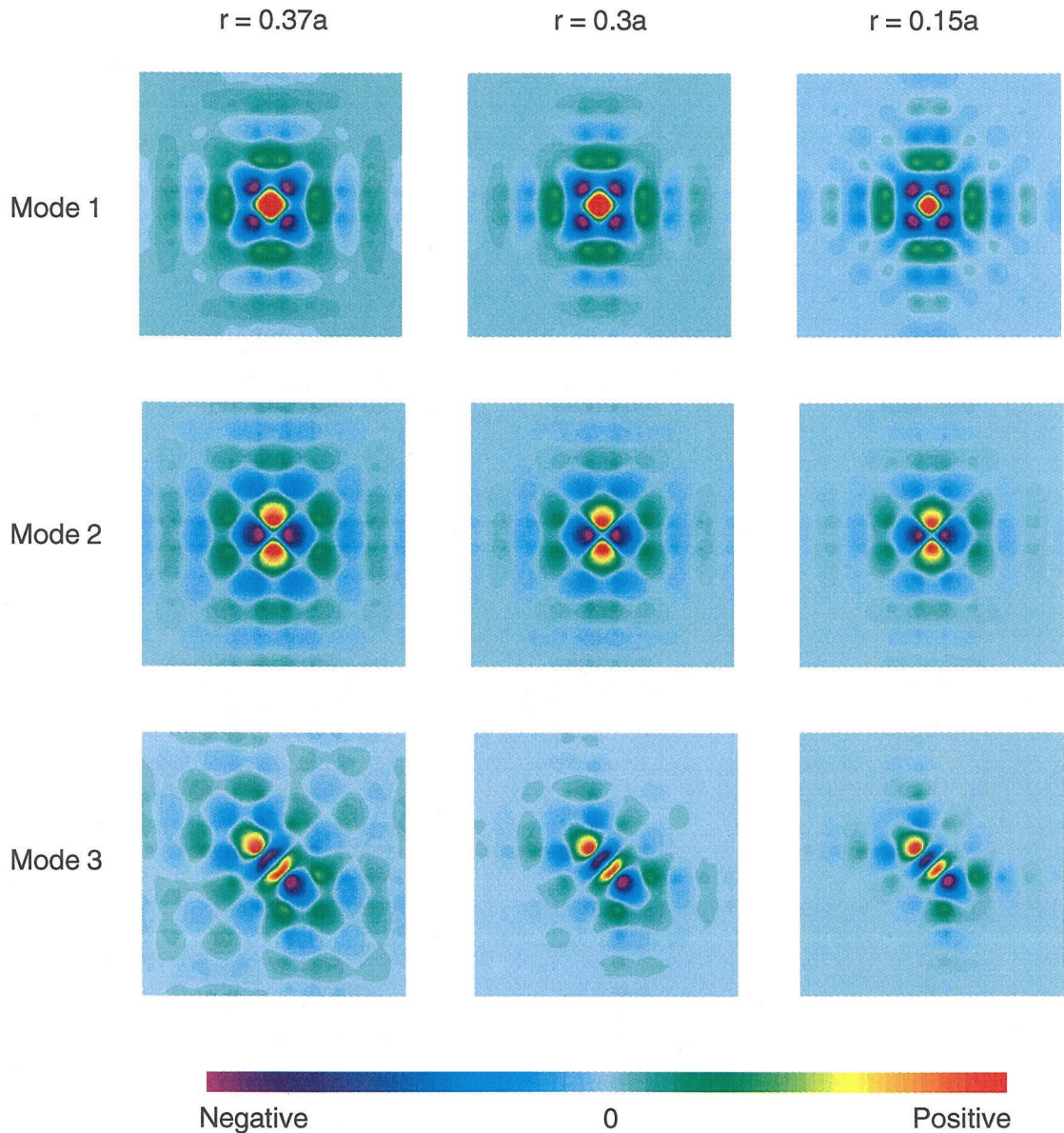
Fig. 4-2. Magnitude of the electric field for three defect modes of the single-rod square structure of holes ($r = 0.495a$) in dielectric, shown for the 100 unit supercell. The third mode is one from a pair of degenerate states. The electric field patterns are calculated for three different values of the defect rod radius. Modes 2 and 3 have the same frequency when $r = 0.3a$. As the rod radius decreases, the mode frequencies approach the middle of the photonic band gap and the resonant electric field becomes more localized about the defect site.
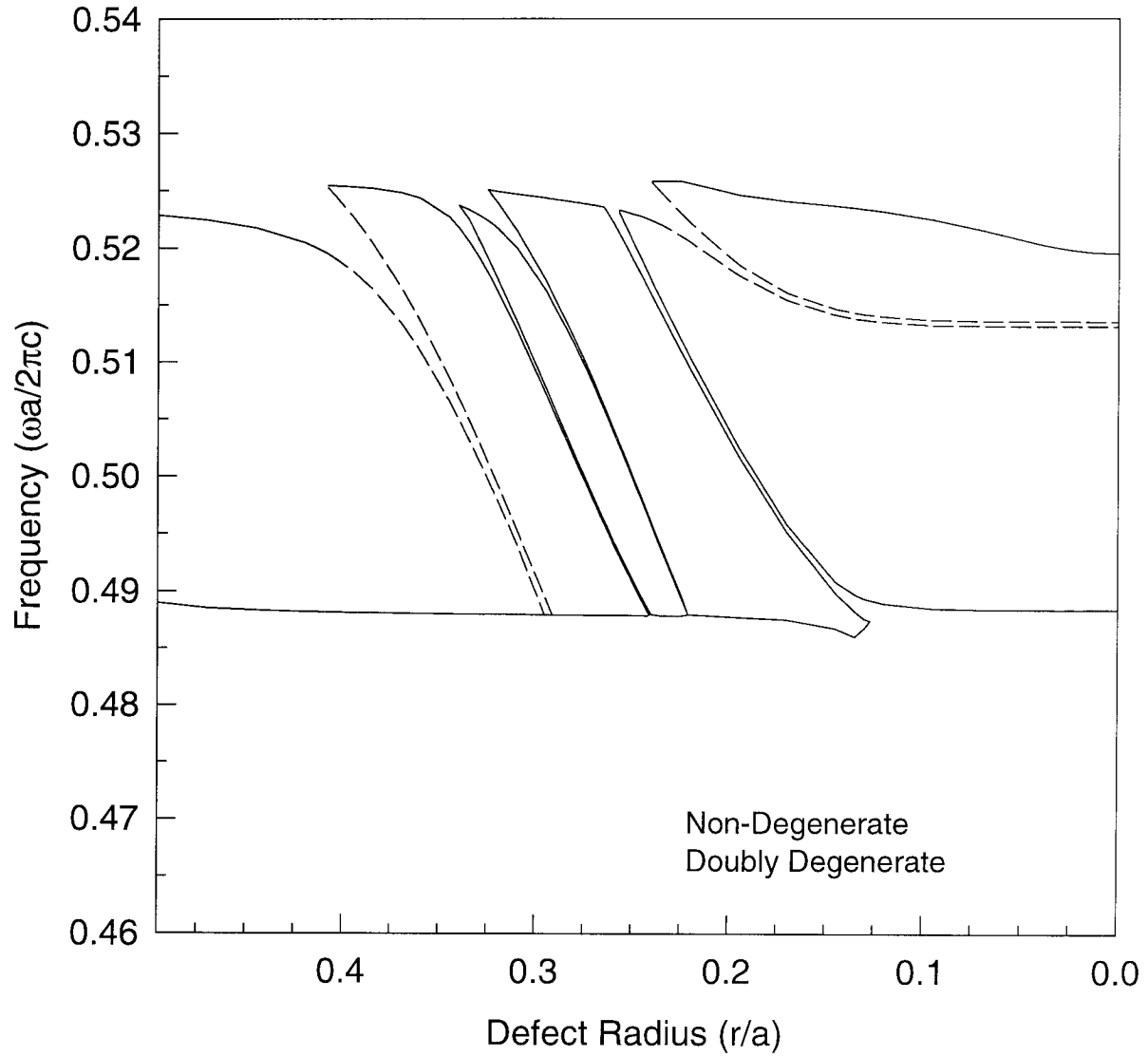
Fig. 4-3. Frequency of the defect states for the H_2 gap in the single-rod square structure of air holes ($r = 0.495a$) in a background dielectric ($\varepsilon_b = 11.4$). The calculation is performed for a 64 unit supercell. Five defect modes leave the conduction band and enter the photonic band gap as the radius of one of the holes is decreased. The defect frequency bands broaden as they near the conduction band edge, producing a discrete jump in the photonic gap frequency at the points where they merge.
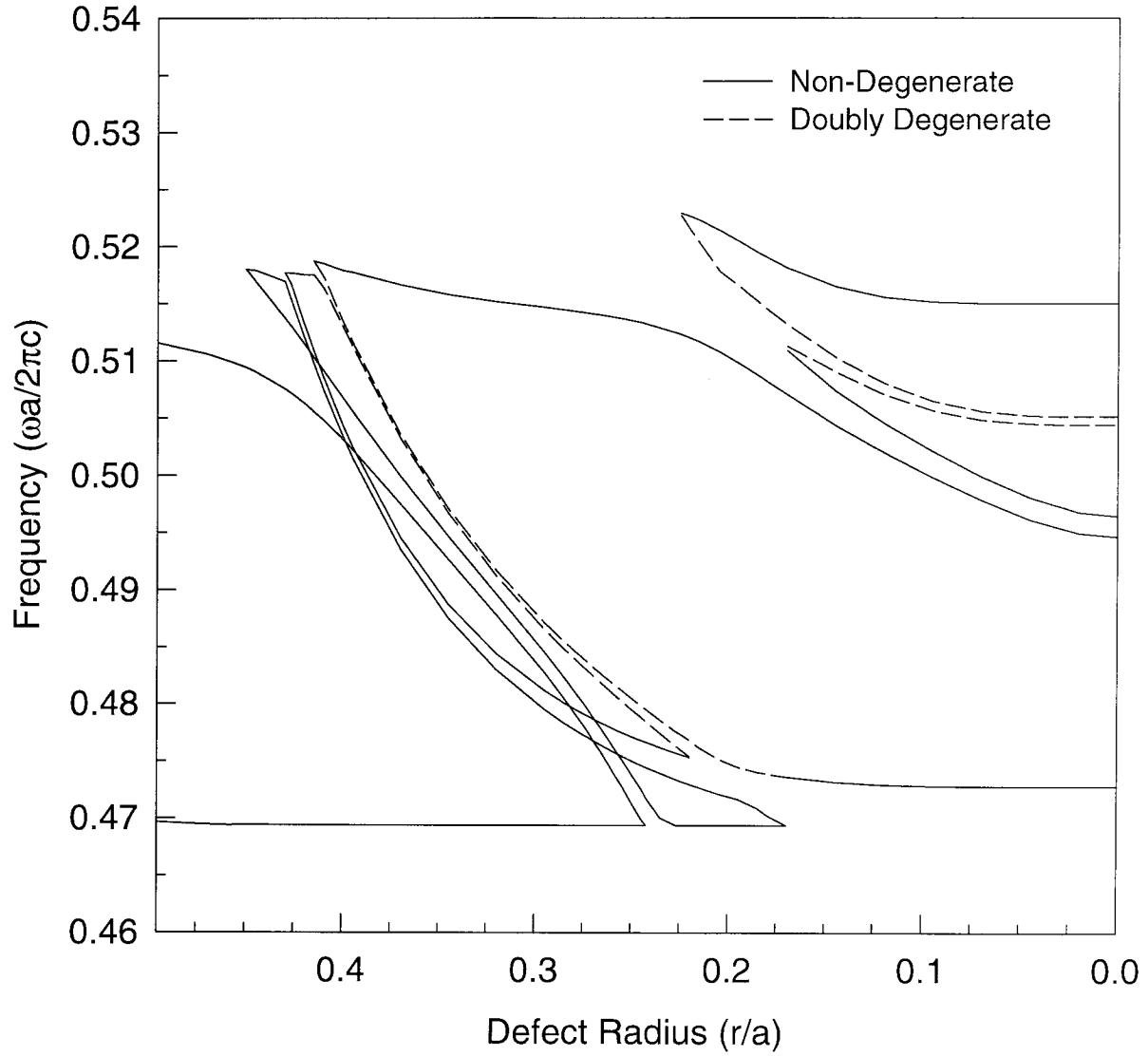
Fig. 4-4. Frequency of the defect states for the E_3 gap in the single-rod square structure of air holes ($r = 0.495a$) in a background dielectric ($\varepsilon_b = 11.4$), calculated with a 64 unit supercell. As for the H-polarization case, discrete jumps in the photonic band gap width occur when broadened frequency bands merge with the continuum of states. The first two defect modes cross in frequency twice as they traverse the band gap.
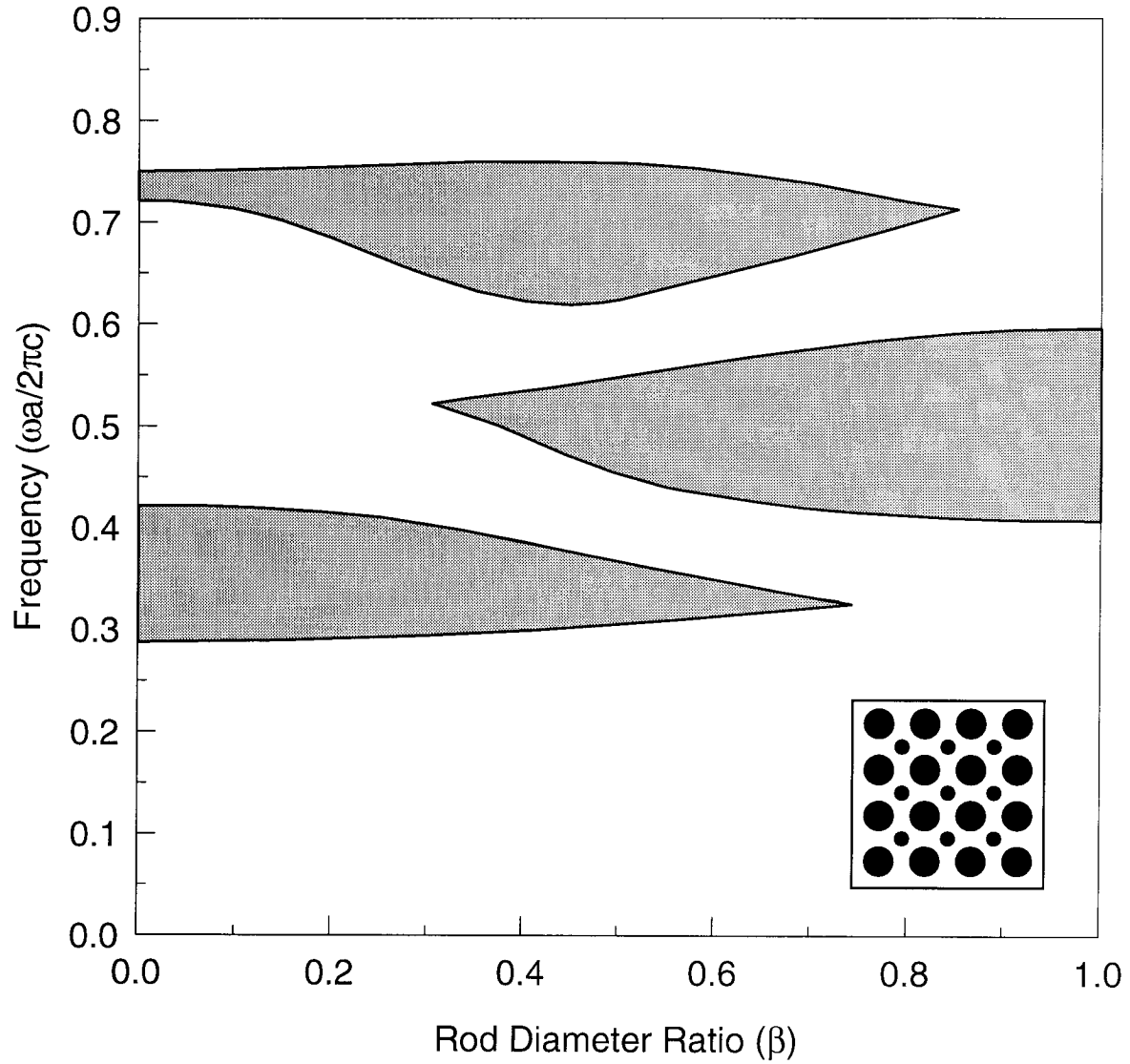
Fig. 4-5. Gap map for the double-rod square structure of dielectric rods ($\varepsilon_b = 11.4$) in air as a function of β, the ratio of the two rod diameters. The structure has a filling fraction $f = 0.126$, equivalent to a rod radius of $0.2a$ at $\beta = 0$. The single-rod structure is recovered at either $\beta = 0$ or 1. Three large E-polarization gaps exist for a range of β values.
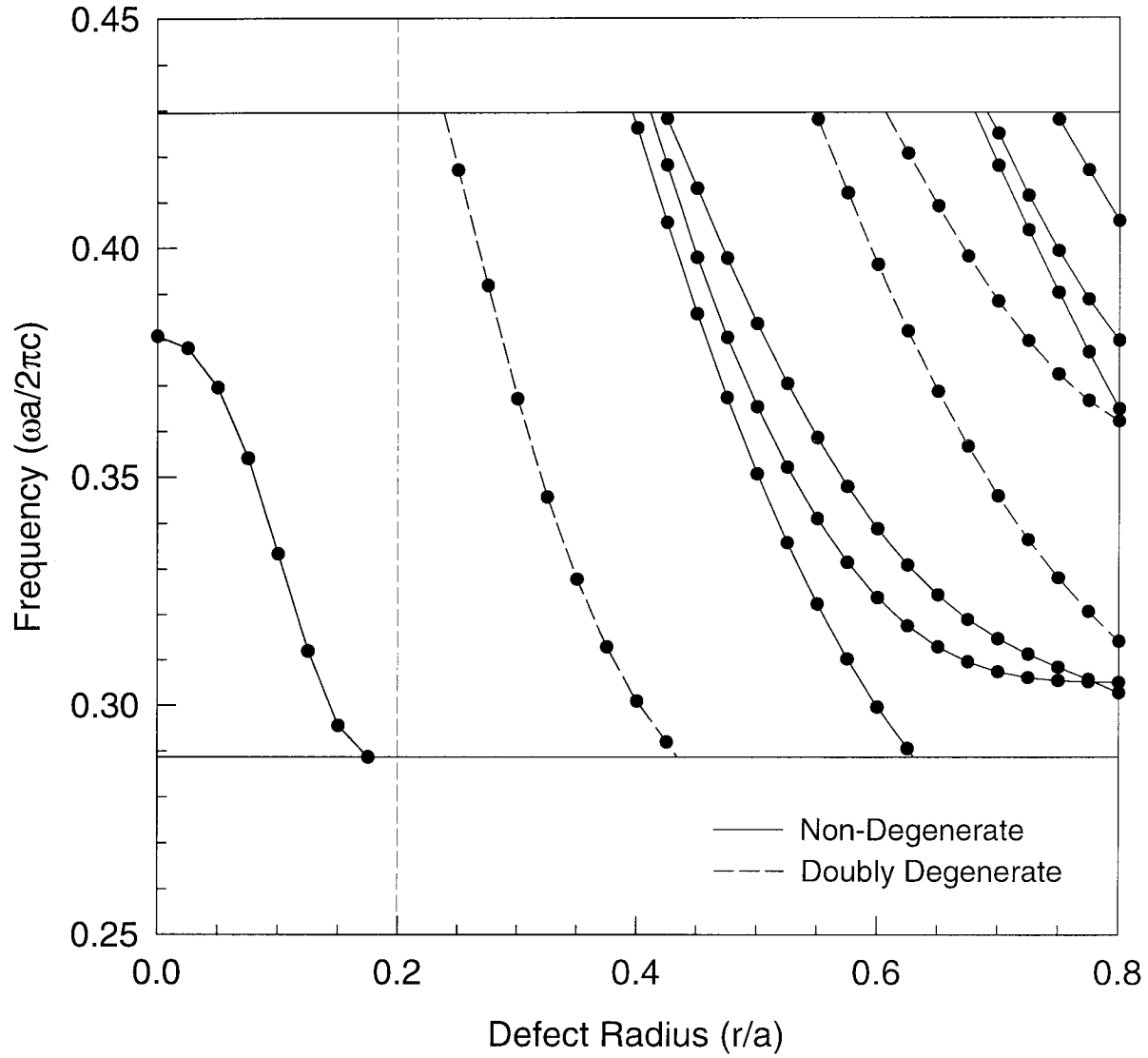
Fig. 4-6. Frequency plot of the defect states in the single-rod square structure of dielectric rods with radius $0.2a$, calculated with a 100 unit supercell. The vertical dashed line indicates the location of the perfect array. Decreasing the radius of the defect rod creates a single acceptor mode within the photonic band gap. Several donor modes enter the gap as the rod radius in increased up to the maximum $r = 0.8a$, when the defect rod first touches the nearest-neighbor rods.

Fig. 4-7. Frequency plot of the defect states in the double-rod square structure ($f = 0.126$, $\beta = 0.3$) of dielectric rods in air. In this case, one of the larger radius rods ($r = 0.271a$) is chosen as the defect site. The vertical dashed line indicates the location of the perfect array. The single acceptor mode still exists, though fewer donor modes enter the gap as compared with the single-rod structure.
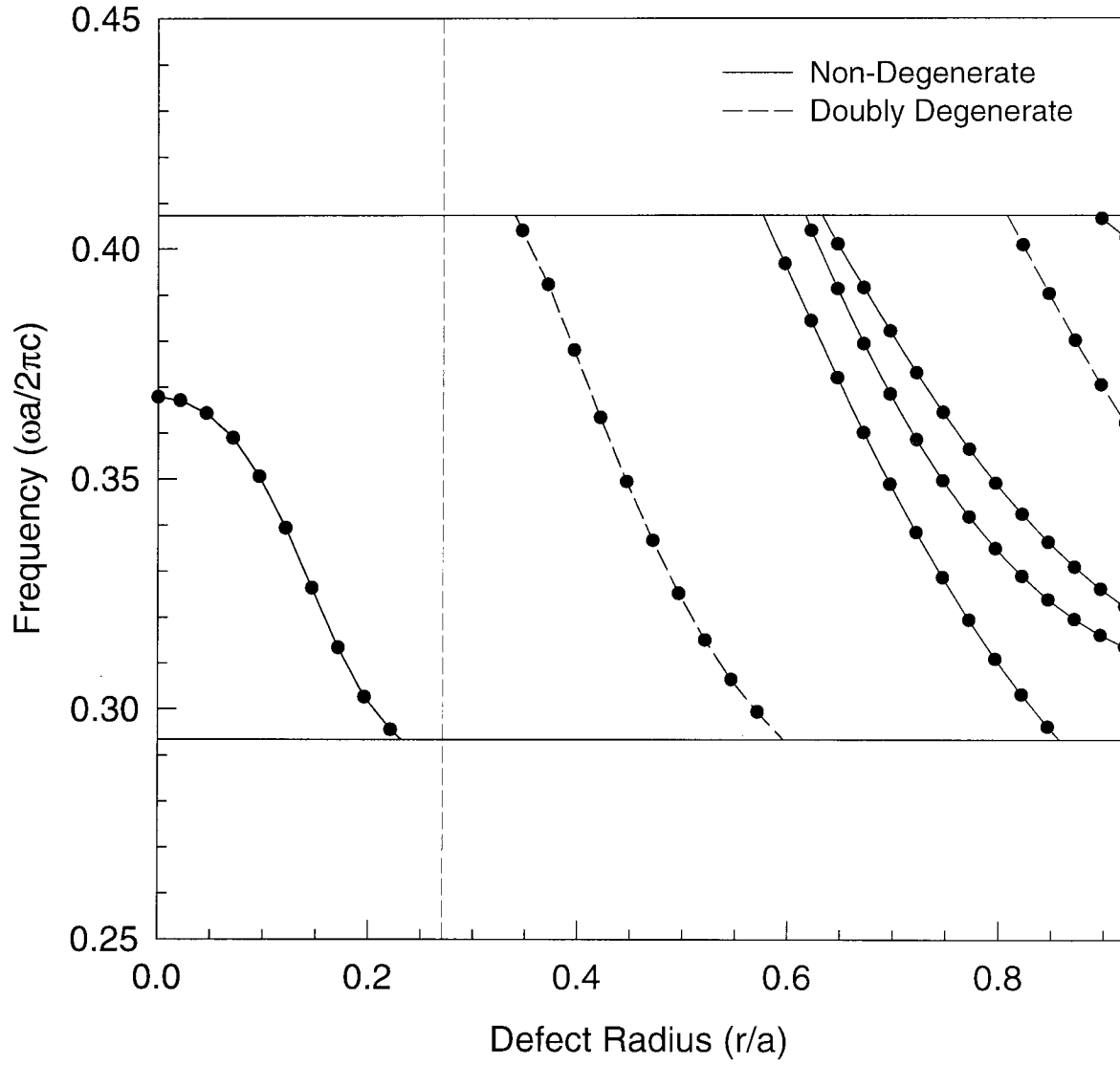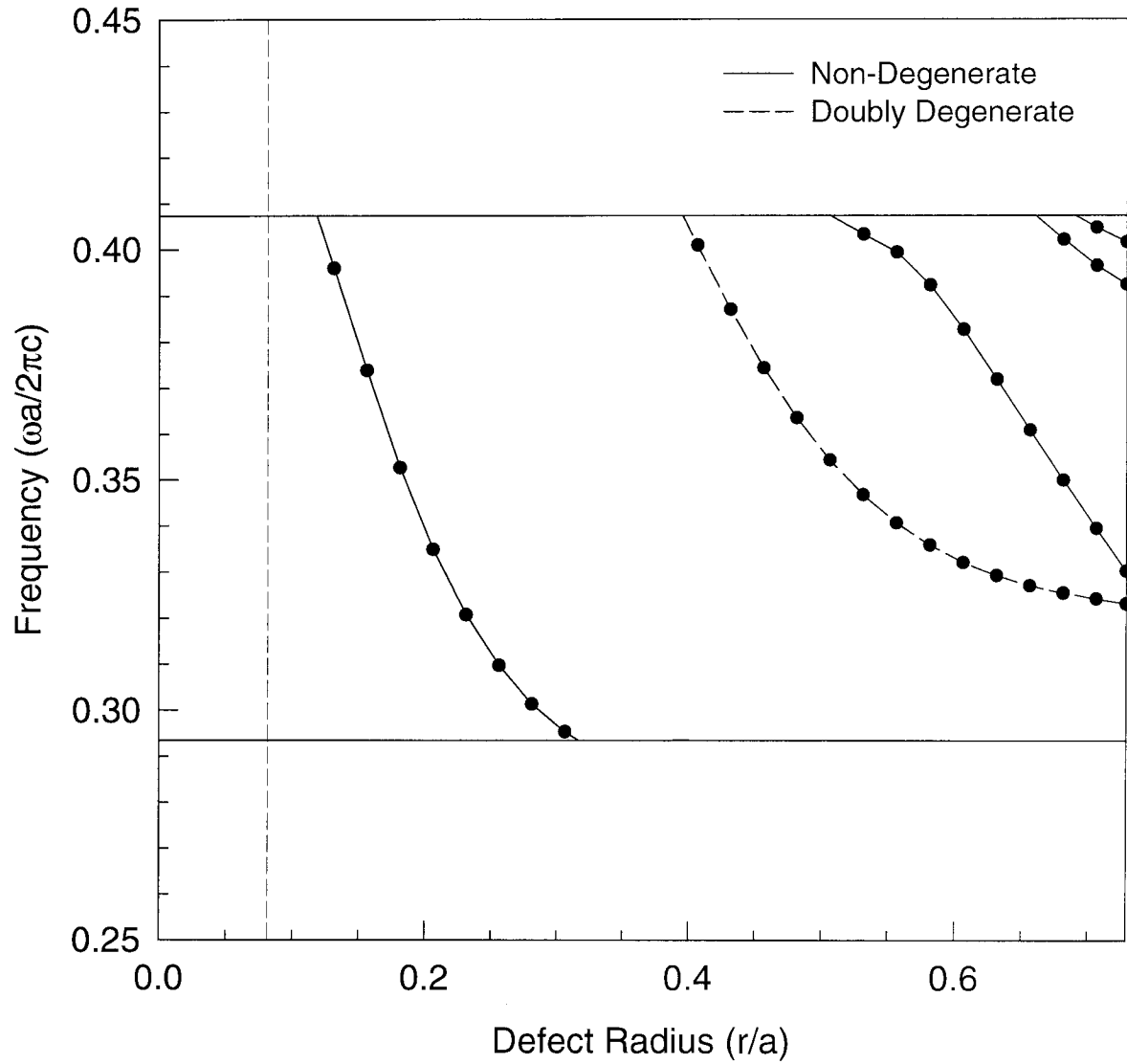
Fig. 4-8. Frequency plot of the defect states in the double-rod square structure ($f=0.126$, $\beta=0.3$) of dielectric rods in air. Here, one of the smaller radius rods ($r=0.0809a$) is chosen as the defect site. The vertical dashed line indicates the location of the perfect array. No acceptor modes exist for this structure, even for complete removal of the rod at $r=0$. Increasing the size of the defect rod creates five distinct donor modes, four of which are still within the photonic band gap at the maximum rod radius.
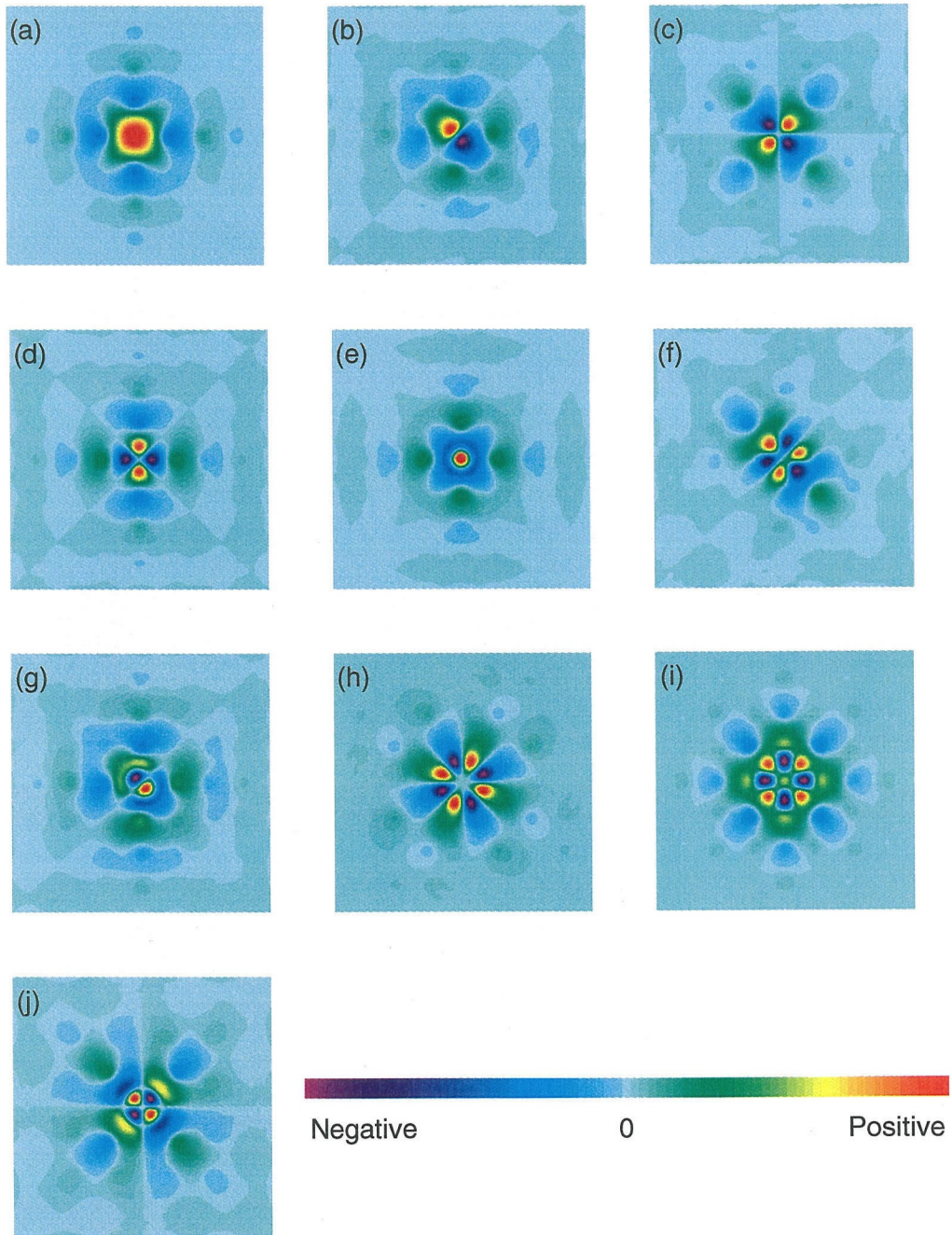
Fig. 4-9. Electric field configurations of the defect modes for the single-rod square structure of rods ($r = 0.2a$) in air. The acceptor mode has a monopole distribution, shown in (a) for $r = 0.075a$. Donor modes are shown in (b) through (j). (b) One dipole field pattern from a pair of degenerate states, $r = 0.3a$. (c) and (d) Non-degenerate quadrupoles, $r = 0.475a$. (e) Second-order monopole, $r = 0.5a$. (f) One of a pair of degenerate hexapoles, $r = 0.525a$. (g) One of a pair of degenerate second-order dipoles, $r = 0.65a$. (h) and (i) Non-degenerate octopoles, $r = 0.8a$. (j) Second-order quadrupole, $r = 0.8a$.

Fig. 4-10. Electric field configurations of the defect modes for the double-rod square structure of rods ($f=0.126$, $\beta=0.3$) in air, with one of the large radius rods as the defect site. Decreasing the rod radius creates an acceptor mode monopole, shown in (a) for $r=0.07a$. Increasing the rod radius gives the donor modes shown in (b) through (g). (b) One dipole field pattern from a pair of degenerate states, $r=0.45a$. (c) and (d) Non-degenerate quadrupoles, $r=0.72a$. (e) Second-order monopole, $r=0.72a$. (f) One of a pair of degenerate hexapoles, $r=0.919a$. (g) One of a pair of degenerate second-order dipoles, $r=0.919a$.
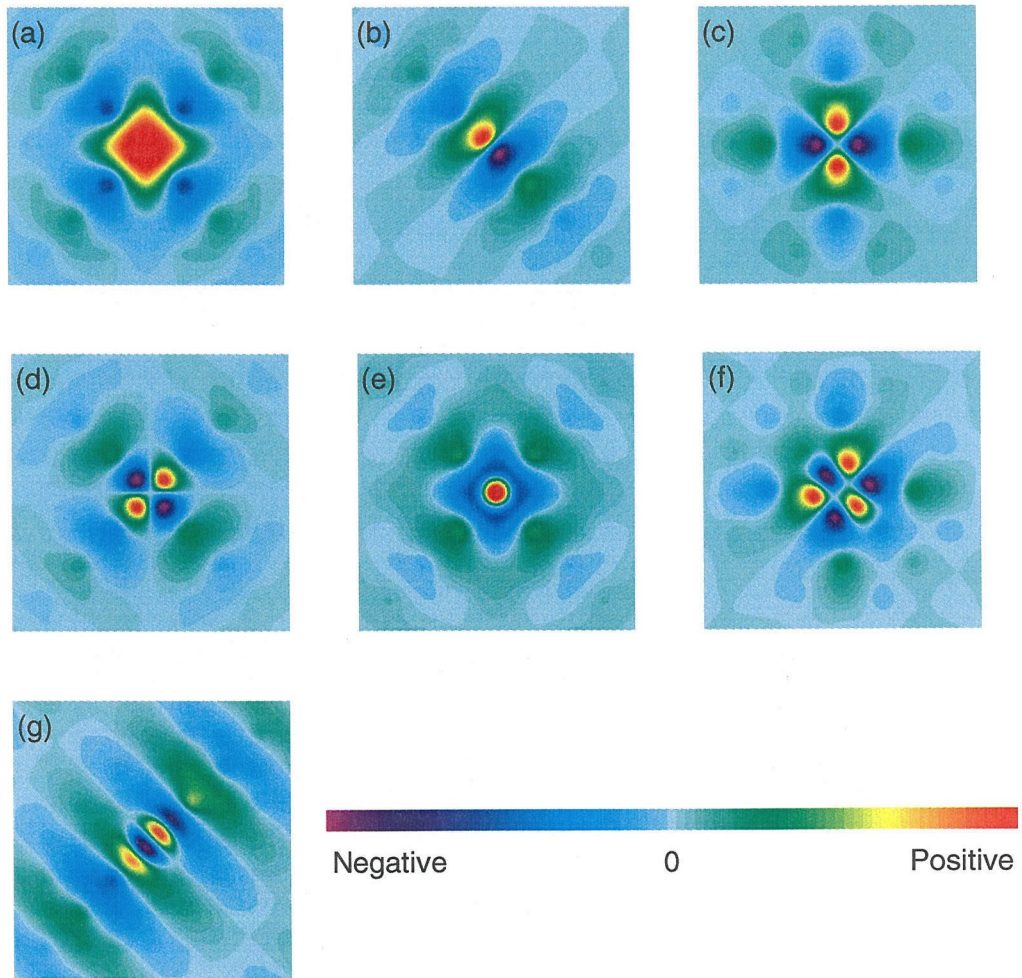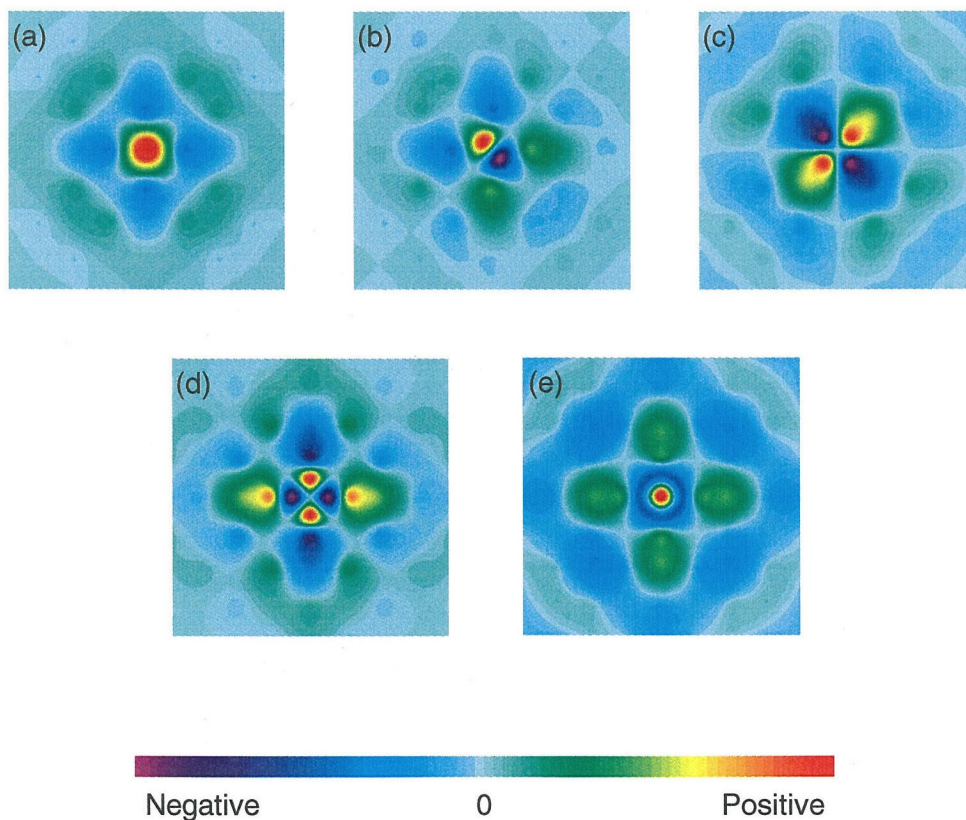
Fig. 4-11. Electric field configurations of the defect modes for the double-rod square structure of rods ($f = 0.126$, $\beta = 0.3$) in air, with one of the small radius rods as the defect site. There are no acceptor modes for this structure—all field distributions shown are donor modes. (a) Monopole, $r = 0.18a$. (b) One of a pair of degenerate dipoles, $r = 0.5a$. (c) Non-degenerate quadrupole, $r = 0.65a$. (d) Non-degenerate quadrupole, $r = 0.73a$. (e) Second-order monopole, $r = 0.73a$.

CHAPTER 5

Hyperthermal Neutral Fluorine Etching of Silicon

Abstract

A hyperthermal neutral fluorine atom beam has been generated by laser-induced detonation of SF_6. The pulsed beam has an ion fraction of much less than 1%, with average translational energies tunable from 4 to 30 eV. The collimated neutral fluorine beam has been used in the anisotropic etching of silicon. Etch profile anomalies including microtrenching and undercutting similar to those found in traditional reactive ion etch processes were observed. The appearance of these phenomena is explained by inelastic scattering of energetic, reactive F atoms. A rough "shag carpet" texture is observed on flat surfaces exposed to the beam at high translational energies. It was discovered that this roughness could be eliminated through the introduction of thermal molecular chlorine to the surface during etching. Silicon etch rates were measured using a sensitive quartz crystal microbalance and found to agree with the etch rates of a photoresist masked silicon wafer measured from SEM pictures. However, the trend of etch rate versus beam energy does not match the $\sqrt{E}$ dependence expected for collision-induced desorption. This is most likely due to a variation of the fluorine beam flux as the energy is varied, resulting in reduced etch rate for higher beam energies.

5.1 Introduction

The properties of photonic crystals discussed in the previous chapters are not restricted to any specific wavelength of light. As long as the elements that form the crystal are large enough so that the system can be described classically, the photonic band gap results are valid. Thus, we can use photonic crystals in applications that range from the microwave regime (millimeters to meters) down to visible light wavelengths (sub-micron device scale). The band gap properties scale such that the size of the photonic crystal elements should be of the order of the wavelength of interest.

Many optoelectronic devices, e.g., semiconductor lasers and light-emitting diodes, that operate at visible to near-infrared (IR) wavelengths could potentially be improved through utilization of photonic crystals. These devices have sizes on the order of microns and are currently made by standard semiconductor microfabrication techniques. Through a series of processing steps involving deposition, masking, and etching, a complex device can be slowly built up on the substrate. If a photonic crystal were to be introduced into the structure of one of these optoelectronic devices, its design should be integrated into the device so that it could be fabricated simultaneously. Thus, it is a reasonable starting point to use common semiconductor materials to form photonic crystals.

Fortunately, semiconductors are an excellent choice for use in microscale photonic crystals. They have reasonably high dielectric constants ($\varepsilon_{Si} \approx 11.8$, $\varepsilon_{GaAs} \approx 13.1$) that provide a large enough dielectric contrast with air to allow photonic band gaps to open. They also have low absorption coefficients in the infrared and near-infrared region of the electromagnetic spectrum so that absorptive losses to the dielectric medium are minimized. Finally, the processing techniques already developed for computer chips may be directly applied in the microfabrication of photonic crystals.

Two-dimensional photonic crystals are especially well suited for fabrication by traditional lithographic techniques. The desired pattern is first defined on the photoresist

and then etched deep into the substrate. Typically, the crystal depth needs to be several times that of the unit cell size in order to minimize the end effects of the rods and promote confinement of the electromagnetic waves within the plane. In addition, the rods should all be straight, smooth, and uniform over the entire depth, as deviations will tend to disrupt the photonic band gap properties and impair the crystal performance. These requirements place great demands on the etching process.

5.1.1 Fabrication Issues

Plasma etching techniques are commonly employed in very large scale integration (VLSI). The plasma is a complex mixture of moieties including ions, electrons, and neutrals (molecules and radicals), with ions and radicals being the main contributors to etching. The positive ions are accelerated through a potential drop across the plasma sheath to bombard the wafer surface. Neutral reactive species from the plasma can also be transported to the wafer surface by diffusion. Directional etching of the surface material occurs through a combination of chemical reaction and momentum transfer from the energetic ions. The interaction of energetic ions with the solid surface is of particular importance in determining the final profiles.

Figure 5.1 illustrates some of the profile irregularities that may appear during etching. The sidewalls might not be perfectly straight, but can become sloped or bowed, as shown in Figs. 5.1(a) and (b), respectively. RIE lag is the phenomenon where narrow trenches are etched slower than wider trenches [Fig. 5-1(c)]. "Microtrenching" (d) describes the appearance of a sharp groove near the foot of the etched feature. Finally, "undercutting" (e) occurs when the material beneath the protective mask is removed. Such profile irregularities can become pronounced in the etching of deep trenches, and may be detrimental to the performance of a photonic crystal.

When the pattern mask is insulating (e.g., photoresist) plasma-induced charging can cause electrostatic deflection of the incoming ions, resulting in some of the

undesirable profile anomalies shown above. The detrimental effects of surface charging can most easily be eliminated altogether by the use of neutral reactive species for etching instead of plasma ions.

5.1.2 Neutral Beam Etching

In the laboratory, we began work on a new kind of etching process that uses a beam of hyperthermal neutral atoms for etching instead of high-energy ionized species. Through the development and study of this novel etching technique, it was our goal to:

(1) Gain a deeper understanding of some of the fundamental processes that occur when reactive species impinge upon semiconductor surfaces,

(2) Develop a technique that might help overcome some of the etching limitations encountered in industrial fabrication processes, and

(3) Use this new process to achieve high aspect ratio etching that could be used to fabricate a two-dimensional photonic crystal.

The hyperthermal neutral atom source provides a unique opportunity to investigate etching phenomena in the absence of charging effects found when plasmas interact with patterned surfaces. Comparison of the results of neutral beam etching with reactive ion etching may help elucidate some of the important mechanisms that direct etch profile evolution.

As silicon is by far the most important semiconductor used in microprocessing today, we have chosen to study the etching of silicon using a hyperthermal neutral beam of fluorine atoms. The source of fluorine in the experiments is sulfur hexafluoride (SF_6), a commonly used source gas for industrial plasma etching. SF_6 was chosen because it is highly stable, non-corrosive, non-toxic, and can yield many fluorine atoms per source molecule.

5.2 Experimental Description

5.2.1 Equipment

A schematic drawing of the hyperthermal neutral atom beam apparatus is shown in Fig. 5-2. The apparatus consists of several ultrahigh vacuum chambers (base pressure approximately 1×10^{-8} Torr) connected by small apertures. The isolated design is intended to confine the bulk of the source beam in the first chamber, selecting only a portion of the beam for contact with the silicon wafer. The design also assists in maintaining low background pressure in the mass spectrometer, located in the fourth chamber.

The hyperthermal neutral fluorine atoms are generated in the first chamber. Pure SF_6 source gas is injected into the vacuum chamber at a pressure of 125 psig by means of a home-built piezoelectric pulsed molecular beam valve.[1] The valve opens by the application of a high voltage pulse (typically 400 to 800 V) to the piezoelectric disk translator, which flexes and retracts the sealing poppet. The applied voltage controls the displacement of the poppet and consequently the time that the valve remains open. The duration of the gas pulse is approximately 300 µs. The SF_6 gas expands supersonically under choked flow into a 10-cm-long water-cooled copper nozzle through a 1 mm diameter orifice at the apex of the cone. The inside surface of the copper nozzle has been plated first with nickel and then a thin layer of bright gold to maximize the surface reflectivity. Shortly after gas injection, a light pulse from a Lumonics model TEA-840 CO_2 laser is fired. The laser light enters the vacuum chamber through a zinc selenide window positioned just beside the nozzle, is reflected and is focused into the cone by means of a gold coated spherical mirror with a 50 cm focal length. The exact timing between the introduction of the source gas and the firing of the laser pulse is precisely controlled to 0.1 µs by a timing circuit. The energy of the intense laser pulse is readily absorbed by the SF_6 gas, as the 10.6 µm emission of the CO_2 laser corresponds to the v_3

vibrational mode of the SF_6 molecule.[2] The intense laser light initiates a high-density plasma which atomizes the gas. As the plasma expands out of the nozzle, electron-ion recombination occurs and a hyperthermal beam of (mostly) neutral atomic fluorine and sulfur atoms emerges. At this point, the expanding species are in the molecular flow regime and no further collisions between particles occur.

Though the atomic beam has been somewhat collimated by the 20° full included angle of the conical nozzle, the angular divergence is further reduced by passing the beam through a 0.5 inch diameter skimmer, located on the flange separating the first and second chambers. The off-axis species are contained within the source chamber and are removed by means of a 3000 ℓ/s cryogenic high vacuum pump. In the second chamber, the beam is either allowed to impinge upon the substrate for etching, or is skimmed further and passed into a double-differentially pumped chamber for detection by a UTI model 100C axial quadrupole mass spectrometer (MS).

5.2.2 Fluorine Beam Analysis

The hyperthermal beam is characterized by tuning the MS to the mass-to-charge ratio (m/e) of interest, and recording the signal as a function of time after the laser pulse is initiated. The resulting time-of-flight (TOF) distribution $N(t)$ is used to calculate the translational energy distribution $P(E)$ of the beam.

A typical TOF curve for fluorine neutrals (filled symbols) is shown in Fig. 5-3(a). Knowing that the fluorine atoms travel 126.5 cm from the nozzle apex to the ionizer of the MS, the translational energy distribution is computed and is shown in Fig. 5-3(b). The fluorine atoms in this beam have an average translational energy of 14.0 eV, with an energy spread of 2.5 eV measured full width at half-maximum (FWHM).

The relative ion content of the beam is determined by comparing the MS TOF signals with the ionizer current turned on versus off. With the ionizing current off only charged species can be focused, mass filtered, and detected by the mass spectrometer.

The measured ion signal for fluorine is shown by the open symbols in Fig. 5-3. The integrated signal with the ionizer off dropped to approximately 4% of the value measured with the ionizer on. The actual ion fraction of the beam is estimated to be significantly lower than the measured 4% for the following reason. Ions are detected with very high efficiency by the MS. Neutral species, however, must undergo ionization in order to become detectable. The ionization process occurs with relatively low efficiency (1 in 10^5) and is further hampered by the small contact time between the fast hyperthermal species and the ionization volume. Therefore, we have concluded that the ion content of the beam is very low.

The translational energy imparted to the fluorine atoms can be controlled by adjusting experimental parameters such as the laser energy and the delay time between introduction of the gas pulse and firing of the laser. Higher laser energies and shorter delay times tend to produce species with higher translational energy. The fluorine translational energy can range from 4 to 30 eV, with a FWHM spread of 10 to 30 percent of the average energy. The more energetic beams tend to have a larger energy spread than the beams of slower species. A sampling of the possible fluorine beam translational energy distributions is shown in Fig. 5-4 along with the calculated energies. The maximum magnitudes for each curve have been normalized to the same value.

The MS was also tuned to detect sulfur ($m/e = 32$) and other higher mass numbers that might exist from incomplete detonation of the SF_6 source gas. The sulfur peak had a similar TOF distribution as for fluorine. From the integrated signals we calculated a fluorine to sulfur ratio of 4:1, lower than the expected theoretical value of 6:1. We suspect that the reason for this difference is that the MS is more sensitive to the higher mass numbers, yielding a relatively larger signal for sulfur. No signal above noise was observed for any SF_x fractions, indicating near complete breakdown of SF_6 into F and S atoms. Previous studies on a similar hyperthermal atom source have also indicated that the SF_6 is more than 99% atomized.[3]

5.3 Experimental Results

5.3.1 Silicon Etch Profile Evolution

Several etching experiments were performed using the hyperthermal neutral fluorine beam. A silicon wafer patterned with photoresist was mounted on a movable stage and placed in the second chamber of the vacuum system. After a hyperthermal fluorine beam with the desired energy has been established and characterized with the MS, the wafer was lowered into the path of the skimmed fluorine beam, 72 cm from the source. In our system, the hyperthermal beam cannot be monitored at the same time etching is occurring because the wafer blocks the beam from entering the mass spectrometer chamber. After the desired number of beam pulses have elapsed, the wafer was raised out of the path of the beam. The hyperthermal beam was checked to ensure that the essential qualities have remained unchanged during the course of the experiment.

We used 80,000 pulses at 2.3 Hz of a hyperthermal fluorine beam with translational energy of 17.6 ± 2.6 eV to etch a masked single-crystal Si wafer. The scanning electron micrographs (SEMs) in Fig. 5-5 show isometric (a) and cross-sectional [(b) and (c)] views of some of the line-and-space structures that were etched. The trench sidewalls are relatively straight, showing a slight slope towards the bottom of the trench. Some microtrenching can be seen next to the sidewalls, a phenomenon that is also observed in plasma etching. The mask remained intact throughout the etching process without any discernible erosion. There was very slight undercutting (etching under the mask) unlike what typically occurs in plasma etching of Si at room temperature with fluorine-based chemistry where the undercutting is more severe. The bottom surface of the etched areas is not smooth, but rather exhibits a "shag carpet" texture that is visible in the SEMs. The microfeatures are approximately 40 nm wide and 100 nm deep. The total etch depth (measured from the bottom of the mask to the top of the shag) is 0.35 μm, corresponding to an etch rate of 44nm/10,000 pulses. Comparison of the etch depth

between the features and in the open area away from masked features in Fig. 5-5(c) shows them to be roughly equal. In fact, the space between the line features appears to be etched slightly deeper, though the shag carpet surface makes accurate comparison difficult. A higher etch rate in between closely spaced features than in open areas is termed "negative lag."

To reduce the rough texture at the bottom of the etched areas, we replaced the pure SF_6 source gas with a mixture of SF_6 and xenon gas. In small amounts, the xenon did not effect the plasma discharge. TOF measurements showed that the hyperthermal Xe atoms had the same velocity as F (and S), but due to its higher molecular mass ($M_{Xe} = 131.3$ versus $M_F = 19.0$) Xe had nearly 7 times the translational energy of F. It was hoped that the additional energy would help to smooth out the surface as etching occurred, thus preventing the microfeatures from forming. Etching experiments with mixtures of 10% and 30% Xe in SF_6 were performed. However, both showed no measurable change in the quality of the bottom surface compared to the etch with SF_6 only.

Next, we modified the experimental system by installing an additional pulsed-operation valve near the wafer position in the second chamber. Thermal chlorine gas at room temperature was pulsed onto the wafer surface, alternating with the hyperthermal fluorine beam pulses using pure SF_6 source gas. The chlorine gas readily dissociates and attaches to the exposed silicon, making the surface more susceptible to etching by the hyperthermal fluorine atoms. The results of an etching experiment on a masked Si wafer with 60,000 pulses of a 16.3 ± 2.0 eV fluorine beam is shown in Fig. 5-6. The improved surface smoothness is readily apparent in all three SEMs. Fig. 5-6(a) shows a peculiar etched surface of alternating rough and smooth stripes. This is a result of the direction from which the chlorine gas was pulsed onto the surface. In order to keep the pulsed valve from blocking the path of the hyperthermal fluorine beam, the valve was placed off to one side. The chlorine pulse was incident upon the wafer surface at an angle, and was

therefore shadowed in places by the masked features. Surface segments in the line-of-sight of the thermal Cl_2 beam were much smoother than areas that are shadowed by the posts, verifying that the addition of chlorine is responsible for the surface smoothing.

Cross-sections of line-and-space patterns are shown in the micrographs in Fig. 5-6(b) and (c). The trench sidewalls have a similar shape as those in Fig. 5-5. The microtrenching at the base of the sidewalls is much more visible now that the shag carpet surface has been smoothed out. The total etch depth is 0.35 μm, the same as the depth of the SF_6 etch with 80,000 pulses. Thus, in addition to smoothing the bottom surface, the presence of chlorine appears to have increased the silicon etch rate to 58 nm/10,000 pulses. The observation is in agreement with a previous study that demonstrated enhanced F-atom etching of Si by the addition of molecular chlorine.[4] Since thermal Cl_2 does not etch Si spontaneously, the sidewalls do not exhibit enhanced undercutting. Comparison of the etch depth in the trench and the open area of Fig. 5-5(c) verifies that a very small amount of negative lag is present.

We used the same combination of hyperthermal fluorine plus thermal chlorine to perform a deep etch and study profile evolution for high aspect ratio etching. A single masked silicon wafer was exposed to 100,000 pulses of a 16.0 ± 1.7 eV hyperthermal F beam and thermal Cl_2, then removed from the chamber and cleaved. One half of the wafer was then etched with an additional 100,000 pulses so that the evolution of the feature profiles could be examined at two different etch depths. Fig. 5-7 shows two SEMs of the wafer surface after 100,000 pulses. As before, the addition of chlorine has helped to smooth the bottom surfaces and prevents the shag carpet from forming. The microtrenches next to the sidewalls are well developed, and some undercutting beneath the protective mask is visible in both SEMs. The sidewalls slope inwards towards the trench bottom as before, but are not perfectly straight; a dislocation in the slope of the sidewall appears approximately halfway down the structure, best seen in Fig. 5-7(b). This abrupt change in the sidewall slope is readily apparent in Fig. 5-8, when the wafer has

been etched with 200,000 pulses. The top portion of the trench profiles all have the same slope, then bend towards the bottom of the trench, then curve in again slightly near the bottom of the trench. We will discuss the reasons for the formation of this unusual phenomenon in a later section. After 200,000 pulses the microtrenches have become very deep, resulting in the appearance of finger-like columns in the center of each etched line. The mask remained in good condition with little alteration even after a large number of pulses. Very slight negative lag is also observed in Fig. 5-8(b). The total etch depth for this experiment was approximately 1.3 μm, corresponding to an etch rate of 65nm/10,000 pulses. The sidewall profiles were undercut by 5%.

5.3.2 Measurement of Etch Rate

The hyperthermal neutral fluorine atom source can be tuned to vary the average translational energy from 4 to 30 eV. As the etching of silicon is both a chemical and a momentum induced process, varying the incident beam energy could have an effect on the rate at which material is removed from the surface.

To study the effects of translational energy on silicon etch rate, we installed a Leybold Inficon model XTM/2 Deposition Monitor into the second chamber of the vacuum system. The monitor is a quartz crystal transducer type deposition (or etch) process monitor and is capable of precisely measuring small changes in mass. The principle of operation is based on the piezoelectric sensitivity of a quartz crystal to mass loading. When a voltage is applied across the faces of a properly cut quartz crystal, the crystal is distorted and changes shape in proportion to the applied voltage. Certain discrete frequencies of applied voltage induce a sharp electro-mechanical resonance in the crystal. When mass is removed from the face of the resonating crystal, the resonant frequency increases. The change in frequency is very reproducible and can be directly related to the removal of mass from the crystal surface. Using the material density and

area of the crystal, the calculated change in mass can be converted to a change in thickness, the etch depth.

A thin layer (approximately 1 µm) of silicon has been deposited onto the surface of a quartz crystal resonator. The crystal was placed inside the temperature controlled rate monitor and installed in the vacuum chamber. The hyperthermal neutral fluorine beam was started, and the TOF distribution was measured with the MS to allow for calculation of the beam energy. The silicon covered quartz crystal is then lowered into the path of the beam and the fluorine begins to etch the silicon layer. The crystal resonant frequency is monitored for 10 to 20 minutes to establish an average etch rate. The crystal is then pulled out of the path of the beam and the delay between the gas and laser pulses is changed to establish a new beam energy. The process is repeated for a range of fluorine energies from 10 to 24 eV, the prime operating regime of the hyperthermal source.

The etch rate versus average translational fluorine atom energy for two experimental runs is plotted in Fig. 5-9. Though there is some scatter in the data, it appears that the highest etch rate occurs for an average fluorine energy of 15 eV. The etch rates calculated for the silicon coated quartz crystal resonator are slightly higher than those found for etching of the masked silicon wafers. The presence of a thicker layer of SiO_2 on the surface of the masked wafers, which has a slower etch rate than Si, would explain this result.

From the quartz crystal data, it appears that the etch rate *decreases* for beam energies greater than ≈ 17 eV, much different than the $\sqrt{E}$ dependence expected for collision-induced desorption. This unexpected result is most likely due to a decrease in the neutral fluorine flux at higher energies. The higher energy species were obtained by lessening the delay time between the introduction of the gas pulse into the copper nozzle and the firing of the laser. Thus, the laser light interacts more with the leading edge of the incoming gas pulse compared with beams at longer delays (lower energy). The gas

pulse profile does not have as much time to develop inside the cone before the plasma is ignited by the laser, effectively reducing the amount of source gas in the plasma discharge. As etch rate is expected to depend linearly on flux, the reduced plasma gas density will produce a lower etch rate for these higher energy atom beams. We expect the same to be true for very long laser delay times as well (which yields low energy beams). In this case, the source gas pulse is well developed and has likely begun to dissipate into the chamber when the laser light pulse arrives at the nozzle, resulting in a lower density plasma discharge.

Attempts to remove the effect of flux variation from the etch rate measurements were unsuccessful due to difficulties in measuring the flux of neutral species. Figure 5-10 shows the total number of counts detected by the mass spectrometer at $m/e = 19$ when the ionizing current is turned on ("neutrals") and off ("ions"). The flux of neutrals appears to reach a maximum when the translational energy of the beam is 14 eV. As the beam energy increases further, the flux drops off and then abruptly increases again. The ion flux, on the other hand, is negligible at energies less than 12 eV but sharply rises at higher energies. We believe that the reduced plasma density at short delay times inhibits efficient recombination of electrons and ions to yield neutral atoms, resulting in the increased ion signal. Comparison of the two curves suggests that the apparent neutral flux increase at high beam energies is due to the presence of these ions. Though the ion content may only be slightly increased, the efficiency with which these ions are detected in the MS is much greater than for neutrals, masking the measurement of true fluorine flux.

5.4 Discussion

The creation of an active fluorine atom source that is both directional and neutral allows us to investigate the evolution of etch profiles in the absence of charging effects,

present when etching in plasmas. This permits the unambiguous determination of the role of inelastic scattering on profile evolution.

For all etching runs performed, microtrenches were seen to appear at the foot of each etched feature. A model of atom-surface interaction dynamics has shown that direct inelastic scattering (DIS), a single atom-surface collision process, is solely responsible for microtrenching.[5] As the profile of a trench begins to evolve, the steepest slope is located at the edges of the feature. Hyperthermal F atoms that impinge upon this portion of the feature strike the surface at an oblique angle and are likely to be scattered in the forward direction, retaining a significant portion of their original energy. In this manner, the flux of high energy fluorine atoms is larger at the sidewall feet than in the center of the trench causing a larger etch rate at those locations. Once the microtrench begins to form, forward scattering by DIS is further enhanced by the presence of steep sidewalls on both sides of the microtrench. Thus, the feature becomes more and more pronounced as etching continues.

The same scattering mechanism is believed to be responsible for the shag-carpet microroughness seen for the hyperthermal fluorine etch chemistry. Microscopically corrugated surfaces, such as those of the rough fluorosilyl layer, are the origin of this phenomenon. When large angles of incidence are encountered, DIS increases resulting in nanotrench formation and an even greater surface roughness. Thus, a macroscopically flat Si surface is unstable to etching by directed hyperthermal neutral F atoms. A similar shag-carpet phenomenon has been found to occur when polymer surfaces on the Space Shuttle are exposed to the static atomic oxygen atmosphere at low earth orbits.[6] The motion of the Shuttle is equivalent to its surfaces being bombarded by 5 eV reactive oxygen atoms. This similarity further suggests that the microstructure formation is a function of etching with low energy neutral beams.

An inadequate supply of reactive fluorine atoms to the Si surface impedes etching of the protruding entities, allowing for DIS to occur. The addition of thermal molecular

chlorine to the surface helps smooth out the etched surfaces by supplying an additional flux of reactive species to the surface. At room temperature, molecular chlorine dissociatively chemisorbs onto the first few atomic layers of the silicon surface.[7] Any dangling silicon bonds are now saturated, making the top surface layers more susceptible to etching by incoming hyperthermal F atoms.

The discontinuous slope of the sidewalls observed in the deep etching experiment is also the result of the DIS process. The origin of this phenomenon is explained with the help of the schematic drawings in Fig. 5-11. The microtrench begins to form as an extension of the feature sidewall. As etching proceeds and the microtrench deepens, the sidewall begins to curve more and more inwards (a). Hyperthermal F atoms now strike the sidewall at a decreased incident angle, resulting in broader forward scattering. Thus, more scattered energetic atoms begin to reach the upper part of the inner sidewall of the microtrench where they etch, thereby decreasing its steep slope (b). The result of this interaction is that direct scattering of the main incident beam at the inner trench wall increases, causing additional flux to arrive at near normal incidence to the outer wall (c). This contributes to etching of the outer sidewall thus causing a break in the continuity of its slope. As etching continues, the inner sidewall is etched away by the main incident beam; the scattered flux that maintained its slope no longer reaches the outer wall but instead is directed toward the bottom of the microtrench (d). Thus, it is now possible for the cycle to begin again as the slope of the outer sidewall begins to curve. Continued etching may result in an oscillation of the sidewall slope, as was observed in Fig. 5-8.

Though we have thus far only discussed DIS in detail, two other types of scattering processes are also possible: a) Indirect inelastic scattering (IIS), which involves multiple atom-surface collisions, yielding an atom that possesses a small fraction of the original incident energy but a complete loss of "memory" of the incident angle; b) Trapping desorption (TD), which refers to atoms that leave the silicon surface with thermal energies, having no correlation to the initial energy and angle of incidence.

These two processes scatter reactive fluorine species in a cosine distribution about the surface normal, and together are responsible for the observed undercutting of the mask.[5] Fluorine atoms scattered by IIS, having a higher energy than the TD species, contribute more to the isotropic sidewall etching and undercutting. These species can undergo multiple scattering events within the trench, eventually impinging on the bottom surface again and contributing to the etch rate. In contrast, species scattered in open areas are lost from the surface. This difference accounts for the slight negative lag seen in the SEMs.

The ideal etch profile is one with perfectly straight, vertical sidewalls, no mask undercutting, and a flat surface at the trench bottom. There are several ways in which one might adjust the etching conditions to improve the quality of the etched profiles. Increasing the average energy of the fluorine neutrals should increase the probability of reaction at first impact with the surface, reducing the amount of forward scattering. This explains why effects such as microtrenching are not observed when etching at higher energies (>50 eV). In addition, the increased reactivity of the higher translational energy F atoms at the bottom of the trench results in a smaller flux of scattered non-reacted F atoms to the sidewalls, thereby improving anisotropy. Alternatively, the incident beam translational energy can be tailored so that scattered species have energies below threshold for reaction. This could be aided by lowering the temperature of the silicon wafer so that the energy of the scattered species is not enough to facilitate reaction at the sidewalls. Another solution is to raise the energy necessary for fluorine atoms to react with the substrate. This could be achieved by adding a small amount of oxygen to the etch mixture, which would form a thin layer of siliconoxyfluorides (SiO_xF_y) on the exposed etching surface. As SiO_xF_y has a higher threshold for etching than does SiF_y, the hyperthermal fluorine atoms directly striking the bottom surface could be selected so that they have a high enough energy to etch, but indirectly scattered species would not react at the sidewalls.

5.5 Conclusions

We have shown that a hyperthermal neutral fluorine atom beam, produced from the plasma formed by laser excitation of SF_6, can be used for anisotropic etching of silicon. Etch rates are fairly low (approximately 1 nm per minute) mostly due to low fluorine flux far away from the expanding beam source and low pulse rate. Accurate measurement of the neutral flux at varying F energies using the mass spectrometer was difficult as detection of the small fraction of ions present in the beam overshadowed the neutrals. Without this flux calibration, significant variation of the F atom flux with beam energy will result in anomalous measurements of etch rate. Since the MS is inherently more sensitive to ions than neutrals, the ions should be removed from the beam in order to improve the accuracy of the flux measurement. This can be achieved by deflecting the ions with a charged plate prior to entering the MS. Alternatively, methods specifically developed for the measurement of neutral fluxes such as a torsion balance,[8] can be employed.

The hyperthermal neutral fluorine source provides a unique opportunity to study the interactions of neutral species and surfaces during etching. Though profile anomalies due to charging effects have been avoided, scattering of energetic species was shown to have a significant effect on the development of etch profiles, particularly for deep etching. The severe microtrenching and sloped sidewalls observed would likely impair the properties of a photonic crystal fabricated by this technique. Understanding the consequences of scattering is important so that the adverse effects on profile development can be minimized.

5.6 References

[1] D. Proch and T. Trickl, "A High-Intensity Multi-Purpose Piezoelectric Pulsed Molecular Beam Source," *Rev. Sci. Instrum.* **60**, 713 (1989).

[2] *Multiple-Photon Excitation and Dissociation of Polyatomic Molecules*, edited by C. D. Cantrell, Springer-Verlag, New York (1986).

[3] K. P. Giapis, T. A. Moore, and T. K. Minton, "Hyperthermal Neutral Beam Etching," *J. Vac. Sci. Technol. A* **13**, 959 (1995).

[4] J. W. Coburn, "Chlorine-Enhanced F-Atom Etching of Silicon," *J. Vac. Sci. Technol. A* **12**, 617 (1994).

[5] G. S. Hwang, C. M. Anderson, M. J. Gordon, T. K. Minton, and K. P. Giapis, "Gas-Surface Dynamics and Profile Evolution During Etching of Silicon," *Phys. Rev. Lett.* **77**, 3049 (1996).

[6] B. A. Banks, M. J. Mirtich, S. K. Rutledge, and D. M. Swec, *NASA Tech. Memo.* TM-83706 (1984).

[7] W. Sesselmann, E. Hudeczek, and F. Bachmann, "Reaction of Silicon With Chlorine and Ultraviolet Laser Induced Chemical Etching Mechanisms," *J. Vac. Sci. Tech. B* **7**, 1284 (1989).

[8] S. R. Cook, M. A. Hoffbauer, J. B. Cross, H. Wellenstein, and M. Fink, "A Specialized Torsion Balance Designed to Measure the Absolute Flux Density of Hyperthermal Molecular Beams Containing Reactive Species," *Rev. Sci. Instrum.* **67**, 1781 (1996).
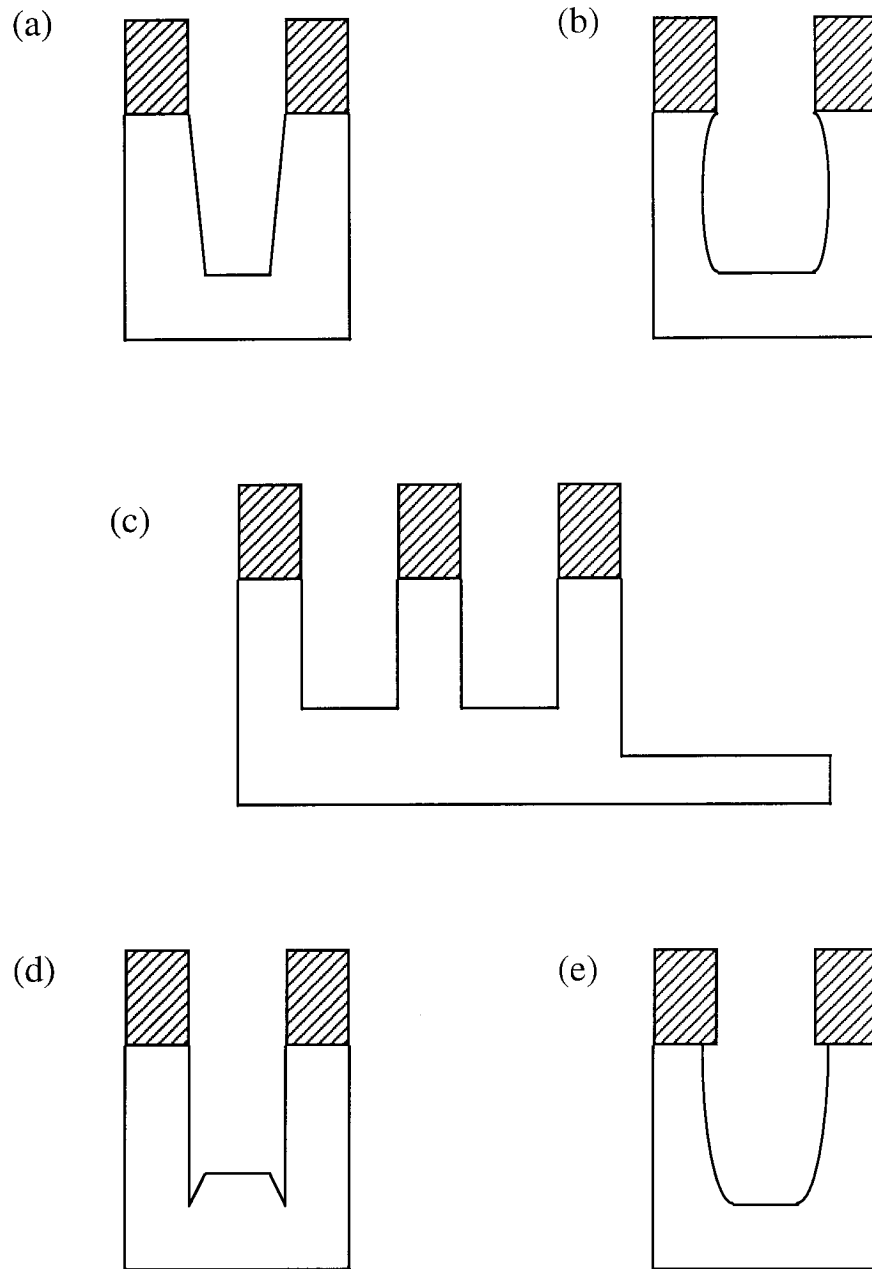
Fig. 5-1. Schematic drawings illustrating possible plasma etching profile anomalies. The hatched regions represent the photoresist that defines the pattern for the substrate below. (a) Sloped sidewalls. (b) Bowed sidewalls. (c) RIE lag. (d) Microtrenching. (e) Undercutting.
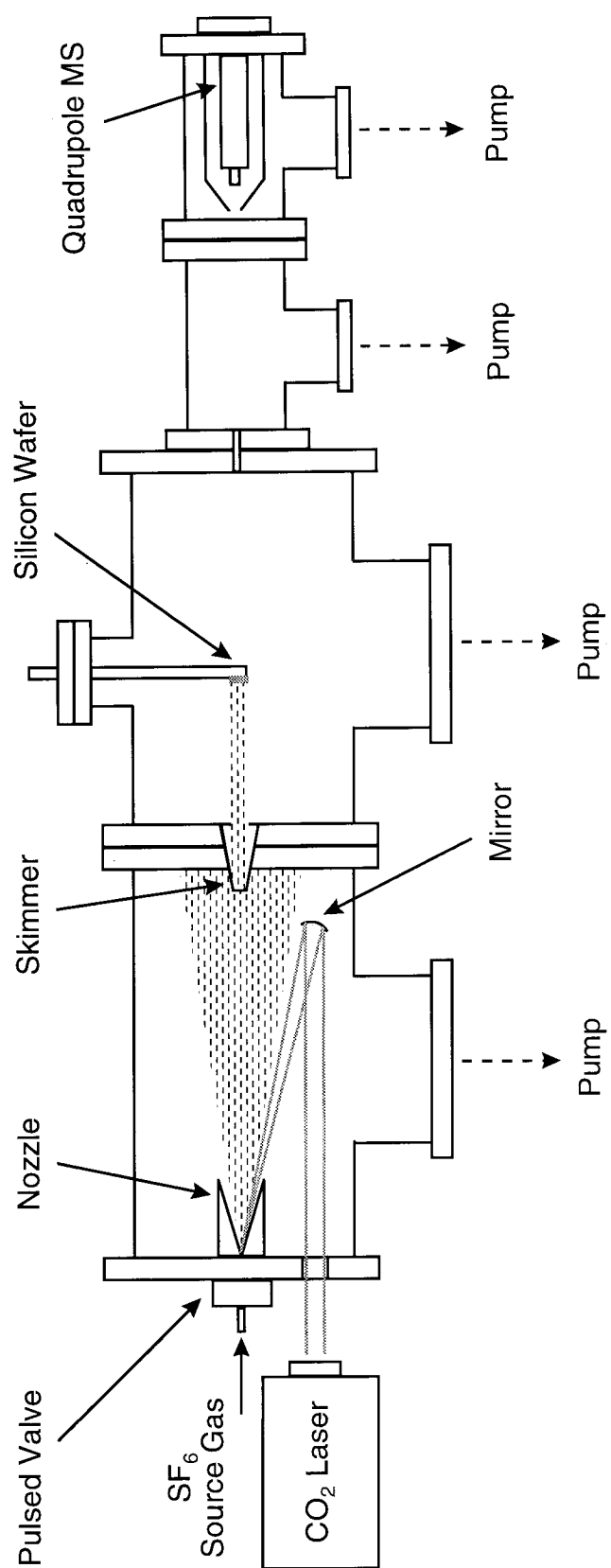
Fig. 5-2. Schematic drawing of the vacuum chamber used for hyperthermal neutral beam etching.
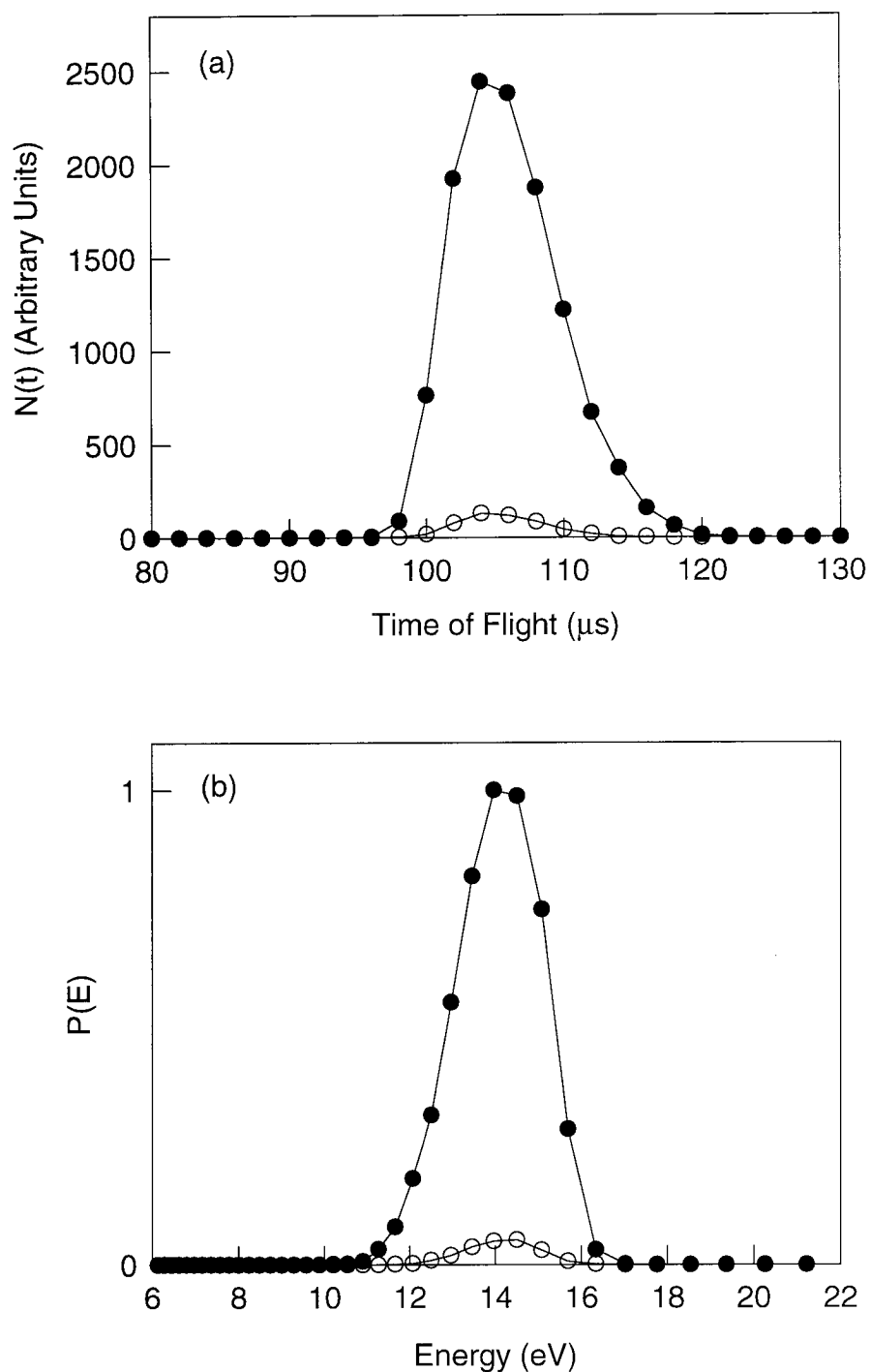
Fig. 5-3. Time-of-flight distribution (a) and the corresponding translational energy distribution (b) for fluorine atoms ($m/e = 19$). The integrated signal for ions, measured with the ionization current turned off (open circles), is 4% of the signal with the ionization current on (filled circles). The beam has an average translational energy of 14.0 eV, with an energy spread of 2.5 eV.
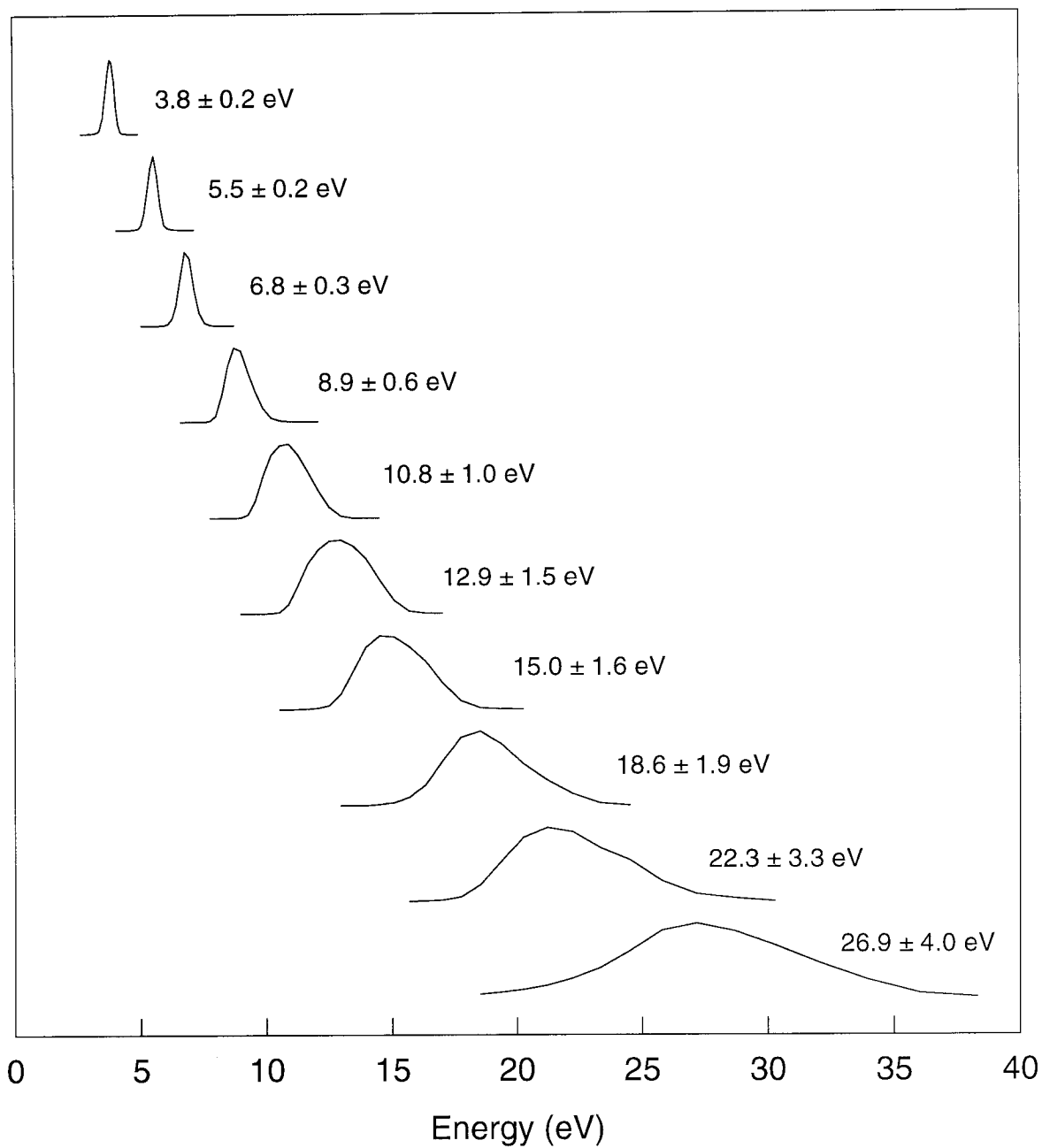
Fig. 5-4. Translational energy distributions for several hyperthermal neutral fluorine atom beams, showing the range of possible energies. The average translational energy is indicated beside each distribution. The magnitude of each curve has been normalized to the same value.
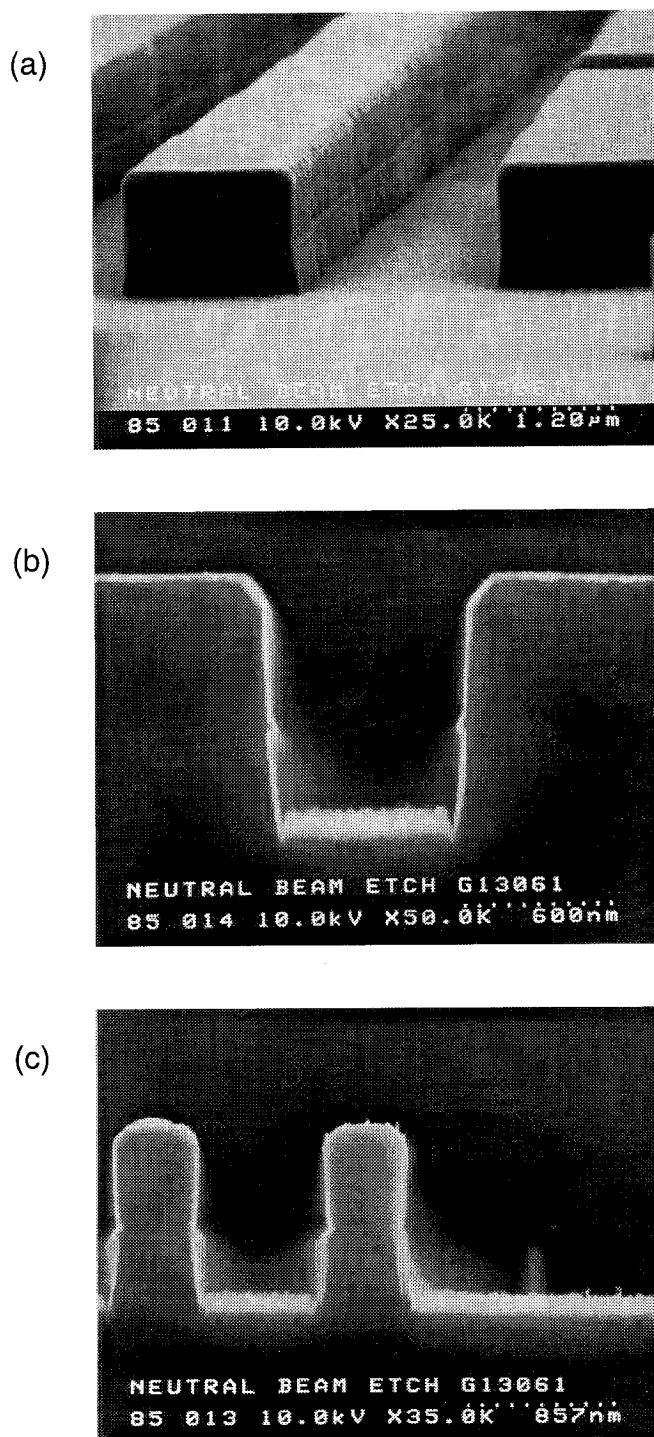
Fig. 5-5. Scanning electron micrographs of the trenches etched in silicon to a depth of 0.35 μm by the hyperthermal neutral fluorine beam. The microtrenching phenomenon is clearly seen in the cross-sectional view in (b), and the rough "shag carpet" bottom surface is visible in (b) and (c).
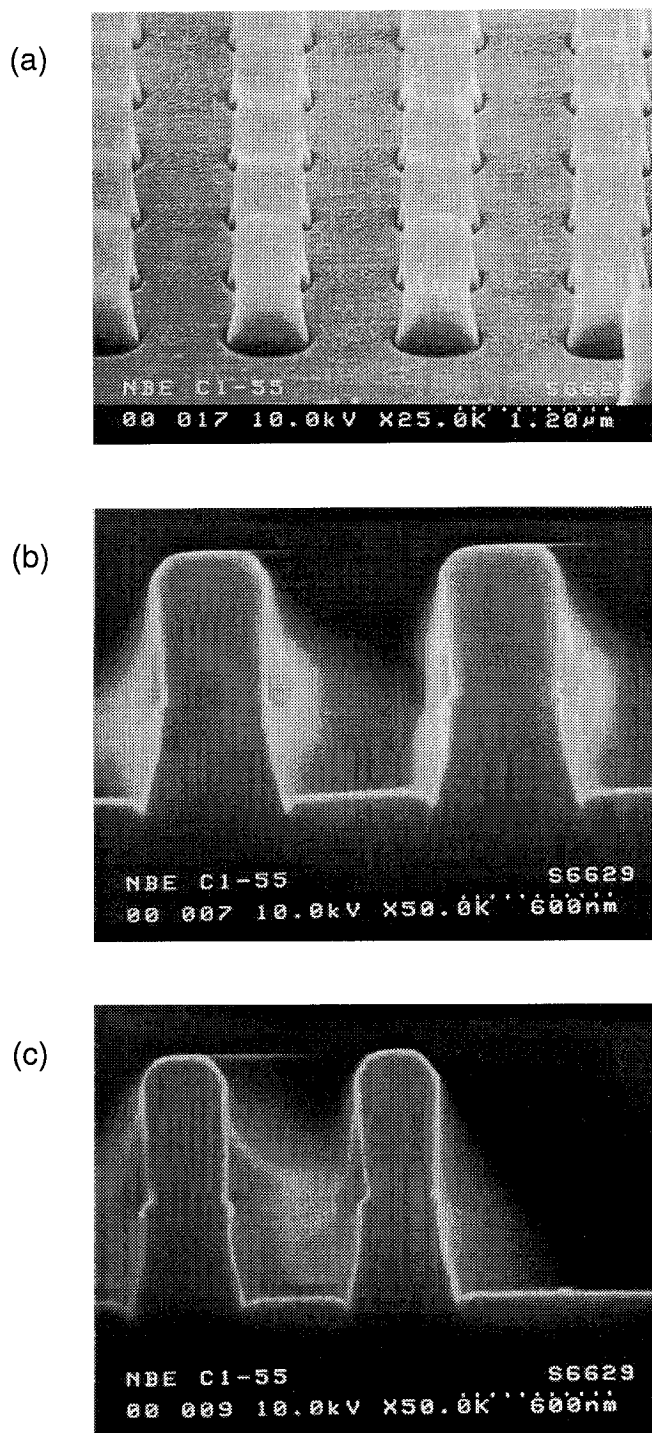
Fig. 5-6. Scanning electron micrographs of silicon etched by the hyperthermal neutral fluorine beam with the addition of thermal molecular chlorine during etching. The chlorine creates a significantly smoother surface than for hyperthermal F etching alone. The striped surface in (a) is due to shadowing of the surface by the posts. Microtrenching is visible at the foot of the sidewalls. The etch depth is 0.35 μm.
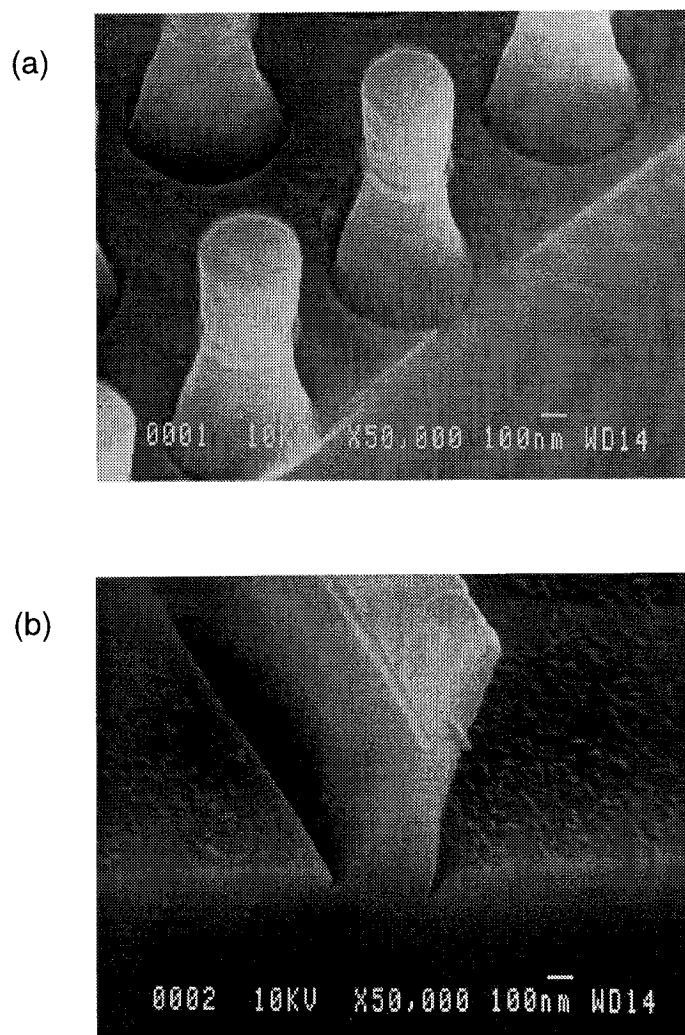
(a)

(b)

Fig. 5-7. Scanning electron micrographs of silicon etched with 100,000 pulses of the hyperthermal neutral fluorine beam plus thermal molecular chlorine. The microtrenching phenomenon is quite pronounced. A break in the sidewall slope can be seen in (b), approximately midway up the feature. Some undercutting of the mask is also visible.

(a)

0006 10KU X27,000 1Pm WD 9
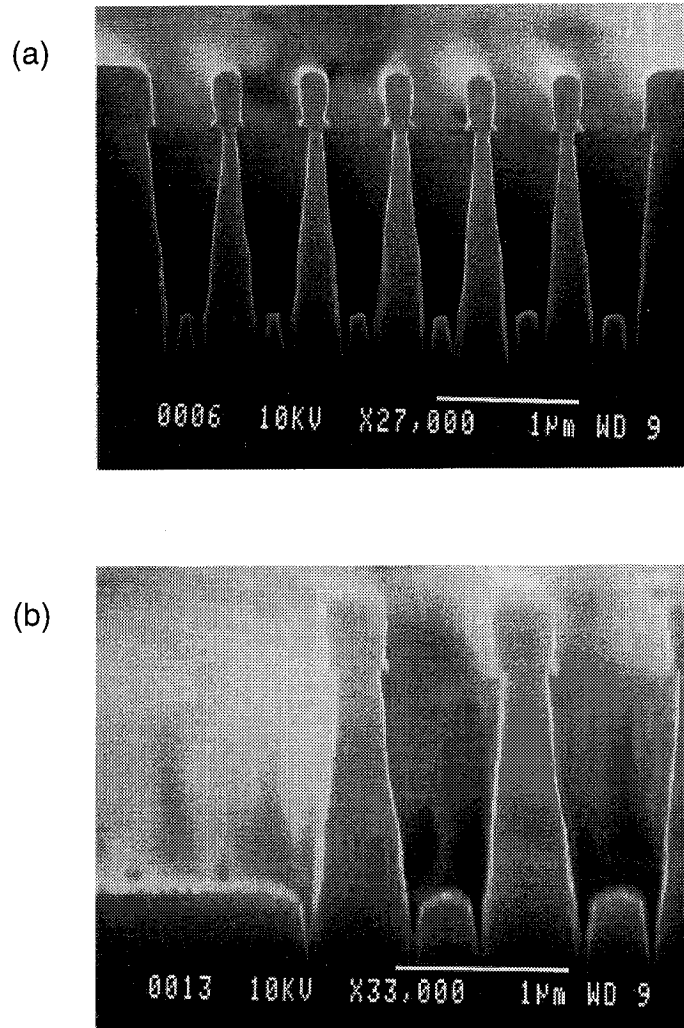

(b)

0013 10KU X33,000 1Pm WD 9

Fig. 5-8. Scanning electron micrographs of silicon etched with a total of 200,000 pulses of the hyperthermal neutral fluorine beam plus thermal molecular chlorine. The total etch depth is 1.3 µm, with 5% undercutting of the mask. The deep microtrenches have produced finger-like columns in the middle of each trench. A break in the sidewall slope is seen approximately halfway down each trench, becoming steeper towards the bottom.
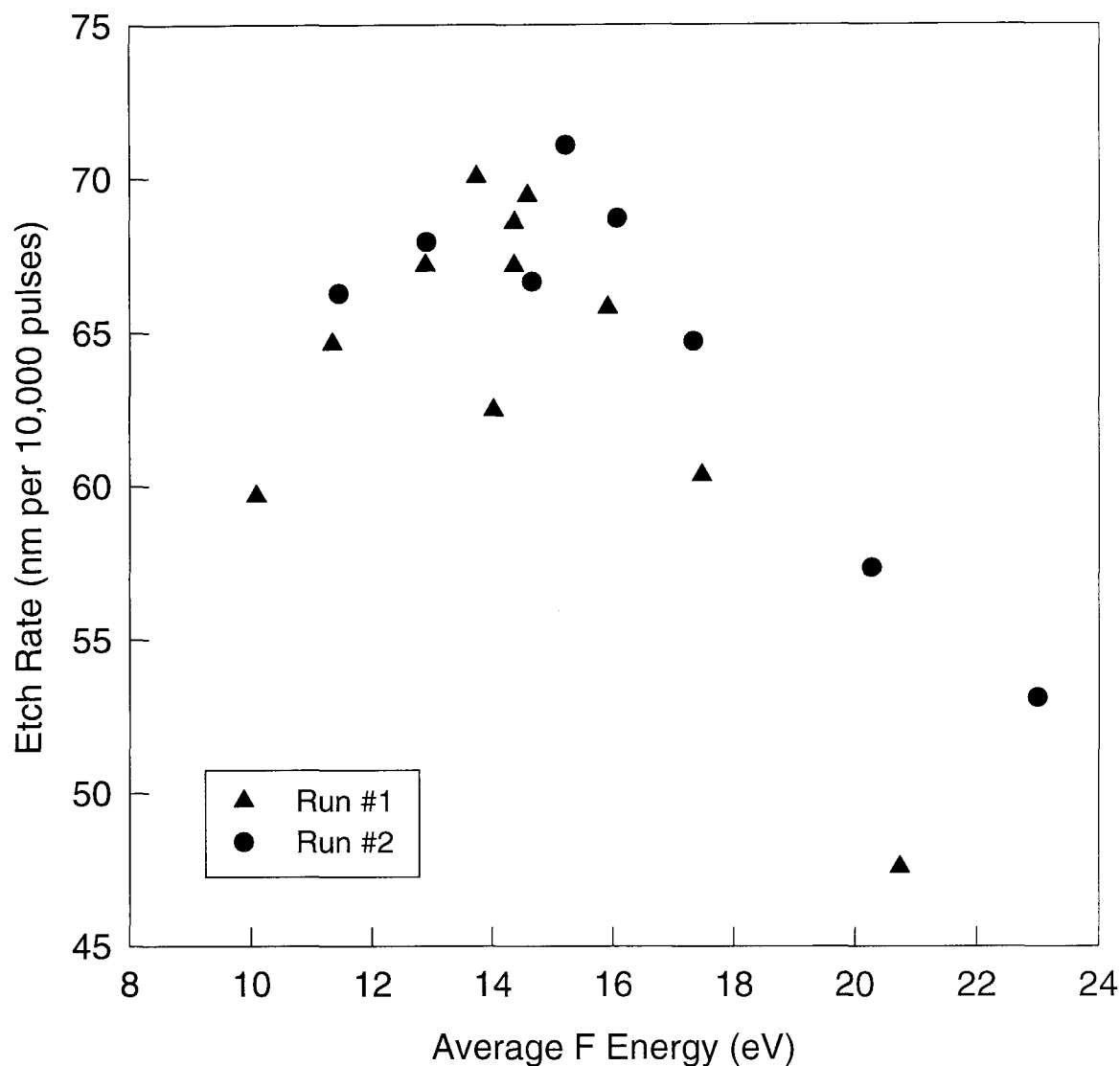
Fig. 5-9. The silicon etch rate as a function of the average translational energy of the hyperthermal fluorine atom beam, as measured with a silicon-coated quartz crystal microbalance. The etch rate is maximum for beams with F atom energies of approximately 15 eV, and appears to decrease for energies greater than 17 eV. The trend is likely caused by reduced fluorine atom flux at high beam energies.
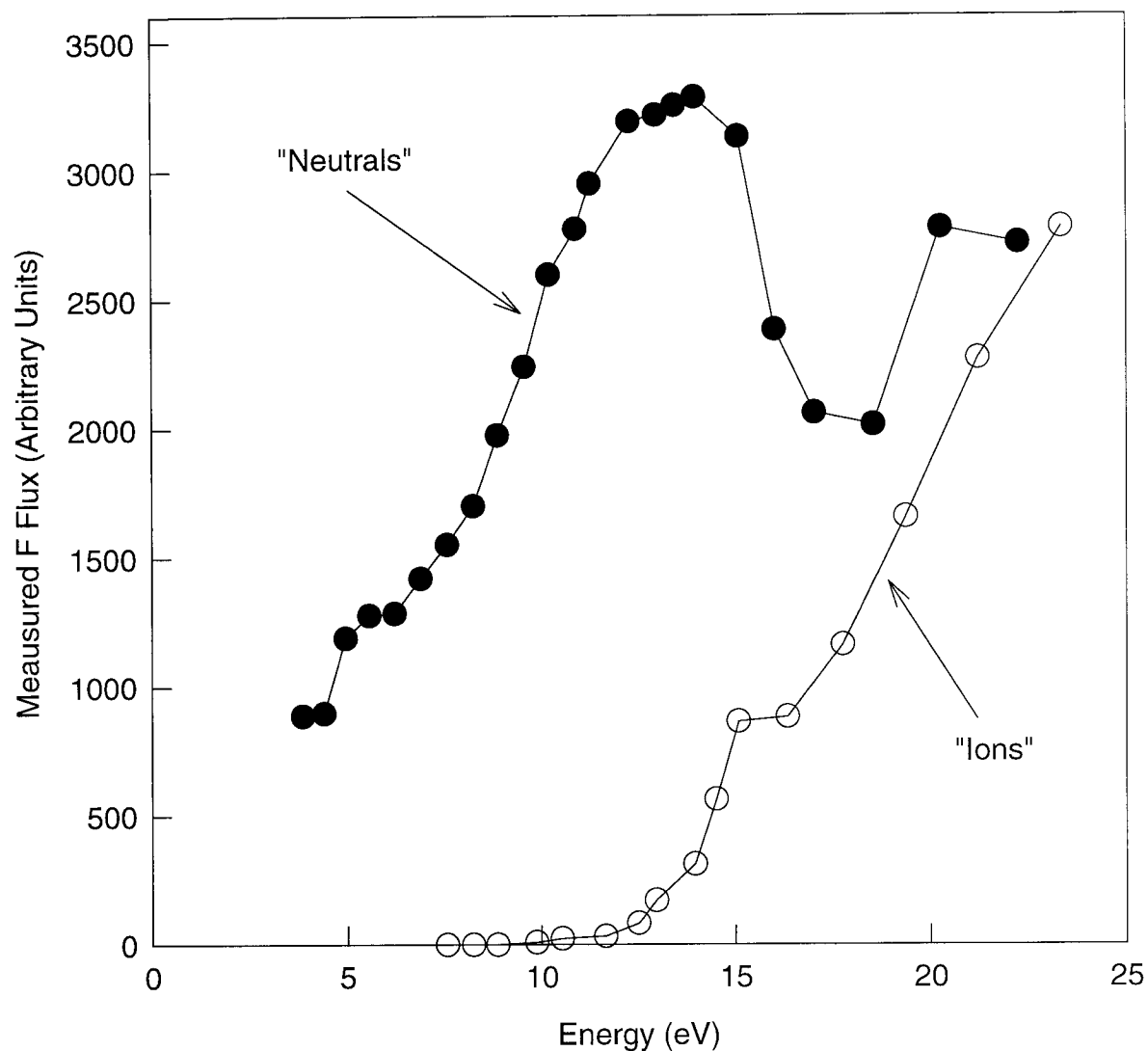
Fig. 5-10. Fluorine ($m/e = 19$) flux as a function of the translational energy of the beam as measured by the mass spectrometer with the ionizing current turned on (neutrals) and off (ions). The apparent increase in neutral flux at energies greater than 18 eV is due to the increased ion content in the beam.
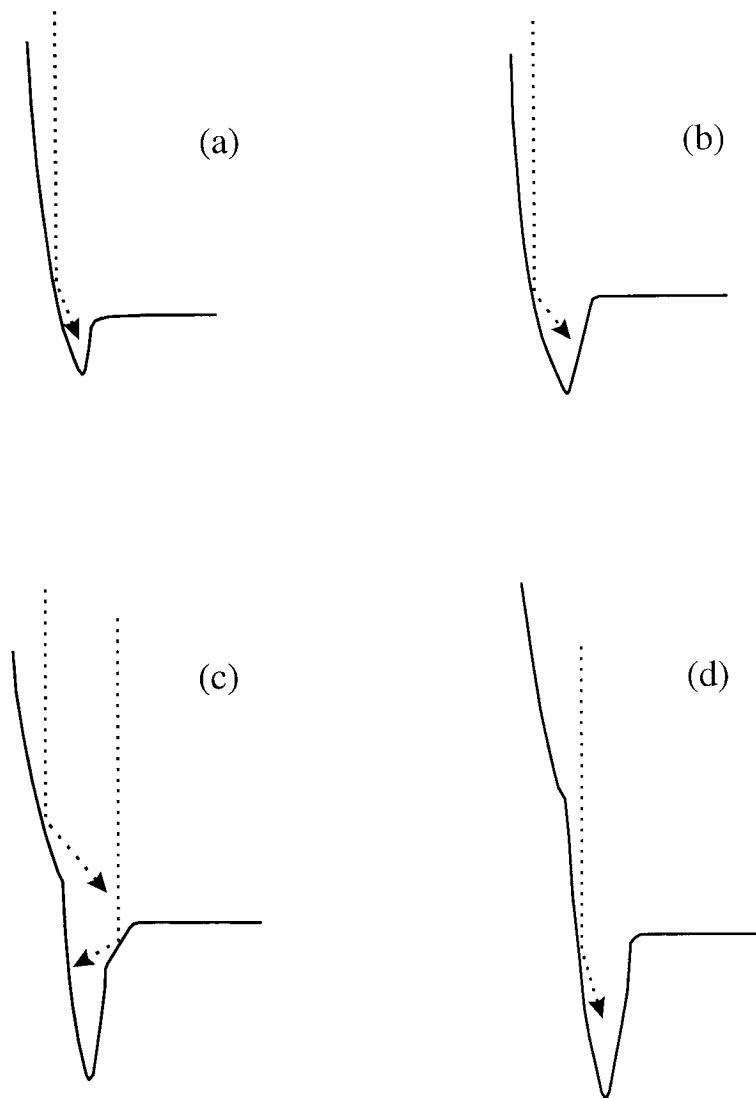
Fig. 5-11. Schematic depiction of the sequence of scattering events that result in a discontinuity in the slope of the profile sidewall.

CHAPTER 6

Conclusions and Future Work

6.1 Conclusions

Photonic crystals provide the opportunity to control and manipulate electromagnetic waves within the range of frequencies of the photonic band gap. This unique property offers promise for improved operation of existing optoelectronic devices including semiconductor lasers and light-emitting diodes, as well as the development of novel optical devices such as filters, switches, and interconnects. Although 3D crystals may be especially valuable because of their ability to control waves in all directions of propagation, 2D structures also find several important uses as a result of their strong reflective properties within the plane of the photonic crystal. In both cases, the useful properties for applications are enhanced by the presence of a wide forbidden frequency range, and thus we seek crystal structures that possess the largest photonic band gaps possible.

To achieve this goal, theoretical methods for calculating the frequency band properties of photonic crystal structures have been developed. Though these methods are a great improvement over the alternative—a "cut and try" experimental approach—the search for the best structures is a difficult task in view of the wide range of variational parameters to model (e.g., lattice type, filling fraction, shape of filling elements, dielectric contrast). The overwhelming number of possible geometrical arrangements even for 2D crystals suggests the need for a rational approach toward selecting the most promising structures for study. Symmetry analysis of the crystal lattice and filling elements can serve as a guide through the vast domain of possible structures, aiding in the discovery of

those with large photonic band gaps that are also relatively easy to microfabricate. In addition, symmetry principles can be used as a way to increase the band gap width in some crystals known to possess large photonic band gaps.

Using a symmetry analysis approach, we have investigated a variety of two-dimensional photonic crystal structures. First, consider the crystals formed when the rods contain the low dielectric constant material and are surrounded by a high dielectric constant background. For this case, both the square and triangular lattice structures have absolute band gaps when the filling fractions are near the close-packed condition. The size of the absolute photonic band gap in the single-rod square lattice can be significantly increased by introducing another rod with a different diameter into the unit cell. The band gap of this double-rod square lattice is nearly three times the size of the best single-rod lattice band gap at the same dielectric contrast. Still, the single-rod triangular structure has the largest photonic band gap (in wavelength) of all the 2D structures of holes in dielectric, and is only made smaller by reducing the lattice symmetry or by the addition of more scattering elements into the unit cell. Comparison of the symmetry properties of these structures suggests that the most favored arrangement for structures with the low dielectric constant material in the rods is that with the highest symmetry possible. Specifically, this is the *p6mm* based structure with circular cross-section holes.

The greatest disadvantage of utilizing the absolute band gaps of these crystals is that the largest gaps occur at high rod filling fractions, resulting in thin-walled structures that are difficult to microfabricate. This problem may be avoided by instead using the complementary crystal arrangement, fabricating photonic crystals that have the high dielectric constant in the rods surrounded by air. However, no absolute photonic band gaps exist for either the single-rod or double-rod square lattice structures, or the triangular lattice of dielectric rods in air. Thus, by merely switching the placement of the dielectric materials in the crystal, the photonic band gap properties have been greatly affected. Analysis of the crystal symmetry properties can guide the way towards finding new

geometric arrangements that will optimize the photonic band gap width for crystals of dielectric rods in air.

For crystals with a square lattice basis, large absolute band gaps can be obtained by reducing the lattice symmetry. Removing the mirror planes of the single-rod square geometry through the introduction of the glide symmetry operation was found to lift band degeneracies and open substantial band gaps at moderate filling fractions. The triangular lattice structures were also found to benefit from symmetry reduction, for example by lowering the rod symmetry from *6mm* to *3m.* to create the honeycomb lattice structure. The optimal arrangement, the reduced symmetry triangular structure, has a blend of *6mm* and *3m.* symmetry elements which combine to form a crystal with the largest absolute photonic band gap found for 2D structures of dielectric rods in air. However, the small features within this crystal structure (in this case, small diameter rods) may again lead to problems in microfabrication. Thus, it may be advantageous to sacrifice some of the photonic gap width in exchange for manufacturing robustness by reverting to the honeycomb structure. Here, the photonic gap is slightly more narrow but the crystal structure does not contain any exceptionally small features, making it much better suited to microfabrication.

Though perfect photonic crystals are valuable in applications where complete reflection of waves within the band gap is desired, the introduction of a physical defect into the crystal can be used to create a strongly localized electromagnetic mode with specific properties. The frequencies and symmetry properties of these defect modes can be controlled by choosing the appropriate size of the defect, and may be useful in devices to direct energy in and out of the crystal. For crystals that contain more than one type of scattering element, the choice of which element to use as the defect site gives even greater flexibility to precisely tune the defect mode properties.

In addition to theoretical calculations, we have developed a novel dry-etching technique that can be used in the microfabrication of photonic crystal structures. A

hyperthermal neutral fluorine atom beam, produced from the plasma formed by laser excitation of SF_6, was used for anisotropic etching of silicon. The advantage of using neutral species for etching is that problems in etch profile evolution caused by charging of the wafer surface are avoided. However, scattering of reactive species was found to play a significant role in the development of the feature profiles, causing the formation of sloped sidewalls, deep microtrenches, and some undercutting of the mask. These anomalies were present to the extent that an attempt to microfabricate a photonic crystal with features on a sub-micron size scale would be greatly hindered. In order to etch such a crystal using this hyperthermal fluorine source, it would be imperative to reduce the effects of the reactive scattered species, perhaps by changing the etch chemistry or lowering the reactivity of the sidewalls through cooling. In the event that this does not sufficiently improve the etched profiles, other etching techniques such as RIE or high-density plasmas might be sought as a way to achieve the good profiles with high-aspect ratio necessary for 2D photonic crystals.

6.2 Future Work

With the presentation of the work in this thesis, the theoretical investigation of perfect 2D photonic crystal structures is somewhat complete. The focus of future work should now shift towards the issues that *real* structures present. For example, the results for the structures described here assumed infinitely long rods, which for practical purposes implies that the rod length is many times longer than the lattice constant ($L \gg a$). The reality of photonic crystal fabrication is that the rods often do not meet this requirement, and the truncated rods can affect the performance of the crystal. Also, for applications where it is desirable to couple light out of the crystal structure in the direction normal to the crystal plane, the effects of the ends of the rods cannot be neglected. These considerations suggest the need for fully three-dimensional modeling of

2D crystals. Band frequency calculations alone cannot capture all of the relevant phenomena that exist for truncated crystals. Calculation methods such as finite-difference time-domain solution of the Maxwell equations are well-suited to describe truncated structures, and can yield information about the electromagnetic waves both inside and outside the crystal structure.[1,2] Thus, this method can also be used to gain an understanding of the scattered electromagnetic wave patterns. This is particularly useful when designing photonic crystals for device applications where the 2D crystal is used in place of a 1D Bragg reflector mirror. The reflected radiation from photonic crystals seems to concentrate along the principal lattice axes,[3] a much different pattern than waves reflected from a dielectric mirror. The use of crystals without mirror planes, such as the glide-symmetry square structure, might provide a more even spatial distribution of reflected waves, offering an improvement over square or triangular lattice structures.

The supercell approach is a convenient method for calculating the defect mode properties of photonic crystals. The drawback is that a very large amount of computer memory is required to retain a sufficient number of plane wave expansion terms to yield accurate results. The errors introduced by carrying too few plane waves are small for the lower lying bands, but rapidly become significant as the band frequencies increase. To obtain accurate numerical solutions of the defect modes in the upper bands, a Green's function approach is recommended.[4-6] Green's functions take advantage of the fact that the defect modes are localized about the site of the physical defect, and require significantly less computer memory to achieve accurate results. Thus, defect modes in the high-frequency photonic band gaps of the 2D glide-symmetry structure can be studied. Two types of rod symmetries are present in the unit cell of this structure, and are expected to yield different defect characteristics depending on which is chosen as the site of the defect. In addition, removing multiple rods in this structure could yield modes with very unique properties due to the interplay of the different symmetry sites.

6.3 References

[1] P. R. Villeneuve, S. Fan, and J. D. Joannopoulos, "Microcavities in Photonic Crystals: Mode Symmetry, Tunability, and Coupling Efficiency," *Phys. Rev. B* **54**, 7837 (1996).

[2] B. D'Urso, O. Painter, J. O'Brien, T. Tombrello, A. Yariv, and A. Scherer, "Modal Reflectivity in Finite-Depth Two-Dimensional Photonic-Crystal Microcavities," *J. Opt. Soc. Am. B* **15**, 1155 (1998).

[3] P. L. Gourley, "Microstructured Semiconductor Lasers for High-Speed Information Processing," *Nature* **371**, 571 (1994).

[4] K. M. Leung, "Defect Modes in Photonic Band Structures: A Green's Function Approach Using Vector Wannier Functions," *J. Opt. Soc. Am. B* **10**, 303 (1993).

[5] A. R. McGurn, "Green's-Function Theory for Row and Periodic Defect Arrays in Photonic Band Structures," *Phys. Rev. B* **53**, 7059 (1996).

[6] M. G. Khazhinsky and A. R. McGurn, "Green's Function Method for Waveguide and Single Impurity Modes in 2D Photonic Crystals: H-polarization," *Phys. Lett. A* **237**, 175 (1998).